

Universidade de São Paulo
Instituto de Física

Estados ligados de Majorana no interior de vórtices em supercondutores

Bruna Shinohara de Mendonça



Orientador: Prof. Dr. Luis Gregório Dias

Tese de doutorado apresentada ao Instituto de Física da
Universidade de São Paulo, como requisito parcial para a
obtenção do título de Doutora em Ciências.

Banca Examinadora:
Prof. Dr. Luis Gregório Dias da Silva
Profa. Dra. Mariana Malard
Profa. Dra. Gabrielle Weber Martins
Prof. Dr. Gustavo Martini Dalpian
Profa. Dra. Barbara Lopes Amaral

São Paulo
2023

FICHA CATALOGRÁFICA
Preparada pelo Serviço de Biblioteca e Informação
do Instituto de Física da Universidade de São Paulo

Mendonça, Bruna Shinohara de

Estados ligados de Majorana no interior de vórtices em supercondutores. São Paulo, 2023.

Tese (Doutorado) - Universidade de São Paulo. Instituto de Física. Depto. de Física de Materiais e Mecânica.

Orientador: Prof. Dr. Luis Gregório Dias da Silva

Área de Concentração: Física

Unitermos: 1. Física computacional; 2. Sistema quântico; 3. Física da matéria condensada

USP/IF/SBI-025/2023

University of São Paulo
Physics Institute

Majorana bound states in superconductor vortex cores

Bruna Shinohara de Mendonça

Supervisor: Prof. Dr. Luis Gregório Dias

Thesis submitted to the Physics Institute of the University of
São Paulo in partial fulfillment of the requirements for the
degree of Doctor of Science.

Examining Committee:

Prof. Dr. Luis Gregório Dias da Silva

Prof. Dr. Mariana Malard

Prof. Dr. Gabrielle Weber Martins

Prof. Dr. Gustavo Martini Dalpian

Prof. Dr. Barbara Lopes Amaral

São Paulo
2023

Acknowledgements

I would like to immensely thank my parents, José and Fátima, for their great affection and support during my academic journey and for being the encouragers of my curiosity and feeling of self-confidence to feel able to follow the academic field from childhood to today.

I thank my advisor, Luis Gregorio Dias, for the proposal of this fascinating topic and for believing in me. Thanks to his trust, I have become a better and more ambitious researcher in those four years. I also thank my research group friends: Marcos, Raphael (a.k.a Levy), João, Lauro, and Lucas. Each of you is great and makes me constantly proud.

I also thank my advisor in the Center of Quantum Devices, Nancy Sandler, for receiving me and being interested in the subject. I am thankful for all the insights and great conversations. They changed my perspective in many beautiful ways.

I thank and wish CAPES, the sponsor of my Ph.D. fellowship in Brazil and my Joint Ph.D. fellowship in Denmark, longevity. This study was financed in part by the Coordenação de Aperfeiçoamento de Pessoal de Nível Superior - Brasil (CAPES) - Finance Code 001.

I thank Antonio, my main external collaborator, for the incredibly insightful discussions. I am also grateful for your patience in teaching me more about quantum transport and academic life in general.

I'm also grateful to my friends, inside and outside of physics, who have motivated me with tips, productive discussions about physics, or making me laugh. Your kindness and companionship inspire me.

A special thanks to two weirdly named groups of friends. First, the so-called "Less Able Students", were named after a section in a book on Relativity by Ray D'Inverno. The name is not suitable in any measure: you are the smartest, funniest, and most able people I know. Second, the G.A.V. (don't ask what the acronym means!) for long-lasting online and in-person friendships, besides great memes.

I thank Krissia, a friend and a doppelganger, for the heartfelt conversations throughout my Ph.D. They were incredibly helpful to have some to share difficult and delightful experiences.

A big thanks to Rodolfo for more than a great romantic relationship but also a great intellectual one. I am glad for the shared conversations about physics, philosophy, and whatever obscure topic one of us would decide to dive into that week. I appreciate every time I have spent with you, and I hope to be lucky enough to continue sharing experiences with you.

Finally, I thank all the people, throughout history, belonging to social minorities who took risks and contributed to the scientific field. Thank you for opening doors and allowing for a greater diversity of minds in the academic environment.

“It is a wonderful intellectual achievement, to have traced such profoundly consequential properties of matter to a basic aspect of identity — that is, indistinguishability — and the topology of motion in space-time.”

— Franck Wilczek, regarding anyonic particles.

*“I don’t need beads and wires
Don’t need no abacus
Don’t need no Pascaline
Don’t need no Babbage ’ngine
I got some news for Google
Don’t even need you too
(...)
Quantum computer, Ain’t no loser”*

— Wildebeast, “Quantum Computer”

Abstract

Research into the realization of Majorana quasiparticles has been driven by the relevance of quantum computing and topological materials. Initially, efforts were focused on nanowire realization of Majoranas, but experimental limitations and skepticism led to investigations into two-dimensional setups such as superconducting vortices [1]–[7]. In this study, we explore the potential and constraints of superconducting vortices as hosts of topological quasiparticles. We examine how scalar impurities can cause false-positive signatures of Majoranas in fully trivial superconductivity. Our findings show that scalar impurities can modify the Caroli-de Gennes-Matricon (CdGM) spectrum, resulting in spectral properties similar to Majorana Zero Modes (MZMs). Local scalar perturbations lower the energy of CdGM states and suppress their total Bardeen-Cooper-Schrieffer (BCS) charge, leading to impurity-driven zero energy states that cannot be distinguished from topological MZMs using local spectroscopic techniques. Additionally, extrinsic broadening of the particle-hole symmetric levels results in vanishing non-local transport signals, making it appear that the BCS charge is zero. These findings have implications for experimental works that rely on finite energy CdGM states [8]. We also investigate the potential of hybrid systems of semiconductors and trivial superconductors as substitutes for intrinsic topological superconductivity, which may provide a more robust way of retaining topological character [9], [10]. Whereas the p -wave order parameter's complex phase places limitations on the number of vortices that can be introduced, the scalar s -wave order parameter lacks this constraint. This discrepancy is significant because, despite having an equivalent total number of modes, the edge mode is not suitable for braiding. Furthermore, we remark that unequivocally topological zero energy mode in the topological region is not guaranteed for four vortices and is dependent on a suitably large scattering space, even in the approximation of minimal radii.

Keywords: Computational Physics, Quantum System, Condensed Matter Physics.

Resumo

A pesquisa sobre a realização de quasipartículas de Majorana foi impulsionada pela relevância da computação quântica e materiais topológicos. Inicialmente, os esforços foram focados na realização de nanofios de Majoranas, mas as limitações experimentais e o ceticismo levaram a investigações sobre configurações bidimensionais, como vórtices supercondutores [1]–[7]. Neste estudo, exploramos o potencial e as restrições dos vórtices supercondutores como hospedeiros de quasipartículas topológicas. Examinamos como impurezas escalares podem causar assinaturas falso-positivas de Majoranas em supercondutividade totalmente trivial. Nossos resultados mostram que as impurezas escalares podem modificar o espectro de Caroli-de Gennes-Matricon (CdGM), resultando em propriedades espectrais semelhantes aos Majoranas de energia zero. As perturbações escalares locais diminuem a energia dos estados CdGM e suprimem sua carga de Bardeen-Cooper-Schrieffer (BCS) total, levando a estados de energia zero movidos por impurezas que não podem ser distinguidos dos MZMs topológicos usando técnicas espectroscópicas locais. Além disso, o alargamento extrínseco dos níveis de simetria partícula-buraco resulta no desaparecimento de sinais de transporte não locais, fazendo parecer que a carga BCS é zero. Essas descobertas têm implicações para trabalhos experimentais que dependem de estados CdGM de energia finita [8]. Também investigamos o potencial de sistemas híbridos de semicondutores e supercondutores triviais como substitutos para a supercondutividade topológica intrínseca, o que pode fornecer uma maneira mais robusta de manter o caráter topológico [9], [10]. Enquanto a fase complexa do parâmetro de ordem p -wave coloca limitações no número de vórtices que podem ser introduzidos, o parâmetro de ordem escalar s -wave não possui essa restrição. Essa discrepância é significativa porque, apesar de ter um número total de modos equivalente, o modo de borda não é adequado para trançar. Além disso, observamos que o modo de energia zero inequivocamente topológico na região topológica não é garantido para quatro vórtices e depende de um espaço de espalhamento adequadamente grande, mesmo na aproximação de raio mínimo.

Keywords: Física Computacional, Sistema Quântico, Física da Matéria Condensada.

Contents

1	Introduction	17
2	Preliminary Theory	26
2.1	Superconductivity	26
2.1.1	Meissner effect and Londons' equation	26
2.1.2	Ginzburg-Landau formalism	27
2.1.3	Bardeen–Cooper–Schrieffer (BCS) formalism	30
2.1.4	Bogolioubov-de Gennes (BdG)	36
2.2	Algebraic-Topology Aspects in Physics	40
2.2.1	Topology and Exchange statistics in (2+1)D	41
2.2.2	Braiding	41
2.3	Symmetries in Condensed Matter	46
2.4	Physical Systems Hosting Anyons	49
2.5	Topological superconductivity: p -wave pairing	51
2.5.1	Majorana States	53
2.6	Majorana signatures	55
2.6.1	Quantized conductance	55
2.6.2	Zero bias peaks	56
2.6.3	Current periodicity in Josephson junctions	56
2.7	Experimental aspects	57
2.7.1	Braiding implementation protocols	57
2.7.2	Probing techniques	58
3	Ambiguity of MZM signatures in the presence of scalar impurities	60
3.1	Model	63
3.2	Effects of an impurity potential	65
3.3	Experimental relevance	68
3.4	Concluding Remarks	71
4	Multi-vortex configurations in semiconductor-superconductor hybrid systems	72
4.1	The hybrid setup	72
4.2	Zero-energy spinor components for many vortices	77
4.3	Topological Characterization for many vortices	80
4.3.1	Majorana Polarization	80
4.3.2	Multiple Vortices	81
4.4	Concluding remarks	86
5	Conclusions	87

A Braiding and Fusion formalisms	89
B Circuit Model of Quantum Computation	94
B.1 Example: Hadamard gate in the TQC hardware	97
C Majorana-like states in vortices	98
C.1 Poor man's majoranas	98
C.2 Quasi-majoranas	99
D Quasiparticle poisoning and error correction	100
D.1 Quantum Error Correction Protocols	100
E Perturbative corrections due to the impurity potential	102
F Finite Differences Method for the single vortex case	104
F.1 Generalization for many vortices	106
G Near zero-energy Caroli-de Gennes-Matricon vortex states in the presence of impurities	110

List of Abbreviations

- TQC: Topological Quantum Computing.
- MZM: Majorana Zero Mode.
- BCS: Bardeen-Cooper-Schrieffer.
- BdG: Bogoliubov-de Gennes.
- SC: Superconductor.
- CdGM: Caroli-de Gennes-Matricon.
- YSR: Yu-Shiba-Rusinov.
- ABS: Andreev Bound State.
- TI: Topological Insulator.
- 2DEG: two-dimensional electron gas.
- (L)DOS: (Local) density of states.
- FQHE: Fractional Quantum Hall Effect.
- STM: Scanning Tunneling Microscopy.
- STS: Scanning Tunneling Spectroscopy.
- ZBP: Zero-bias peak.

List of Symbols

- μ : Chemical potential.
- t : hopping constant.
- Δ : Superconducting order parameter.
- γ_i : Majorana fermion corresponding to the i site.
- c_i^\dagger / c_i : Dirac fermion creation and annihilation operators corresponding to the i site.
- α : Rashba strength.
- η : Screening length of a Gaussian impurity.
- $\delta\mu$: Impurity strength.
- ξ : Vortex radius.
- γ : level broadening parameter.

List of Figures

1.1	a) Schematic representation of four vortices on a topological superconductor representing a two-level system based on their parities, on a spacetime diagram. b) When the Majorana quasiparticle in vortex γ_2 goes around vortex γ_3 , the crossing of the branch cut can be mapped to a σ_x operation. c) A complete exchange of positions between γ_2 and γ_3 generates a $\sqrt{\sigma_x}$ operation. Adapted from [29].	18
1.2	a) Top: device layout, containing a nanowire, parallel magnetic field, B and perpendicular spin-orbit component, B_{SO} , above a s -wave superconductor. Red stars represent the Majorana quasiparticles, predicted to be at the ends of nanowires. Bottom: dispersion relation, showing how the addition of terms in the Hamiltonian allows for gap opening. b) Scanning microscopy of the physical device, indicating normal (N) and superconducting (S) leads, and the dielectric covered gates, labeled 1 through 4. Adapted from [33].	20
1.3	a) I-V characteristic as function of the voltage V, for different values of magnetic field, B, starting from B = 0 mT (bottom curve) to B = 490 mT (top curve). b) Voltage as function of magnetic field and I-V characteristic. Adapted from [33].	20
1.4	The right: fig. 2 from the retracted paper, left side: fig. 3 from the republished paper. Top row shows voltage bias, V, as function of the I-V characteristic and tunnel-gate voltage, V_{TG} . Middle row present I-V characteristic as function of the tunnel-gate voltage for V = 0 mV. Bottom row: sames as middle row, but for Middle row present I-V characteristic as function of the tunnel-gate voltage for $V_{TG} = \pm 0.2$ mV. Adapted from [36] and [37].	21
1.5	Non-topological mechanisms for zero-bias peaks in nanowires. In the first row, simulations containing a quantum dot, with a) showing conductance measure on the left lead and b) showing conductance from the right lead. The bottom row of figures shows the effect of inhomogeneties measured in left (c) and right (d) leads. Adapted from [3].	22
1.6	Superconducting vortex analyzed via STM/S method. A) Zero-Bias peak spatial map. B) Intensity plot along the black dashed line in (A). (C) A waterfall plot of (B) with 65 spectra. Adapted from [7].	23
2.1	Scattering of time-reversed pairs of electrons, in diagrammatic form.	33
2.2	Dyson equation for the pair scattering vertex in diagrammatic form.	33
2.3	Trivial (above) and topological (below) regimes in a Kitaev chain. The circles represent Majorana particles in a chain. The dashed ovals represent the Fermions encompassing two Majorana particles each. The pink oval represents the non-zero hopping terms. In the topological regime, the end Majorana particles are not connected to the Hamiltonian, having zero energy.	52

2.4	The two possible types of trajectories in the unit sphere as k go from 0 to π and their corresponding topological invariant.	53
2.5	Pictoric scheme for a Scanning Tunneling Microscope. Scanning surface with different heights provide different tunneling current values.	59
3.1	Energy states inside the vortex for (a) a clean s -wave superconductor and (b) an s -wave system with screened charge impurity. The blue line shows the position-dependent superconducting order parameter, and the dashed lines schematically show the energy of in-gap CdGM states. In panel (b), the black dashed lines indicate the CdGM spectrum without a charged impurity, whereas the red dashed lines indicate the spectrum with the impurity. The black arrow highlights the energy shift caused by the impurity potential. Panels (c) and (d) show the density of states, whereas (e) and (f) show the BCS spectral charge for the s -wave system without and with impurity respectively.	62
3.2	Magnitude (a) and phase (b) of the superconducting order parameter (as defined in Eq. (3.3)). The BCS charge-resolved spectrum of in-gap vortex states is shown for s -wave superconductor (c) without and (d) with an screened charge impurity with $\delta\mu = 0.06t$ and $\eta = 5a$	64
3.3	BCS charge for an s -wave system with impurity. In panels (a,b), the spectrum evolves as a function of (a) impurity size η ($\delta\mu = 0.025t$), (b) impurity strength $\delta\mu$ ($\eta = 5a$). (c) BCS charge (black) and BCS charge spectral density (red) for the lowest energy state for a system without (dashed line) and with (solid line) an impurity with $\eta = 5a$ and $\delta\mu = 0.05t$	66
3.4	Dependence of lowest energy state $E_{1/2}$ (a, c) and BCS charge (b, d) on (a, b) η and ξ , (c, d) η and $\delta\mu$. In (a, b) we choose $\delta\mu = 0.06t$, and in (c, d) we choose $\xi = 5a$	67
3.5	Density of states $A(\omega) \equiv (-1/\pi)\text{Im} G(\omega)$ of an s -wave superconductor as a function of level broadening γ ($\eta = 5a$). In panel (a), one can observe that the two trivial states are distinguishable in the absence of an impurity ($\delta\mu = 0$) up to $\gamma \sim E_{1/2}$. As the impurity strength increases, as shown in panels (b-d), the trivial states are shifted to smaller energies ω and therefore one cannot distinguish them even with a much smaller level broadening γ	69
4.1	Physical setup for the hybrid device studied.	74
4.2	Spinor components from the reduced BdG Hamiltonian with a vortex-like order parameter. where we used $\eta = \alpha = V_z = -\lambda = 1$, $\Delta_0 = 0.1$ and $\mu = 0$	76
4.3	A visual scheme for two vortices in real space. The distance between vortices is assumed to be greater than the vortex core, $R_{core} = 1$	77
4.4	Spinor component solutions. Using parameters to account for one vortex.	79
4.5	Single vortex case: Spectrum. Here, $\Delta = 0.5$	81
4.6	Two vortices case: a) spatial distribution of the density of states, b) spatial distribution of the Majorana Polarization.	82
4.7	Two vortices case positioned at $r_1 = (30,0)$ and $r_2 = (-30,0)$: Spectrum as a function of V_z	82
4.8	Two vortices case, with $(-1,1)$ phases, positioned at $r_1 = (10,0)$ and $r_2 = (-10,0)$: a) spatial distribution of the density of states, b) spatial distribution of the Majorana Polarization.	83

4.9	Four vortices. a) spatial distribution of the density of states for for (+1,-1,+1,-1) phases. b) spatial distribution of the density of states for for (-1,+1,+1,-1) phases. c) spatial distribution of the Majorana Polarization for (+1,-1,+1,-1) phases. d) spatial distribution of the Majorana Polarization for (-1,+1,+1,-1) phases. . . .	84
4.10	Four vortices case positioned at $r_1 = (20,0)$, $r_2 = (-20,0)$, $r_3 = (0, 20)$ and $r_4 = (0,-20)$. a) spectrum as a function of V_z for (+1,-1,+1,-1) phases. b) spectrum as a function of V_z for (-1,+1,+1,-1) phases.	85
4.11	Four vortices case positioned at $r_1 = (20,0)$, $r_2 = (-20,0)$, $r_3 = (0, 20)$ and $r_4 = (0,-20)$: spectrum as a function of V_z on a 200x200 sites scattering setup.	85
A.1	Pictorial demonstration of first braiding relation. Braiding diagrams can be composed by concatenation of the end of an operation with the beginning of another for each particle, as shown by the purple arrows. The dashed lines represent that the trajectory is below the full line.	90
A.2	Pictorial demonstration of second braiding relation. Braiding diagrams can be composed by concatenation of the end of an operation with the beginning of another for each particle, as shown by the purple arrows. The dashed lines represent that the trajectory is below the full line. Smaller, lesser-spaced dashed lines are below both the larger dashed line and the full line.	90
A.3	Pictorial demonstration of $B = F^{-1}RF$	92
B.1	Bloch sphere visualization. a - A qubit in the bloch sphere, initialized in $ 0\rangle$ state. b - Action of σ_x on the initial qubit, performing a bit-flip and bringing the qubit to state $ 1\rangle$. c - Action of σ_z on the bit-flipped qubit, now performing a phase-flip, indicated by the red color of the state.	95
B.2	Action of the Hadamard gate on the initial qubit, $ 0\rangle$, creating an equal superposition of $ 0\rangle$ and $ 1\rangle$	95
B.3	Action of the CNOT gate on the initial qubit, $\frac{1}{\sqrt{2}}(0\rangle + 1\rangle) 0\rangle$, on the Q-Sphere, a generalization of the Bloch sphere for multi-qubits. creating the entangled state $\frac{1}{\sqrt{2}}(00\rangle + 11\rangle)$	96
F.1	Comparison between <code>bvp_solve</code> and finite differences methods.	106

List of Tables

2.1	Relevant Feynman diagrams correspondence.	33
2.2	Classes of topological systems based on chiral, particle-hole and time-reversal symmetries. Missing entries represent the absence of the corresponding symmetry. The other entries represent the value of the corresponding symmetry operator squared.	47
2.3	Classes of topological systems based on symmetries and topological invariants in dimensions $d = 0, 1, 2, 3$	48

Chapter 1

Introduction

In 2016, the Nobel prize in Physics was awarded to D. Thouless, F. Haldane and J. Kosterlitz for their studies on the unlikely marriage of an abstract branch of mathematics, Algebraic Topology, and a tangible branch of Physics, of materials [11]–[14]. While Differential Topology was already an acquaintance of researchers in General Relativity, with the concept of manifolds, Algebraic Topology seemed to be out-of-place in Physics for a long time. The field started to show its relevance with the establishment of Topological Quantum Field Theory [15], [16]. Currently, popular research topics in condensed matter make use of topological toolbox, such as graphene physics, spin liquids and quantum error correction [17]–[19].

Truly remarkable physical phenomena are better understood with the aid of Algebraic Topology concepts. Topological defects, such as vortices in superconductors, allows for statistics beyond Fermionic and Bosonic in two-dimensions. The Berry phase, related to topological properties of the parameter space, can be a measurable quantity and have consequences to electronic properties of materials and optics [20]–[22]. Furthermore, topological invariants can be associated to physical systems, allowing for systematic classifications of materials and better understanding of the conditions for phase transitions that cannot be described purely via symmetry breaking [23].

Majorana states are a prominent instance of topological phenomena in materials [24], [25]. In general terms, these quasiparticles arise as solutions of the Dirac equation when the particle is its own antiparticle [26]. Symmetry and topological properties allow for Majorana's special set of features, including robustness to local perturbations and neutral charge [23], [24].

Majorana states and Quantum Computing - Resistance to perturbations is a strongly sought-after property in Quantum Computing, where decoherence due to noise is a prevalent problem [27], [28]. The robustness of topological states could, therefore, benefit quantum computing hardware. Indeed, it can be shown that four Majorana states are mappable to a two-level system (qubit) based on their fermionic parities.

Even more conveniently, not only bound Majorana quasiparticles are robust, they are **non-abelian anyons**. In practice, this means that the crossing of worldlines, called braiding, of these types of particles does not renders a scalar phase, but a unitary matrix [23]. In gate-based quantum computation, unitary matrices are applied to qubits to perform computational tasks. Braiding allows for many of the relevant matrices for quantum computing, as exemplified in Fig. 1.1¹ [29].

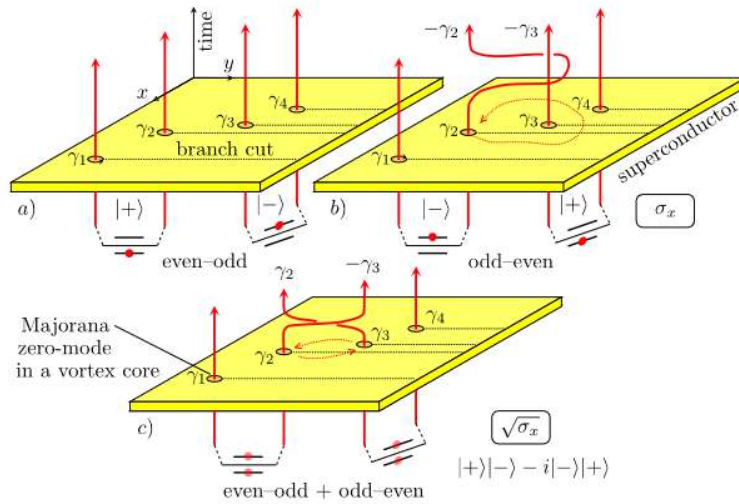


Figure 1.1: a) Schematic representation of four vortices on a topological superconductor representing a two-level system based on their parities, on a spacetime diagram. b) When the Majorana quasiparticle in vortex γ_2 goes around vortex γ_3 , the crossing of the branch cut can be mapped to a σ_x operation. c) A complete exchange of positions between γ_2 and γ_3 generates a $\sqrt{\sigma_x}$ operation. Adapted from [29].

Unsurprisingly, research on the realization of Majorana quasiparticles was propelled by the topical relevance of both Quantum Computing and topological materials fields.

Proposed realizations of Majorana quasiparticles

Majorana states are predicted to exist in two-dimensional electron fluids with external magnetic field in the Fractional Quantum Hall (FQH) regime and in a topological superconductor

¹Not all matrices can be constructed via braiding - this is discussed in Appendix B.

with vortices.

In this work, we focus on the superconductor realization. In such systems, non-abelian anyons are predicted to appear in the ends of a nanowire or in vortices in two-dimensional setups. Until recently, experimental efforts revolved around the nanowire realization of Majoranas, where the superconducting pairing potential is linearly dependent of the momentum. This type of pairing is referred to as ***p*-wave** and is one of the possible superconducting pairings that provides topological superconductivity [1].

Highlights from recent research in Majorana physics

The *p*-wave superconductivity is not only uncommon as a pairing configuration, but it is also a controversial topic, as the leading candidate material with this pairing, Strontium Ruthenate (Sr_2RuO_4), is not unanimously considered as truly topological by the Superconducting Physics community [2], [30]–[32].

In contrast, it is possible to make use of a more common superconductivity pairing, ***s*-wave**, that independes of momentum. Allied with semiconductors with spin-orbit and a magnetic insulator, *s*-wave superconductivity can be used to create effective topological superconductivity [10]. In this work, we refer to this realization as hybrid semi-superconductor setups. In the following subsections, we discuss two key papers in hybrid nanowires setups.

Mourik, Vincent et al. (2012) experiment

This work focus on electrical measurements of the nanowire realization of a semiconductor with strong spin orbit, Indium Antimonide, in contact with a normal and a superconducting electrode [33].

Fig 1.2 A shows a pictorial representation of the setup: a semiconducting nanowire, placed on the top of an *s*-wave (trivial) superconductor, with a magnetic field parallel to the lenght of the nanowire and spin-orbit component perpendicular to it. At the botton, fig. 1.2 A illustrates how the addition of a Rashba term, coming from spin-orbit interaction, allows for the separation of spin up (red) and spin down (blue) components. Furthermore, the curves in black represents the effect of introducing a parallel magnetic field - it opens a gap.

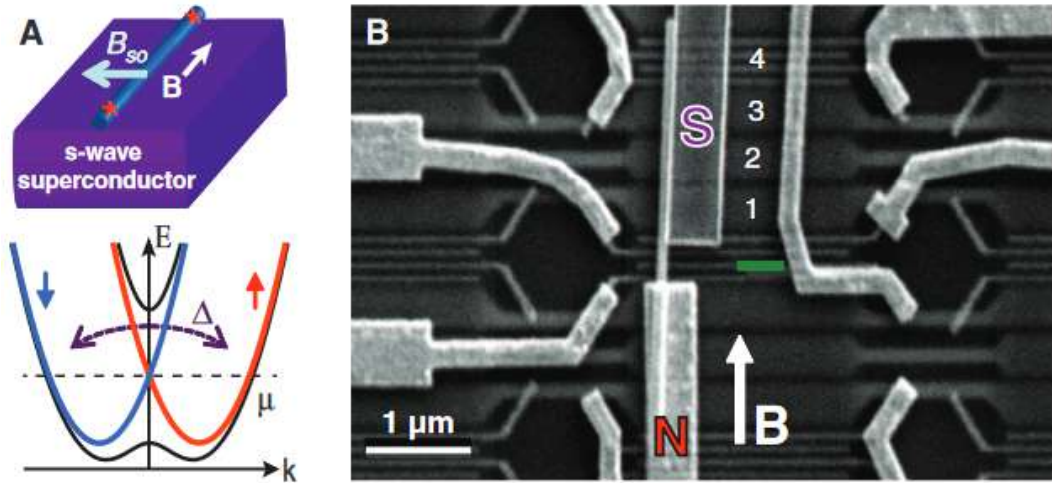


Figure 1.2: a) Top: device layout, containing a nanowire, parallel magnetic field, B and perpendicular spin-orbit component, B_{SO} , above a s -wave superconductor. Red stars represent the Majorana quasiparticles, predicted to be at the ends of nanowires. Bottom: dispersion relation, showing how the addition of terms in the Hamiltonian allows for gap opening. b) Scanning microscopy of the physical device, indicating normal (N) and superconducting (S) leads, and the dielectric covered gates, labeled 1 through 4. Adapted from [33].

Figs. 1.3 represent the main results. In fig. 1.3 a, zero bias peaks can be observed for a wide range of magnetic field strengths, in accordance to the expected robustness of Majorana quasiparticles. Here, the green arrows represent peaks arising from the gap edges. The presence of zero-bias peak (ZBP) is an important signature of the presence of Majoranas. In low temperatures, when the bias V is zero, a prominent peak in conductance is predicted to appear².

Fig. 1.3 b showcases the dependency between voltage and magnetic field. Both the zero-bias peak and the edge peaks can be observed for a range of magnetic fields.

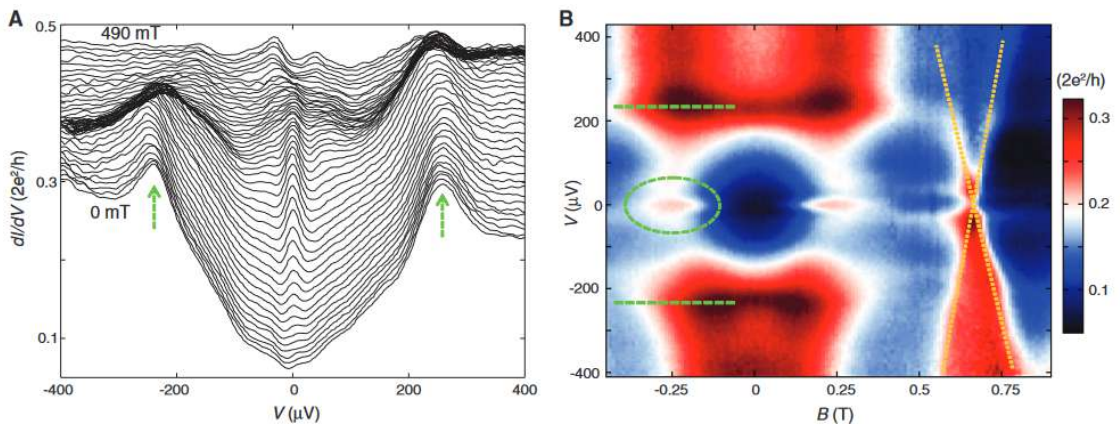


Figure 1.3: a) I-V characteristic as function of the voltage V , for different values of magnetic field, B , starting from $B = 0$ mT (bottom curve) to $B = 490$ mT (top curve). b) Voltage as function of magnetic field and I-V characteristic. Adapted from [33].

²Refer to section 2.6 for more details on experimental Majorana signatures.

The paper also seeks to rule out other possible mechanisms for the formation of ZPBs, such as Kondo effect and trivial Andreev Bound States [34]. However, since 2012, many efforts on establishing smoking-gun signatures for Majoranas had clarified that resistance of ZPBs to high magnetic fields are far from enough to claim Majorana presence [2], [35].

Retraction of Zhang, Hao et al. (2018) paper

Moving along in the timeline, we have another important paper, with seemingly more convincing data to claim the existence of Majorana quasiparticles in condensed matter [36].

This paper, originally titled "Quantized Majorana Conductance", studies Indium Antimonide again, now covered with Aluminum to create a superconducting shell. The work showcased I-V characteristic plots with apparent and accordance to the simulated data, presenting zero-bias peaks. It also displayed conductance in the expected quantized value of $G = 2e^2/h$, where e is the electron charge and h is Planck's constant. However, independent reexamination of the raw data revealed that the plotted data was partially cut out. In 2021, a retraction note was issued. The corrected data is now republished with the more modest title of "Large zero-bias peaks in InSb-Al hybrid semiconductor-superconductor nanowire device" [37].

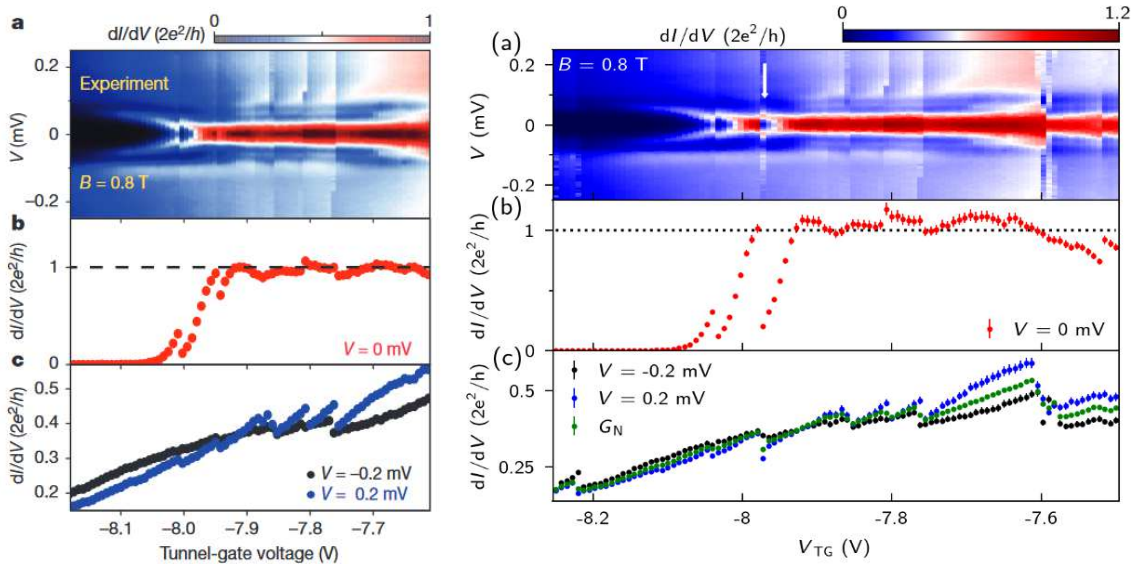


Figure 1.4: The right: fig. 2 from the retracted paper, left side: fig. 3 from the republished paper. Top row shows voltage bias, V , as function of the I-V characteristic and tunnel-gate voltage, V_{TG} . Middle row present I-V characteristic as function of the tunnel-gate voltage for $V = 0$ mV. Bottom row: same as middle row, but for Middle row present I-V characteristic as function of the tunnel-gate voltage for $V_{TG} = \pm 0.2$ mV. Adapted from [36] and [37].

A side-by-side comparison of both works is instructive to understand the main issues of the

original paper. The right side of fig. 1.4 shows fig. 2 from the retracted paper, while the left side presents fig. 3 from the republished paper [37]. It is noticeable, from the top row figures, that information was omitted. The sudden valley in conductance around $V_{TG} = -7.95V$ is a possible sign of charge jump originated from charge disorder. It is important to highlight that disorder in nanowires is one of the possible causes for the appearance of zero-bias peaks, as seen in 1.5 [3].

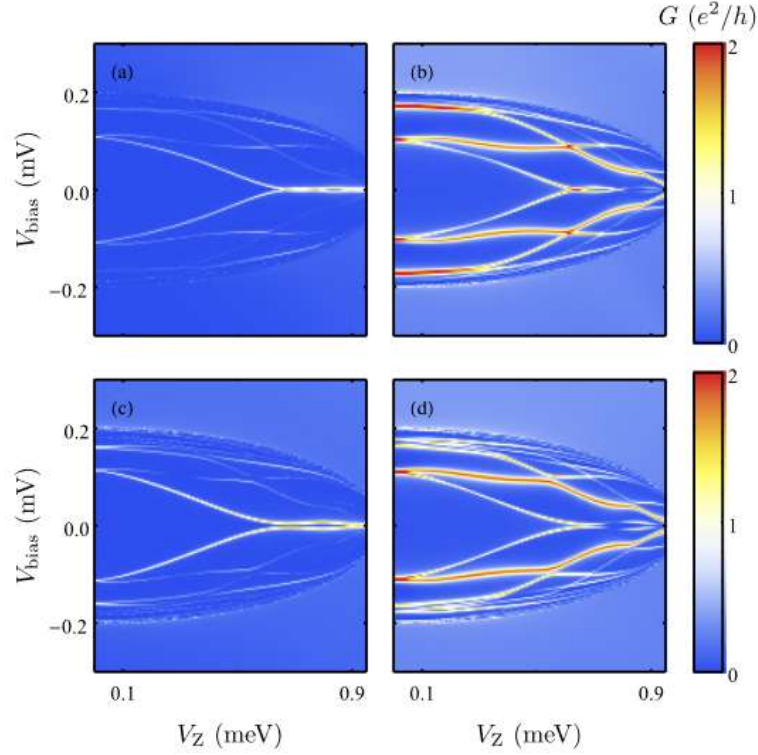


Figure 1.5: Non-topological mechanisms for zero-bias peaks in nanowires. In the first row, simulations containing a quantum dot, with a) showing conductance measure on the left lead and b) showing conductance from the right lead. The bottom row of figures shows the effect of inhomogeneities measured in left (c) and right (d) leads. Adapted from [3].

Another discrepancy can be observed between the middle row plots. In the republished paper, it is evident, even considering error margins, that the conductance is higher than the expected conductance value for many tunnel-gate voltage values. The claim that originally gave the paper's title was no longer valid.

Lessons learned and applied in this thesis

Such developments in experiments make evident that there are reasons to be careful when interpreting Majorana signatures. In the present work, we explore alternatives to previous methods to probe Majorana quasiparticles, motivated by caution, in two different approaches:

1. Moving from nanowires to vortices

Nanowires possess practical limitations, such as the need to fine-tune experimental parameters to control the topological regime and difficulties in implementing quantum gates for quantum computing-based applications [29], [38], [39]. These practical aspects were motivations for the shift to two-dimensional setups, where Majorana states may appear bound to the interior of vortices in superconductors [10], [27], [29], [40].

A second motivation to study vortex-bounded Majoranas is the current skepticism in some approaches to their detection in nanowires. At the present moment, experimentalists rely on surface methods, such as Scanning Tunneling Microscopy (STM) and Spectroscopy (STS) to detect the predicted energy and charge signatures for Majorana states. As discussed, theory predictions are translated in practice by seeking zero-bias conductance peaks, quantized conductance plateaus, and Josephson Junction 4π -periodic current as evidences of topological superconductivity [2], [25]. More recently, non-local surface methods were proposed to evaluate charge neutrality in such systems [41]. Figure 1.6 is an example of STM/S usage for vortex analysis.

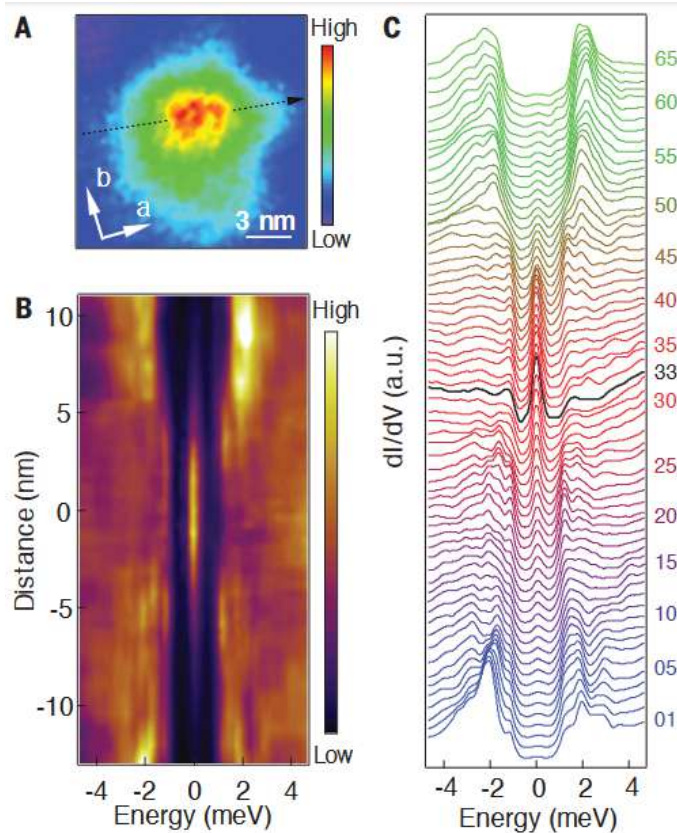


Figure 1.6: Superconducting vortex analyzed via STM/S method. A) Zero-Bias peak spatial map. B) Intensity plot along the black dashed line in (A). (C) A waterfall plot of (B) with 65 spectra. Adapted from [7].

However, as previously discussed and illustrated by the results in figure 1.5, such signatures may arise from different mechanisms in condensed matter [2]–[7]. While theoretical studies have been carried out in nanowires, two-dimensional setups for Majoranas are a less explored road that can shed new light on previous difficulties.

In particular, we are interested in explore the limitations of the currently established signatures of Majoranas in the presence of scalar impurities in superconducting vortices. We show, through numerical calculations, that both energy and charges of trivial states in vortices can mimic non-trivial Majoranas signatures (zero energy and charge). Furthermore, we demonstrate that improving apparatus resolution may not be enough to differentiate Majorana states from non-topological states due to level broadening. These studies are compiled in our 2022 paper with collaborators [8].

2. Moving from p -wave pairing to extrinsic topological superconductivity in two dimensions

With the same intent of exploring lesser-known paths in Majorana physics, we also analyze the use of extrinsic topological superconductivity i.e. superconductivity whose topological properties are engineered in the Hamiltonian, rather than naturally arising from p -wave superconducting pairing in two dimensions.

We focus on understanding the particularities of adding more than on vortex when trivial superconductivity is aided with other Hamiltonian terms to create effective topological system. In p -wave systems the boundary conditions imposes constraints in the number of available Majorana modes. In practice, this means that both geometry, in the sense of number of domain walls of the system, and number of injected vortices are factors the determine the number of Majorana states present in the material.

These difficulties are lifted in s -wave pairing. With this subtlety in mind, we numerically analyze spectral differences of both setups in terms of topological characterization by making use of a generalized signature of Majorana character, Majorana Polarization.

Outline of the thesis

As a whole, this work explore the possibilities and limitations of the vortices in superconductors as hosts of topological quasiparticles, from a practical standpoint. We approach this investigation in different ways: first, analyzing impurities in two-dimensional setup and second, testing the quality of Majorana signatures in a extrinsic topological setup. This leads to the thesis structure.

- In chapter 2 , we delve into the preliminary theory required to understand the scope of this work: physics of superconductors, relationship with symmetries, topological aspects, braiding and experimental techniques.
- In chapter 3, we investigate how fully trivial superconductivity can present false-positive signatures of Majoranas in the presence of scalar impurities, for both energy and charge measurements [8]. We explore how apparatus resolution is not necessarily the straightforward solution to the signature ambiguity, as the expected level broadening is also detrimental to unequivocally differentiate Majorana states from the topological trivial states that may coexist in vortices.
- In chapter 4, we follow the path of examining proximitized superconductivity in two dimensions, making use of trivial s -wave and additional external parameters to mimic intrinsic topological superconductivity in vortices [9], [10]. We examine the advantages and disadvantages of this approach via computational simulation.
- Chapter 5 summarizes conclusions from the previous chapters, discusses limitations on the making of this thesis and possible implications of the present study on Majorana physics in vortices.

Chapter 2

Preliminary Theory

2.1 Superconductivity

Although following the historical sequence of events may not always be the best approach to studying many topics in physics, it will be useful here, as the frameworks follow a monotonical progression from macroscopic to microscopic concepts, with each approach leading to insights that would allow the development of the next one. The main theories on superconductivity (SC) that we will briefly cover are, in chronological order: Londons', Ginzburg-Landau, Bardeen-Cooper-Schrieffer (BCS) and Bogoliubov-de Gennes (BdG).

Topological superconductivity, in particular, requires the brief introduction of concepts in Algebraic Topology from section 2.2; thus, it will be covered later in the thesis.

2.1.1 Meissner effect and Londons' equation

Superconductivity was first observed in 1911, in the form of a complete suppression of resistivity in Mercury when cooled below a critical temperature [42]. Further studies on superconducting material led to, twenty years later, the observation of weak magnetic fields being expelled - the Meissner effect [43].

The thermodynamic behaviour of the material in relation to an external field leads to one of several classifications of superconductors. Type I superconductors are materials in which the magnetization decays instantly above a critical field, H_c . Type II superconductors are characterized by the magnetization decay from a first critical field H_{c1} to a second, higher one, H_{c2} . In practice, in type II superconductors there is penetration of flux between the two critical fields, but not enough to break superconductivity.

In 1935, the London brothers investigate the phenomenon from the electrodynamics standpoint [44]. Modeling the supercurrent \vec{J} as carried by a fraction n_s of electrons with velocity \vec{v} ,

$$\vec{J} = -en_s\vec{v}. \quad (2.1)$$

We may take the time derivative of the supercurrent to relate the electric field, \vec{E} .

$$\frac{\partial}{\partial t}\vec{J} = \frac{n_s e^2}{m_e c}\vec{E}. \quad (2.2)$$

Then, taking the rotational of eq. (2.2) and considering Maxwell's equation:

$$\frac{\partial}{\partial t}\left(\nabla \times \vec{J} + \frac{n_s e^2}{m_e c}\vec{B}\right) = 0, \quad (2.3)$$

where m_e is the mass of the electron and c is the speed of light. As the Meissner effect implied the possibility of flux changes over time, the London brothers proposed a more restricted version of eq. (2.3) to model superconductivity, now known as London's equation:

$$\nabla \times \vec{J} + \frac{n_s e^2}{m_e c}\vec{B} = 0. \quad (2.4)$$

London's equation, when combined with Ampere's law, yields

$$\nabla \times \nabla \times \vec{B} = -\lambda \vec{B}, \quad \lambda \equiv \left(\frac{4\pi n_s e^2}{m_e c^2}\right)^{-1/2}. \quad (2.5)$$

The parameter λ is called **London penetration depth**, a quantifier for how further into the material could the field penetrate. This can be seen by solving eq. (2.5) for, as an example, an external field $\vec{B} = B_0 \hat{z}$ in a radius x . We have λ appearing as a spatial scale:

$$\vec{B} = -B_0 e^{-x/\lambda} \hat{z}. \quad (2.6)$$

2.1.2 Ginzburg-Landau formalism

The Ginzburg-Landau theory is a phenomenological approach to superconductivity that revolves around the concept of **order parameter**, that is, a parameter that characterizes different thermodynamic or quantum phases of matter. The idea is to define a partition function depending

on the order parameter, ϕ , as

$$Z = \int_{-\infty}^{\infty} d\phi e^{-\beta N f(\phi, T, h)}. \quad (2.7)$$

Here, T is the temperature, $\beta = T^{-1}$ and h is the magnetization. As the integral is dominated by the minimal value of the exponential argument, we may use

$$\left. \frac{\partial F(\phi, T, h)}{\partial \phi} \right|_{\phi=m} = 0. \quad (2.8)$$

Thus, we obtain the order parameter with an appropriate ansatz for $F(\phi)$ [45]. The Free energy density functional, in its simplest form, can be expanded in powers of the order parameter:

$$F(T) = F_0(T) + a(T)|\phi|^2 + \frac{1}{2}b(T)|\phi|^4 + \dots \quad (2.9)$$

with $b(T) > 0$ due to the stability of the solution. From here, it is possible to find the condensation energy and check that there is a symmetry breaking that dictates the phase transition between $F(T)$ and $F_0(T)$ phases when $a(T)$ is negative [46]. In this case,

$$|\phi|^2 = -\frac{a(T)}{b(T)} \quad (2.10)$$

While developing the theory, Ginzburg and Landau interpreted the order parameter assumed a complex phase form - a vortex-like solution:

$$\psi \propto f(r)e^{i\theta}, \quad (2.11)$$

where $f(r)$ encompasses the radial dependency of the solution, to be deduced later, and θ accounts of the angular dependency. Here and onwards, we denote the order parameter solution as ψ instead of ϕ . In the original paper, there was no explicit interpretation for ψ : its understanding as a center-of-mass wavefunction corresponding to the Cooper pair would be developed later.

For the vector potential, \vec{A} , we have:

$$A(r) = \frac{1}{r} \int_0^r r' h(r') dr' \quad (2.12)$$

Evaluated in the center of the vortex, we have:

$$A(r) = \frac{h(0)}{2} r \quad (2.13)$$

Away from the center, we encompass the total flux $\Phi_0 = \oint A \cdot ds$, and

$$A_\infty = \frac{\Phi_0}{2\pi r} \quad (2.14)$$

In the presence of an electromagnetic (EM) field, we have extra terms in the functional:

$$F = F_0 + a|\psi|^2 + \frac{b}{2}|\psi|^4 + \frac{1}{2m^*} [(-i\nabla + 2eA)\psi(r)]^2 + \frac{B^2}{8\pi}. \quad (2.15)$$

The fourth term on the right-hand side is a gauge-invariant form of the kinetic part of the free energy. We may find the solution for $f(r)$ by minimizing the functional (recall that $|\psi|^2 = -a(T)/b(T)$ in the phase transition):

$$\delta F = 0 = a\psi + b|\psi|^2\psi - \frac{1}{2m^*} [(-i\nabla + eA)\psi]^2, \quad (2.16)$$

where $m^* = 2m_e$ and m_e is the electron mass. In terms of $f(r)$, in the center of the vortex, substitution in eq. (2.16) leads to:

$$f - f^3 - \xi^2 \left[\left(\frac{1}{r} - \frac{\pi h(0)r}{\Phi_0} \right)^2 f - \frac{1}{r} \frac{d}{dr} \left(r \frac{df}{dr} \right) \right] = 0, \quad (2.17)$$

where we introduced the characteristic length, $\xi(T)$:

$$\xi(T) = \left(\frac{1}{2m^*|a(T)|} \right)^{1/2} \quad (2.18)$$

We can look for polynomial solutions of the form $f(r) \approx cr^n$. Substituting back to eq. (2.17),

$$cr^n - (cr^n)^3 - \xi^2 \left[\left(\frac{1}{r} - \frac{\pi h(0)r}{\Phi_0} \right)^2 cr^n - n^2 cr^{n-2} \right] = 0. \quad (2.19)$$

We want to avoid the divergence coming from the last term. Furthermore, respecting the boundary conditions of f being constant away from the vortex center and $f \rightarrow 0$ approaching the vortex center, an appropriate solution is [47]:

$$f = \tanh\left(\frac{\alpha r}{\xi}\right). \quad (2.20)$$

with α being a constant.

It is important to highlight how successful the theory is: it predicts both types I and II of superconductivity by considering different regimes, besides recovering the London equation using the functional formalism [45].

In superconductors, it is worth mentioning two topologically trivial excitations with energies below the superconducting gap that may appear in the vortex core: Yu-Shiba-Rusinov and Caroli-de Gennes-Matricon states.

In the next section, we will properly introduce a third type of state trapped in vortices cores, but of topological nature: Majorana states. All three types belong to a class of subgap states named **Andreev Bound States (ABSs)**. In a clean system, the topologically trivial and non-trivial ABSs may have deceptive similarities - this is the central theme for chapter 3.

Yu-Shiba-Rusinov (YSR) - In independent works, L. Yu, H. Shiba and A. I. Rusinov expanded on the work of A. Abrikosov and L. Gor'kov on superconductors in the presence of paramagnetic impurities [48]. They demonstrated the appearance of in-gap states in superconductor vortices in the presence of magnetic impurities. By considering a *classical spin*¹, in a similar fashion as the Kondo effect, it is possible to show that low-energy states appear in type-II vortices.

Caroli-de Gennes Matricon (CdGM) - these states appear as low-lying excitations inside of type-II superconductors [50]. In pristine conditions, the spectrum is:

$$E_m = \frac{m\Delta_0}{k_F\xi}, \quad (2.21)$$

where $m = (n + 1/2)$, $n \in \mathbb{Z}^*$, k_F is the Fermi momentum, ξ the bulk coherence length, and Δ_0 is the bulk superconducting pairing potential. Therefore, CdGM states have energies above zero. Symmetric zero-bias peaks around zero-energy in STM experiments are a signature of these states [51]. Majorana states, in contrast, have zero-bias peaks precisely at zero energy.

2.1.3 Bardeen–Cooper–Schrieffer (BCS) formalism

Thanks to realizing the need for an order parameter in the Ginzburg-Landau formalism, J. Bardeen, L. Cooper and J. Schrieffer took the first step to a microscopic theory of superconductivity. Before discussing their mean-field theoretical approach, we develop the effective

¹Here, "classical spin" means to consider the product $\mathbf{S}\cdot\mathbf{J}$ finite, here \mathbf{S} is the spin component and \mathbf{J} is the coupling constant in the interaction term between conducting electrons and the localized spin [49]

Hamiltonian for superconductivity, coming from the realization that the resulting potential from electron-phonon interactions is attractive. We also note the importance of scattering processes for superconductivity, resulting in the condensation of fermions in the ground state.

From a phenomenological standpoint, the attractive potential comes from distortions of the phonon lattice, modeling the ionic background in superconductors. While free electrons flow with a characteristic Fermi velocity ϵ_F , lattice distortions relate to the Debye frequency, ω_D . In superconductors, the differences between timescales difficult the flow of electrons in a phonon background, resulting in attracted electrons due to the effective electron-phonon interaction [52]. To better understand the phenomenon, we start by considering the free phonon Hamiltonian,

$$H_{ph} = \sum_{q\lambda} \Omega_{q\lambda} \left(b_{q\lambda}^\dagger b_{q\lambda} + \frac{1}{2} \right), \quad (2.22)$$

where $b_{q\lambda}^\dagger, b_{q\lambda}$ are phonon operators and $\Omega_{q\lambda}$ is the plasma frequency. The index q refers to momenta and λ refers to different branches, accounting for the fact that a unit cell will contain two ions in this model. The electron-phonon interaction in the lattice model is:

$$V_{e-p} = \frac{1}{\mathcal{V}} \sum_{k\sigma} \sum_q g_q c_{k+q,\sigma}^\dagger c_{k\sigma} (b_{q\lambda} + b_{-q\lambda}^\dagger) \quad (2.23)$$

where $c_{q,\sigma}, c_{q,\sigma}^\dagger$ are the electron operators, a g_q is the electron-phonon coupling strength and \mathcal{V} is the volume constraining the modes.

To define the electron-phonon coupling, we will consider a neutral ionic background; this is modeled by the **Jellium** model. In this model, we may relate g_q with a plasma frequency for the whole ionic background, Ω . Considering N as the number of ionic modes, Ze as the ions charge and M as their masses,

$$g_q = \frac{iZe^2}{\epsilon_0 q} \sqrt{\frac{N}{2M\Omega}} \quad (2.24)$$

We may define a new operator to encompass the phonon contribution for the interaction term.

$$A_{q\lambda} \equiv b_{q\lambda} + b_{-q\lambda}^\dagger. \quad (2.25)$$

In the interaction picture, the evolution parametrized by the imaginary time τ is given by $A_{q\lambda}(\tau) = e^{\tau H_{ph}} A_{q\lambda} e^{-\tau H_{ph}}$. Now, we may introduce Matsubara Green's function for the free

phonons.

$$D_\lambda^0(q, \tau) = -\langle T_\tau A_{q\lambda}(\tau) A_{q\lambda}^\dagger(0) \rangle_0, \quad (2.26)$$

where T_τ is the time-ordering operator. In the frequency domain,

$$D_\lambda^0(q, iq_n) = \int_0^\beta d\tau e^{iq_n\tau} D_\lambda^0(q, \tau) \quad (2.27)$$

$$= \frac{1}{iq_n - \Omega_{q\lambda}} - \frac{1}{iq_n + \Omega_{q\lambda}} \quad (2.28)$$

$$= \frac{2\Omega_{q\lambda}}{(iq_n)^2 - (\Omega_{q\lambda})^2} \quad (2.29)$$

where iq_n are the Matsubara frequencies and $\beta \equiv T^{-1}$.

From here onwards, for simplification, we account only for longitudinal modes, thus dropping the dependency on λ . In the dispersionless case, $\Omega_q \approx \Omega$, and long wavelength limit we obtain a form for the phonon-mediated interaction that relates to the Coulomb interaction, $V(q)$, by combining (2.29) and (2.24).

$$\frac{|g_q|^2}{\mathcal{V}} D_\lambda^0(q, T) = \frac{1}{2} V(q) \frac{(\Omega)^2}{(iq_n)^2 - (\Omega)^2}. \quad (2.30)$$

From here, we can obtain the effective potential in superconductivity and show that it will be attractive. This potential is given by the sum of the bare Coulomb interaction, and the phonon-mediated interaction [45].

$$V_{eff}(q, iq_n) = V(q) + \frac{|g_q|^2}{\mathcal{V}} D_\lambda^0(q, T) = V(q) \frac{(iq_n)^2}{(iq_n)^2 - (\Omega)^2} \quad (2.31)$$

With analytical continuation ($iq_n \rightarrow \omega + i\eta$), we obtain real frequencies and note that since $V(q)$ is repulsive, the effective potential will be attractive for Matsubara frequencies lower than the plasma frequency. Similarly, we may also consider the Random Phase Approximation to renormalize the interactions to avoid divergencies coming from the Coulomb potential. We skip the derivations here but note that the renormalized potential, V_{eff}^{RPA} , has the same form as eq. (2.31).

We shall examine how a particular electron pair scattering gives rise to the instability of the ground state in superconductivity. The pair scattering vertex, Λ , is given by the infinite ladder diagram of the sum of scattering events between time-reversed electron pairs (here, $|k \uparrow\rangle$ and $| -k \downarrow\rangle$), as shown in Fig. 2.1.

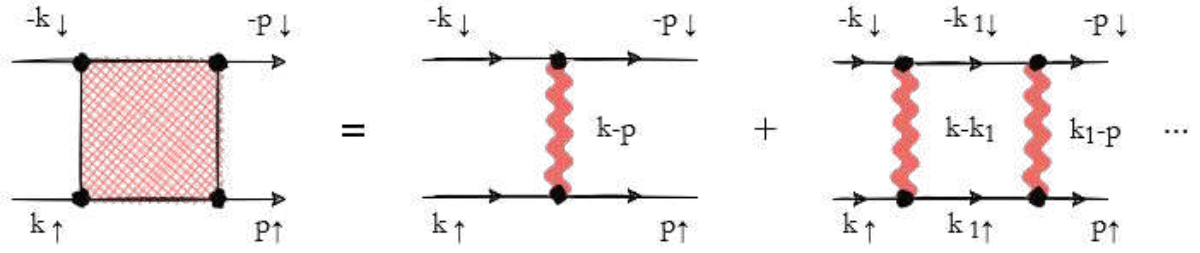


Figure 2.1: Scattering of time-reversed pairs of electrons, in diagrammatic form.

The formal correspondence of diagrams and quantities are shown in table 2.1. Here, $G_{\sigma}^0(k, ik_n)$ is the single-electron Green's function.

Diagram	Quantity
	$G_{\sigma}^0(k, ik_n)$
	$-V_{eff}^{RPA}(k-p)$
	$\Lambda(k, p)$

Table 2.1: Relevant Feynman diagrams correspondence.

We may disregard external electron propagators and write a Dyson equation for Λ , taking into account the Feynman rules for Coulomb interaction. It will take the form of a Bethe-Salpeter equation [53], as described in Fig. 2.2.

$$\Lambda(k, p) = -V_{eff}^{RPA}(k-p) + \frac{1}{\mathcal{V}\beta} \sum_q \left(-V_{eff}^{RPA}(k-q) \right) G_{\uparrow}^0(q) G_{\downarrow}^0(-q) \Lambda(q, p) \quad (2.32)$$

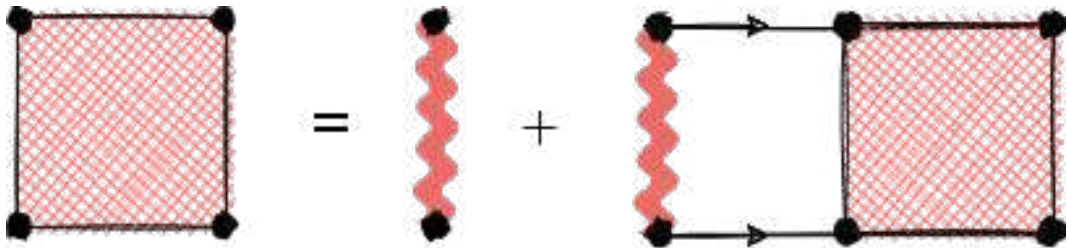


Figure 2.2: Dyson equation for the pair scattering vertex in diagrammatic form.

We are interested in analyze the attractive regime. For this purpose, we proceed by taking two

approximations: first, take into consideration that most phonons participating in this scattering process have frequencies of the order ω_D . We, thus, set $\omega_q = \omega_D$. Second, take the interaction strength, V_{eff}^{RPA} , to be constant. More specifically, $V_{eff}^{RPA} \approx -V$ for $|iq_n| < \omega_D$ and zero otherwise. The frequency ω_D , therefore, will be a cutoff. We arrive at

$$\Lambda(k, p) = V + \frac{1}{\beta} \sum_{iq_n}^{\omega_D} \frac{1}{\mathcal{V}} \sum_q V G_{\uparrow}^0(q, iq_n) G_{\downarrow}^0(-q, -iq_n) \Lambda(q, p) \quad (2.33)$$

As the right-hand side of the equation is k-independent, we have $\Lambda(k, p) = \Lambda(p)$ and will not contribute to the summation. The self-consistent solution will be constant, of the form:

$$\Lambda = \frac{V}{1 - \frac{V}{\beta} \sum_{|iq_n| < \omega_0} \frac{1}{\mathcal{V}} \sum_q G_{\uparrow}^0(q, iq_n) G_{\downarrow}^0(-q, -iq_n)} \quad (2.34)$$

The temperature dependency from β implies that $\lambda \rightarrow \infty$ for low temperatures. Therefore, the ground state is unstable below a critical temperature T_c , as bound states of time-reversed pairs of electrons are formed. This condensation happens with all electrons in the Fermi surface, since $V_{eff}^{RPA} \approx -V$ in this case.

In practice, the system can lower its energy by creating these pairs of fermions, denominated **Cooper pairs**, as the energy contribution is negative. Renormalization group analysis shows that these results hold even for a perturbative potential [45]. The phenomenon is known as **Cooper instability**.

At the critical temperature, the denominator in eq. (2.34) is zero. This yields

$$T_c \propto \exp\{-1/\mathcal{V}d(\epsilon_F)\}, \quad (2.35)$$

where $d(\epsilon_F)$ is the Density of States (DOS), ϵ_F is the Fermi energy. The exponential form showcases strong sensibility with the DOS and implies that we cannot find a different ground state via perturbation theory.

Interlude: A brief introduction to Mean-field theory - A generic second quantized form for the interaction of two different flavors of identical particles is given by

$$H = \sum_l \epsilon_A(k) a_k^\dagger a_k + \sum_m \epsilon_B(m) b_m^\dagger b_m + \sum_{ijkm} V_{ijkm} a_i^\dagger b_j^\dagger a_m b_k, \quad (2.36)$$

Consider the operator $n_{ij} = c_i^\dagger c_j$. We may write the operator in terms of its thermal average and fluctuations:

$$n_{ij} = \langle n_{ij} \rangle + \delta n_{ij} \quad (2.37)$$

where δn_{ij} is the fluctuation around the thermal average, $\langle n_{ij} \rangle$. In the particular case of zero temperature, the average is in the ground state. For the **mean-field approximation**, we keep only the terms linear in the fluctuations. This is equivalent to ignoring correlations. Rewriting eq. (2.36) in terms of eq. (2.37) and considering the mean-field approximation,

$$H = \sum_l \epsilon_A(k) n_k^a + \sum_m \epsilon_B(m) n_m^b + \sum_{ijkn} V_{ijkn} \left[n_{ik}^a \langle n_{jm}^b \rangle + n_{jm}^b \langle n_{ik}^a \rangle - \langle n_{ik}^a \rangle \langle n_{jm}^b \rangle \right]. \quad (2.38)$$

We now have one-body problems that sense and average effect coming from the other type of particle. This is more clear writing:

$$V_{ik}^A = \sum_{jm} V_{ijkm} \langle n_{jm}^b \rangle \quad (2.39)$$

$$V_{jm}^B = \sum_{ik} V_{ijkm} \langle n_{ik}^a \rangle \quad (2.40)$$

The recursive aspect of the mean-field theory is now evident. To establish the potential, we would need the state to carry out the average. However, we need the potential in order to obtain the state. The solution for the potential is, therefore, obtained self-consistently.

Mean-field theory for superconductivity

We start with the simplest effective model for superconductivity [53]:

$$H = \sum_{k\sigma} \epsilon_k \hat{n}_{k\sigma} - \frac{g}{L^d} \sum_{k,k',q} c_{k+q\uparrow}^\dagger c_{-k\downarrow}^\dagger c_{-k'+q\downarrow} c_{k'\uparrow}, \quad (2.41)$$

where g is a positive constant and L^d is a d -dimensional volume. To apply mean field techniques, we assume a ground state $|\Omega_s\rangle$, whose explicit form for this ground state will be derived shortly, to carry the mean field approximation for the interaction term. The quartic term in fermionic operators reduces to a one-body operator by introducing:

$$\Delta = \frac{g}{L^d} \sum_k \langle \Omega_s | c_{-k\downarrow} c_{k\uparrow} | \Omega_s \rangle \quad (2.42)$$

Δ is the order parameter. The denomination as an order parameter is pertinent. This band gap is crucial to explaining the different phase transitions observed in the form of condensation of the quasiparticles, which leads to the dissipationless flow of current in low energies, as excited states are energetically costly. The mean-field Hamiltonian is:

$$H \approx \sum_k \xi_k c_{k\sigma}^\dagger c_{k\sigma} - (\bar{\Delta} c_{-k\downarrow} c_{k\uparrow} + \Delta c_k^\dagger c_{-k\downarrow}^\dagger) + L^d \frac{|\Delta|^2}{g}, \quad (2.43)$$

with $\xi_k \equiv \varepsilon_k - \mu$. We can introduce a spinor of the form:

$$\psi_k = \begin{pmatrix} c_{k\uparrow} \\ c_{-k\downarrow}^\dagger \end{pmatrix} \quad (2.44)$$

and the Hamiltonian can be written as:

$$H \approx \sum_k \psi_k^\dagger \begin{pmatrix} \xi_k & -\Delta \\ -\Delta & -\xi_k \end{pmatrix} \psi_k + \sum_k \xi_k + \frac{L^d |\Delta|^2}{g} \quad (2.45)$$

we can now diagonalize the Hamiltonian using fermionic quasiparticle operators ($a_{k,\uparrow}, a_{-k,\downarrow}^\dagger$) that are linear combinations of the previous ones. The spinorial form of the Dirac Fermions are denominated **Nambu spinors**.

$$\begin{pmatrix} a_{k\uparrow} \\ a_{-k\downarrow}^\dagger \end{pmatrix} = \begin{pmatrix} \cos \theta_k & \sin \theta_k \\ \sin \theta_k & -\cos \theta_k \end{pmatrix} \begin{pmatrix} c_{k\uparrow} \\ c_{-k\downarrow}^\dagger \end{pmatrix} \quad (2.46)$$

With $|\Omega\rangle$ being the fermionic vacuum, we obtain the superconducting ground state, $|\Omega_s\rangle$, as the vacuum defined by the Bogoliubov quasiparticles.

$$|\Omega_s\rangle = \prod_k a_{k\uparrow} a_{-k\downarrow} |\Omega\rangle \propto \prod_k (\cos \theta_k - \sin \theta_k c_{k\uparrow}^\dagger c_{-k\downarrow}^\dagger) |\Omega\rangle \quad (2.47)$$

2.1.4 Bogoliubov-de Gennes (BdG)

Although some ideas associated with this formalism were explored in the previous section, such as the usage of spinor structure in a mean-field Hamiltonian, the Bogoliubov-de Gennes formalism will be used extensively throughout this thesis and deserves a standalone section.

To understand the capabilities of this formalism, let us start with a metallic Hamiltonian and

increment a superconducting pairing afterward. In the second quantized form, we have

$$H_{metal} = \sum_{\sigma,p} c_{\sigma,p}^\dagger \epsilon(p) c_{\sigma,p}, \quad (2.48)$$

where $c_{\sigma,p}^\dagger$ is the creation operation of a fermion with momentum p and spin σ . We can use fermionic anticommutation relations to manipulate the expression (2.48) in order to separate negative and positive momentum contributions:

$$H_{metal} = \frac{1}{2} \sum_{\sigma,p} [\epsilon(p) c_{\sigma,p}^\dagger c_{\sigma,p} - \epsilon(-p) c_{\sigma,-p} c_{\sigma,-p}^\dagger] + \frac{1}{2} \sum_p \epsilon(p). \quad (2.49)$$

We can now introduce the spinor:

$$\Psi_p = \begin{pmatrix} c_{\uparrow,p} \\ c_{\downarrow,p} \\ c_{\uparrow,-p}^\dagger \\ c_{\downarrow,-p}^\dagger \end{pmatrix}. \quad (2.50)$$

Making use of spinor structures, the Hamiltonian, up to a constant term, is now:

$$H_{metal} = \frac{1}{2} \sum_p \Psi_p^\dagger H_{BdG}(p) \Psi_p, \quad (2.51)$$

with

$$H_{BdG} = \begin{pmatrix} \epsilon(p) & 0 & 0 & 0 \\ 0 & \epsilon(p) & 0 & 0 \\ 0 & 0 & -\epsilon(-p) & 0 \\ 0 & 0 & 0 & -\epsilon(-p) \end{pmatrix}. \quad (2.52)$$

Considering now the pair potential, H_{pair} , that creates and annihilates fermions in pairs of opposite spins, the Cooper pairs. Note that, in the many-body formalism, the pairing is a two-body term, it should be quartic on ladder operators. However, we are already implicitly using mean-field theory to encapsulate the contributions in an average way, such that $\Delta \propto \langle c_{\downarrow,-p} c_{\uparrow,p} \rangle$,

in accordance to eq. (2.42).

$$H_{pair} = \sum_p \Delta (c_{\uparrow,p}^\dagger c_{\downarrow,-p}^\dagger + \text{h. c.}). \quad (2.53)$$

This particular form of pairing, independent of momentum, is called **s-wave superconductivity**.

The full Hamiltonian, $H = H_{metal} + H_{pair}$ is:

$$H_{BdG} = \begin{pmatrix} \epsilon(p) & 0 & 0 & \Delta \\ 0 & \epsilon(p) & -\Delta & 0 \\ 0 & -\Delta^* & -\epsilon(-p) & 0 \\ \Delta^* & 0 & 0 & -\epsilon(-p) \end{pmatrix}. \quad (2.54)$$

This Hamiltonian is structured to act on the tensor product of spin and particle/hole Hilbert spaces. Eq. (2.54), for instance, can be written as:

$$H_{BdG} = \epsilon(p)\tau_z \otimes \mathbb{I}_2 - \text{Re}(\Delta)\tau_y \otimes \sigma_y - \text{Im}(\Delta)\tau_x \otimes \sigma_x, \quad (2.55)$$

where σ_i are the Pauli spin matrices and τ_i , also known as ‘‘Nambu basis’’, are the analogous structure in particle/hole space [24]. The solution for H_{BdG} will result in linear combinations of creation and annihilation operators (Bogoliubov quasiparticles).

In some instances, those quasiparticles will obey Majorana statistics, as we shall see in the section 2.5. This is the case for **p-wave superconductivity**, where the pairing potential is linear in the momentum k . The one-dimensional spinless p-wave superconductor is known as Kitaev’s toy lattice model. In real space, it is expressed as:

$$H = -\mu \sum_x c_x^\dagger c_x - \frac{1}{2} \sum_x (t c_x^\dagger c_{x+1} + \Delta \sum_x e^{i\phi} c_x^\dagger c_{x+1}^\dagger), \quad (2.56)$$

where t is the intensity of the hopping to nearest neighbors, μ is the chemical potential and Δ is the superconducting pairing. Note that the fermionic operators are necessarily spinless, as required by the antisymmetry of the total fermionic wavefunction.

More general pairing potentials are possible but beyond this thesis’s scope. Inspired by atomic orbitals terminology, we may have s -, p -, d - and f -wave pairings, corresponding to $l = 0, 1, 2$ and 3 in total spin angular momentum of the Cooper pairs [54].

In section 2.5, we explore bulk-boundary correspondence in this system and how such a

model can host topological modes [55]. Nevertheless, prior to this, we will need to introduce relevant concepts of Topology and their relationships with condensed matter.

2.2 Algebraic-Topology Aspects in Physics

In Physics, Topology is often associated with Differential Topology, which is particularly useful in General Relativity. In Condensed Matter, however, we focus on a different subfield, Algebraic Topology, which mainly studies topological spaces and how to understand equivalences between them in a quantitative manner.

In this work, algebraic Topology appears in many different senses in the field of Topological Quantum Computation and Condensed Matter. It is useful to overview relevant mathematical definitions and illustrate their applications in our physical context, as well as distinguish some definitions that appear in both physics and mathematics, such as the concept of vortices.

Let us start by defining the key concept in this subarea. Let X be a set. For a certain collection of its subsets, given by τ , we consider (X, τ) to be a **topological space** if it satisfies the axioms:

- i) \emptyset and X belongs to τ
- ii) A finite or infinite union of elements of τ also belongs to τ .
- iii) A finite intersection of elements of τ also belongs to τ .

A **homeomorphism** is a continuous map $F \rightarrow G$ in which the inverse is also continuous. A map $f: X \rightarrow Y$, with X, Y being topological spaces, is continuous if the inverse image of an open set in Y is an open set in X .

Thus, two topological spaces are homeomorphic to each other if we can deform one into the other continuously. For geometrical visualization, this can be thought of as modifying the shape without cutting it [56].

A way to quantify this equivalence is to establish **topological invariants**, a quantity that won't change under continuous deformation. A simple example of a topological invariant is the Euler characteristic, χ . In Geometry, for a convex polyhedron:

$$\chi = V - E + F. \tag{2.57}$$

Here, χ is a topological invariant that encapsulates information about the number of vertices (V), edges (E) and faces (F) of any solid, even if continuously deformed. In Physics, it can be shown, although not demonstrated here, that two gapped systems are considered equivalent if they can be continuously deformed into one another without closing the gap [23].

For two topological spaces that are homeomorphic, there may be a class of maps that can perform these deformations. The continuous deformation between those maps themselves is

called a **homotopy**. Formally, with X and Y being topological spaces, a homotopy from the continuous map f to the continuous map g is a continuous function $F_t: X \rightarrow Y$, with $t \in [0, 1]$, with $F_0 = f$ and $F_1 = g$.

Finally, the **fundamental group** π_1 of a topological space is the collection of all loops (i.e., closed paths) that are homotopic ². In particular, for a circle (usually denoted as S^1), the different classes of loops are characterized by their winding number, which denotes the number of times the loop wind around the circle [45].

2.2.1 Topology and Exchange statistics in (2+1)D

To understand the remarkable effects of dimensionality for exchange statistics due to topology, we rely on the concept of homotopy. For concrete visualization in two dimensions, we can imagine a surface of any shape containing a hole somewhere. When restricted to R^2 , we will have classes of loops that can be shrunk into a point and a class that cannot, depending on whether the loop encloses the hole. Those are examples of different homotopy classes.

Particularly in superconductors, one can consider a complex order parameter, $\Delta(x)e^{i\phi(x)}$. The phase maps the parameter onto S^1 . Parameters of this form are called "vortex-like". In the surface of a superconductor, dimensionality limitations will differentiate loops in different homotopy classes – it corresponds to instances in which the order parameter is not uniquely defined, and a winding number can be associated with it. As the winding number is an integer, for vortices, we have $\pi_1(S^1) = \mathbb{Z}$ [56]. Counter/clockwise winding in real space will encompass the topological charge $q = \pm 1$, respectively [45].

In the presence of vortices and confined to (2+1) dimensions, non-trivial topology is manifested by the emergence of Anyons. These excitations have fractional statistics, i.e., after an exchange operation, the application of the parity operator renders an eigenvalue that is neither -1, as for fermions, nor +1, as for bosons, but a more general complex phase; hence the name "Any-ons" [56], [57].

2.2.2 Braiding

We can think of the commutation process of a pair of anyons in terms of the mutual swapping between their worldlines, an operation denoted as "braiding" ³. For our purposes, we shall focus

²The fundamental group is defined as a group for being closed under operations of concatenation of loops.

³This is not the only interpretation; we discuss how braiding does not need to occur in real space in 2.7.1

on group-theoretical aspects of braiding, but it should be noted that this is yet another aspect of Algebraic Topology in Condensed Matter, as braiding is a subject of study in Knot Theory. For a better definition of mathematical properties and schematical visualization of braiding operations, refer to Appendix A.

An intriguing subset of anyonic particles is the **non-abelian anyons**, where different braiding operations are non-commutative. The braiding operations in two dimensions on non-abelian anyons are unitary matrices. In this section, we show how those operations could be used for quantum computation, acting as one-qubit quantum gates, which are also based on unitary, two-dimensional matrices⁴. To illustrate this, we follow a review on the subject [29].

On an abstract level, we consider here a two-dimensional system with vortices containing anyons. In the following subsection, we will delve into details of the physical system, a two-dimensional topological superconductor.

We begin by writing the fermionic operators, c^\dagger and c , as linear combinations of two other operators, denoted by γ_i :

$$c_{kl}^\dagger = \frac{1}{2}(\gamma_k + i\gamma_l) \quad (2.58)$$

$$c_{kl} = \frac{1}{2}(\gamma_k - i\gamma_l). \quad (2.59)$$

Using the canonical anticommutation relations of fermions, we notice that $\{c_{kl}^\dagger, c_{kl}\} = 1 \rightarrow \gamma_k^2 = 1$ and $\{c_{kl}, c_{kl}\} = 0 \rightarrow \gamma_k\gamma_l = -\gamma_l\gamma_k, k \neq l$. The operators γ_k and γ_l following this algebra are the **Majorana fermions** corresponding to those Dirac fermions. Note that the fermionic operators have two indexes, identifying the individual contributions of each Majorana.

Majorana fermions are real solutions to Dirac's equation, implying that its antiparticle is the particle itself. Majorana fermions bound to topological defects in superconductors are named Majorana Zero Mode (MZM). They correspond to degenerated ground state solutions from BCS Hamiltonian.

Two define a two-level system as a basis for a topological qubit, we use the Parity observable. It is instructive to start by defining the Parity operator for Dirac fermions. For each pair of vortices, indexed by k and l , the Parity P_{kl} is

$$P_{kl} = 1 - 2c_{kl}^\dagger c_{kl}, \quad (2.60)$$

⁴Refer to Appendix B for an overview of the circuit model of quantum computation.

where c_{kl}^\dagger and c_{kl} are the operators of creation and annihilation of Dirac fermions. We have even parity (+1 eigenvalue for the Parity operator) when $n_{kl} \equiv c_{kl}^\dagger c_{kl} = 0$, i.e., when this level is not occupied, and we have odd parity when it is occupied.

Initializing with two vortices, one of them with occupation and the other unoccupied, despite not having local contact between the vortices, the fermion will "jump" from one vortex to the other. This unpaired fermion, due to Pauli's exclusion principle, will fill the lower energy level, so the parity will be even since the population of this level will be completely paired or will jump to a higher level, resulting in odd parity. We will define even parity state as $|+\rangle$ and odd parity as $|-\rangle$.

The parity operator can now be written in terms of MZMs as:

$$P_{kl} = 1 - \frac{1}{2}(\gamma_k + i\gamma_l)(\gamma_k - i\gamma_l) = i\gamma_k\gamma_l. \quad (2.61)$$

We can define a two-level system for this configuration of four vortices as:

$$|0\rangle \equiv |+\rangle |-\rangle \quad (2.62)$$

$$|1\rangle \equiv |-\rangle |+\rangle, \quad (2.63)$$

where both states have odd total parity (considering the products of the parities in pairs). Alternatively, it would be also possible to define $|0\rangle \equiv |+\rangle |-\rangle$, $|1\rangle \equiv |-\rangle |+\rangle$, with even total parity, in an independent fashion, since different parities commute, resulting in uncorrelated subspaces.

Given this definition for odd parity, we can explore how certain operations of Majorana fermions swapping can lead to Pauli matrices. First, let us consider a situation with four vortices in which the parity of the two first fermions is even and the two last fermions, odd ($P_{12} = 1$ e $P_{34} = -1$). When we circle γ_2 around γ_3 , both parities swap signs, ($P_{12} \rightarrow -1$ e $P_{34} \rightarrow 1$). This can be seen in terms of Dirac fermions. We have:

$$P_{23} = i\gamma_2\gamma_3 = -c_{12}c_{34}^\dagger - c_{12}c_{34} + c_{12}^\dagger c_{34}^\dagger + c_{12}^\dagger c_{34}. \quad (2.64)$$

Therefore,

$$P_{23} |0\rangle = P_{23} |+\rangle |-\rangle = |-\rangle |+\rangle = |1\rangle. \quad (2.65)$$

Similarly, up to a global phase, $P_{23} |1\rangle = |-\rangle |+\rangle = |0\rangle$. In our qubit definition, we have a "bit

flip", i.e., we have the equivalent as a σ_x operation, represented in Bloch's sphere as a $\theta = \pi$ rotation. Bit rotations can be written in a general manner as:

$$U = e^{i\beta} e^{-\frac{i\theta}{2} \hat{n} \cdot \sigma}, \quad (2.66)$$

where β is a phase. If we define $\beta = \frac{\pi}{2}$, we note that the "half-braiding" (or exchange) operation B_{23} is equivalent to perform half of the operation, thus it is given by the square root spin flip:

$$B_{2,3} = \exp\left(\frac{i\pi}{4}(\mathbb{I} - \sigma_x)\right). \quad (2.67)$$

Expanding $e^{-i\pi\sigma_x/4}$ in power series and substituting $i\gamma_2\gamma_3 = \sigma_x$:

$$B_{2,3} = \sqrt{\frac{i}{2}} (\mathbb{I} + \gamma_2\gamma_3). \quad (2.68)$$

Analyzing now the half-braiding of Majoranas in a same pair, such as γ_1 and γ_2 . Applying $P_{12} = i\gamma_1\gamma_2$ in the qubits:

$$P_{12} |0\rangle \equiv |+\rangle |-\rangle, P_{12} |1\rangle \equiv -|-\rangle |+\rangle. \quad (2.69)$$

Thus, $i\gamma_1\gamma_2$ acts as a phase flip, or σ_z . So, we define B_{12} :

$$B_{12} = \exp\left(\frac{i\pi}{4}(1 - \sigma_z)\right) = \frac{1}{\sqrt{2}} (\mathbb{I} + \gamma_1\gamma_2). \quad (2.70)$$

It is important to notice that B_{12} and B_{23} do not commute,

$$[B_{12}, B_{23}] = i\gamma_1\gamma_3, \quad (2.71)$$

which shows that the exchange operations are non-abelian.

Having spin-flip and bit-flip, we can create many important logical gates for single qubits, such as Hadamard. However, to achieve universal quantum computation (to be able to perform any computational operation), it is necessary a universal set of gates, as detailed in Appendix B.

For the gates mentioned, we would obtain it by adding the T-gate ($\pi/8$ gate). However, this gate cannot be performed through braiding, since the minimal operation possible, exchange, corresponds to an angle of $\pi/4$.

It is worth mentioning that not all braiding processes imply topological protection. First, braiding is also defined for abelian anyons; in this case, the operation results in a scalar phase, not being relevant for quantum computing, for instance [58], [59]. Moreover, even when non abelian braiding is detected, protection is not necessarily guaranteed, as further explained in Appendix C.

2.3 Symmetries in Condensed Matter

Symmetry aspects are generally associated with profound physics consequences, as illustrated by Noether's theorem for conservation laws. In condensed matter, the idea of symmetry appears in a multitude of contexts. Most notably, in solid-state physics, continuous translational-symmetry breaking is what defines a crystal. In the context of topological matter, it is useful to detail the construction and implication of three types of symmetries: Time-reversal, Particle-Hole and Chirality.

Time-reversal, \mathcal{T} : A Hamiltonian possesses Time-reversal (TR) symmetry when it is invariant under the application of the operator $\mathcal{T} = U\mathcal{K}$, where U is a unitary matrix and \mathcal{K} is the complex conjugation operator. The Hamiltonian, in this case, is composed of real entries. It follows that:

$$\mathcal{T}H^*\mathcal{T}^\dagger = H. \quad (2.72)$$

It can be shown that a TR-preserving Hamiltonian will be at least doubly degenerate. One way to break degenerescence is adding a magnetic term of Zeeman type, $V_z = V_0\sigma_z$, since the Pauli matrices do not commute.

Particle-Hole, \mathcal{P} : To understand this symmetry, it is useful to recall the Bogouliubov-de Gennes Hamiltonian, where a fermionic Hamiltonian can be written in terms of spinors, as done in the p -wave develop section 2.5. A Hamiltonian is particle-hole symmetric when, in its BdG form, it is invariant under:

$$\mathcal{P} = \tau_x\mathcal{K}. \quad (2.73)$$

where τ_x is the x -component in Nambu basis. A Hamiltonian is particle-hole symmetric when obeys

$$\mathcal{P}H^*\mathcal{P}^\dagger = -H. \quad (2.74)$$

A consequence of Particle-Hole invariance is a symmetric spectrum around zero energy.

Chirality, \mathcal{S} : Also known as sublattice symmetry, it is defined as the product of the two previous symmetry operators [23].

$$\mathcal{S} = C\mathcal{P}. \quad (2.75)$$

One consequence of chirality is a symmetric spectrum with no gap closings.

By considering these symmetries, it is possible to create a classification of topological matter, also known as the ten-fold way, as shown in Table 2.2. The class nomenclature is inspired by E. Cartan's classification of symmetry spaces [60].

Class	C	\mathcal{P}	\mathcal{T}
A			
AIII	1		
AI			1
BDI	1	1	1
D		1	
DIII	1	1	-1
AII			-1
CII	1	-1	-1
C		-1	
CI	1	-1	1

Table 2.2: Classes of topological systems based on chiral, particle-hole and time-reversal symmetries. Missing entries represent the absence of the corresponding symmetry. The other entries represent the value of the corresponding symmetry operator squared.

Further classification can be done based on topological aspects. In terms of the group representation of the topological invariant present in the Hamiltonian, we denote \mathbb{Z} when the topological invariant belongs to the set of Integers, while $2\mathbb{Z}$ corresponds to even integers. As an example of \mathbb{Z} topological invariant, we have the winding number, present in vortices in superconductors.

Another classification is \mathbb{Z}_2 , the cyclic group of order 2. The invariant in \mathbb{Z}_n follows arithmetic modulo n . In this category, we have only two possible topological states, as the topological invariant may assume two values.

An example of this case is the Pfaffian. The Pfaffian of a skew-symmetric matrix A is defined as:

$$\text{Pf}(A)^2 = \det A. \quad (2.76)$$

As shown in 2.2.2, we may associate four MZMs states with two Parity eigenstates, associated with even or odd parity or, equivalently, to occupied or unoccupied fermionic state. In the ground state, the action of a single Majorana quasiparticle flips the parity of the state. Such **femionic parity switches** can be understood as level crossings. The Pfaffian invariant, Q , is defined as:

$$Q_{BdG} = \text{sign}(\text{Pf}(iM^T H_{BdG} M)) \quad (2.77)$$

with M being the unitary

$$M = \begin{pmatrix} 1 & -i \\ 1 & i \end{pmatrix}. \quad (2.78)$$

Q can be ± 1 , indeed belonging to \mathbb{Z}_2 .

The $M^T H_{BdG} M$ form results in an antisymmetric matrix, characterized by having doubled eigenstates, in conformity to the particle-hole symmetry of the Hamiltonian. From the definition of the Pfaffian, eq. (2.76), we may note that a sign change in a single eigenstate, which corresponds to a level crossing, will change the sign in Q_{BdG} . Therefore, the Pfaffian is an adequate topological invariant to account for the crossings.

We may now expand the ten-fold way to include the topological invariants in different dimensions, as shown in Table 2.3.

Class	C	\mathcal{P}	\mathcal{T}	0	1	2	3
A				\mathbb{Z}		\mathbb{Z}	
AIII	1				\mathbb{Z}		\mathbb{Z}
AI			1	\mathbb{Z}			
BDI	1	1	1	\mathbb{Z}_2	\mathbb{Z}		
D		1		\mathbb{Z}_2	\mathbb{Z}_2	\mathbb{Z}	
DIII	1	1	-1		\mathbb{Z}_2	\mathbb{Z}_2	\mathbb{Z}
AII			-1	$2\mathbb{Z}$		\mathbb{Z}_2	\mathbb{Z}_2
CII	1	-1	-1		$2\mathbb{Z}$		\mathbb{Z}_2
C		-1				$2\mathbb{Z}$	
CI	1	-1	1				$2\mathbb{Z}$

Table 2.3: Classes of topological systems based on symmetries and topological invariants in dimensions $d = 0, 1, 2, 3$.

Such classification is useful to understand the consequences of dimensionality reduction and/or symmetry breaking of relevant symmetries. Furthermore, the periodic structure hints at the possibility of finding new physical realizations in each of the entries. In chapter 4, we discuss how different it is possible to build Hamiltonians with symmetry constraints in mind to generate the desired topological phenomena.

2.4 Physical Systems Hosting Anyons

Non-abelian anyons are predicted to exist in two systems that are currently under extensive experimental investigation: the two-dimensional electron fluid with external magnetic field in the Fractional Quantum Hall (FQH) regime, and in a topological superconductor with vortices [25], [61], [62].

In this section, we introduce the Fractional Quantum Hall Effect (FQHE) and compare, in terms of anyonic features, with topological superconductivity. As the focus of the present thesis is on topological superconductors, we postpone the detailing of this physical system for a later section.

Similarly to the integer quantum Hall effect, the main footprint of the FQHE is the quantized plateaus in Hall conductivity, σ_{xy} , proportional to e^2/h . Explicitly,

$$\sigma_{xy} = \frac{e^2}{2\pi} \nu \tag{2.79}$$

In the FQHE case, the filling factor ν possess fractional values.

Discovered around the 1980s, the phenomenon was understood by Robert Laughlin by considering a many-body trial function for the ground state of the system with $\nu = 1/m$, with m odd [63]. More general fractions were later established by Duncan Haldane and Bertrand Halperin [64], [65].

Topology in this system manifests in a different way than what was previously presented. In interacting systems, the ten-fold way characterization is no longer sufficient. The FQHE is an example of **topologically ordered** system, while previously, we examined **symmetry protected** systems in section 2.3. Symmetry-protected systems do not maintain topological protection under the breaking of the necessary symmetry. In topological ordered systems, in other hand, topology is not associated with symmetry breaking: the phase transition of a normal two-dimensional electron gas to an FQHE state is not described via symmetry breaking [23].

These specific anyons arising in the FQHE are called "Fibonacci" anyons. [66]. Fibonacci anyons allow for universal quantum computation, unlike Ising anyons, which arise in topological superconductors with vortices. To fully realize all possible quantum computing operations, Ising anyon-based qubits require extra elements. One possible implementation relies on using Majoranas in nanowires along with superconductors' degrees of freedom [67]. Another possibility is to couple with a quantum dot [68].

The experimental difficulties presented by FQH systems pose as motivation to work with topological superconductors. In such systems, non-abelian anyons are predicted to appear in well-separated ends of a nanowire or in vortices in two-dimensional setups. The minimal system in which these quasiparticles may arise, the p -wave superconductivity, will be discussed next. Systems with engineered topological superconductivity will be treated in chapter 4.

2.5 Topological superconductivity: p -wave pairing

The physical system described in the section 2.1.4, free electrons with s-wave superconductivity, is a topologically trivial system. In this section, we refer to a different type of superconductivity to observe topological effects, the **p -wave superconductivity**, where the pairing potential is linear in the momentum k .

In this section, we follow the development in reference [1]. We shall study the case of a one-dimensional spinless p -wave superconductor, which is the simplest model that supports a topological phase. To make sense of the Hamiltonian, we will start with Kitaev's toy lattice model in real space:

$$H = -\mu \sum_x c_x^\dagger c_x - \frac{1}{2} \left[\sum_x t c_x^\dagger c_{x+1} + (\Delta \sum_x e^{i\phi} c_x^\dagger c_{x+1}^\dagger + \text{h.c.}) \right], \quad (2.80)$$

where t is the intensity of the hopping to nearest neighbors, μ is the chemical potential and Δ is the order parameter, as previously presented in section 2.1.4.

We restrain our studies to the bulk part of the system by introducing periodic conditions, we can now write a diagonalized form in momentum space as:

$$H = \sum_k E_{bulk}(k) a_k^\dagger a_k, \quad (2.81)$$

with $E_{bulk}(k) = \sqrt{(-t \cos k - \mu)^2 + |\tilde{\Delta}_k|^2}$ and where the quasiparticle operators are given by a linear combination of particles and holes, $a_k \propto c_k + c_{-k}^\dagger$.

In the gapped regime, we will have strong pairing (for $\mu < -t$) and weak pairing ($|\mu| > t$). We are now able to show that the weak coupling gives rise to a nontrivial topological regime. We can write the hamiltonian, eq. (2.56), in Bogoliubov-de Gennes form:

$$H = \frac{1}{2} \sum_k C_k^\dagger \mathcal{H}_k C_k, \quad \mathcal{H}_k = \begin{pmatrix} \epsilon_k & \tilde{\Delta}_k^* \\ \tilde{\Delta}_k & -\epsilon_k \end{pmatrix}. \quad (2.82)$$

Here, $\epsilon_k \equiv -t \cos k - \mu$. We can decompose \mathcal{H}_k in Pauli matrices as $\mathcal{H}_k = h(k) \cdot \sigma$, where $h(k)$ is a general vector embedding the momentum dependency and $\sigma = \sigma_x \hat{x} + \sigma_y \hat{y} + \sigma_z \hat{z}$, $\sigma_i, i = x, y, z$ are the Pauli Matrices. Due to charge conjugation symmetry, further explained in section 2.73,

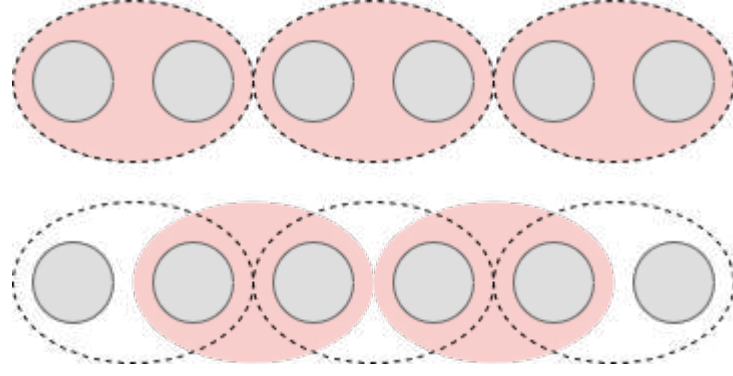


Figure 2.3: Trivial (above) and topological (below) regimes in a Kitaev chain. The circles represent Majorana particles in a chain. The dashed ovals represent the Fermions encompassing two Majorana particles each. The pink oval represents the non-zero hopping terms. In the topological regime, the end Majorana particles are not connected to the Hamiltonian, having zero energy.

we will have limitations for the values of $h(k)$:

$$\begin{aligned} h_{x,y}(k) &= -h_{x,y}(-k) \\ h_z(k) &= h_z(-k). \end{aligned} \tag{2.83}$$

Writing $h(k)$ as a vector, mapping the Brillouin Zone into a sphere, the limitations above will imply that we can write $\hat{h}_{x,y}(0) = s_0 \hat{z}$ and $\hat{h}_z(\pi) = s_\pi \hat{z}$. Then, running k from 0 to π , we can have a **closed** path coming from the north pole and getting back to the same point (for $s_0 = s_\pi$) or an **open** path arising from the north pole and ending at the south (for $s_0 = -s_\pi$).

We can establish a topological invariant:

$$\nu = s_0 s_\pi. \tag{2.84}$$

Fig. 2.3 shows a diagrammatic representation of the trivial and topological regimes. Analyzing the Bloch-like sphere in Fig. 2.4, it is noticeable that the path for $\nu = +1$ is topologically trivial since it can be deformed to a point in the north pole, while the path for $\nu = -1$ is not. The nontrivial case corresponds to the weak pairing regime. In this situation, unpaired Majoranas can be found on both edges of the chain.

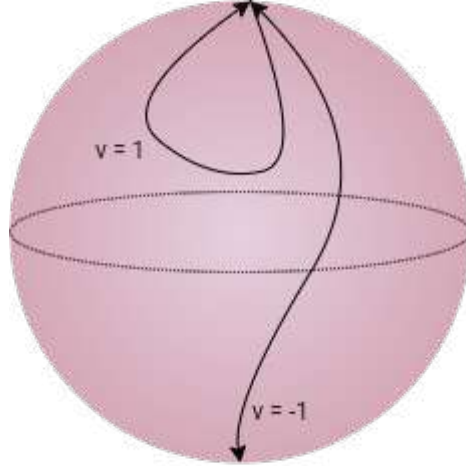


Figure 2.4: The two possible types of trajectories in the unit sphere as k go from 0 to π and their corresponding topological invariant.

2.5.1 Majorana States

Majorana particles are most succinctly known to be a particle that is their own anti-particle [26]. Conceptualized by Ettore Majorana, is of interest in both condensed matter and particle physics. For the latter, it may be one of the possible candidates for neutrinos [69]. For the former, it is the basis for topological effects in certain systems supporting anyons.

In topological superconductors, the non-trivial states obey Majorana properties. This can be seen by noting that the zero-energy solution in a BdG Hamiltonian representing superconductivity can be written as being composed by a linear combination of quasiparticles $\gamma_{i,x}$:

$$c_x \propto \gamma_{B,x} + i\gamma_{A,x}. \quad (2.85)$$

Using the canonical algebra for Fermions, we note that such that $\gamma_{i,x} = \gamma_{i,x}^\dagger$ and $\gamma_{i,x}, \gamma_{i',x'} = 2\delta_{ii'}\delta_{xx'}$, which are the canonical relations for Majoranas.

Note that the first condition implies that the Majorana particles are real particles. In contrast, as the Dirac Fermions are composed of a linear combination of the form of eq. (2.85), they are also known as "complex Fermions".

However, this is not applicable when the fermionic operator embeds spin degrees of freedom, as it is the case of s -wave superconductivity. The path to overcoming this difficulty for s -wave systems and obtaining Majorana modes will be covered in the next chapter.

Another relevant characteristic for these states to be understood as Majorana is their charge-neutral property. This is a natural consequence in superconductors, as particle-hole symmetry is

present [70]. Charge conjugation is a necessary property for a particle to be its own antiparticle.

Vortices in (2+1) dimensions chiral p -wave superconductors Majoranas are predicted to appear in the core of the superconductor's vortices in the topological regime. In domain walls, Majoranas tend to appear as chiral edges. To understand why it makes sense to find a single Majorana mode inside a vortex as well, we need to take into consideration that a magnetic flux has the ability to change the boundary conditions in the system to periodic to anti-periodic, in an analogous way as the Aharonov-Bohm effect [24]. This can be seen in a simpler manner by remembering the tight binding form of the Kitaev chain being closed, in the presence of a magnetic field. The field is incorporated in the tight binding form of the Hamiltonian via Peierls substitution ⁵:

$$t \rightarrow te^{i\phi/2}, \quad (2.86)$$

and have this phase related to the superconducting flux, $\Phi_0 = 2e/h$ as $\phi = 2\pi\Phi/\Phi_0$.

When $\Phi = \Phi_0$, we have $t \rightarrow -t$ and anti-periodic conditions. This is precisely what happens in the presence of vortices, which enclose a flux Φ_0 . Vortices can be injected in systems in this manner since a π -flux changes the phase of the order parameter and creates a vortex [72].

In polar coordinates, the appropriate BdG Hamiltonian is [24]:

$$H_{BdG} = \begin{pmatrix} -\mu & |\Delta(r)|e^{i\theta}\frac{\partial}{\partial r} + \frac{i}{r}\frac{\partial}{\partial\theta} \\ -|\Delta(r)|e^{-i\theta}\frac{\partial}{\partial r} - \frac{i}{r}\frac{\partial}{\partial\theta} & \mu \end{pmatrix}. \quad (2.87)$$

Here, our vortex profile is gauge-transform to allow for anti-periodic boundary conditions. Solving for zero energy, we obtain solutions of the form:

$$\phi(r, \theta) \propto \frac{1}{\sqrt{r}} \int_0^r \left(\frac{\mu(r')}{|\Delta(r')|} dr' \right) \begin{pmatrix} -e^{i\theta/2} \\ e^{-i\theta/2} \end{pmatrix} \equiv f(r) \begin{pmatrix} -e^{i\theta/2} \\ e^{-i\theta/2} \end{pmatrix}. \quad (2.88)$$

This function $f(r)$ is centered in the vortex core, at $r = 0$.

⁵The addition of a phase in the hopping terms of a tight-binding Hamiltonian can be shown to be in conformity with adding a magnetic term in the continuous Hamiltonian [71]

2.6 Majorana signatures

Majorana particles possess well established characteristics in theory: they are zero-energy states that, due to particle-hole symmetry, also have zero charge. Furthermore, the total parity in Majorana systems is conserved.

In practice, the detection of such properties requires careful experimental analysis. Even combining experimental tests may not be enough to unequivocally detect Majorana character [3], [73]. In this section, we describe the main three types of sought-after signatures in experiments. Limitations and difficulties of pursuing such signatures will be discussed throughout the thesis.

2.6.1 Quantized conductance

When Majorana bound states are present in superconductors, we expect perfect Andreev reflection, i.e., that incident electrons will be reflected as holes and vice-versa.

In a junction, the scattering matrix is given by

$$R = \begin{pmatrix} r_{ee} & r_{eh} \\ r_{he} & r_{hh} \end{pmatrix}, \quad (2.89)$$

where r_{ij} is the reflection coefficient for a incident particle i – electron (e) or hole (h) – being reflected as a particle j (electron or hole). The linear conductance, G , is given by:

$$G = \frac{2e^2}{h} \text{Tr} [r_{eh} r_{eh}^\dagger]. \quad (2.90)$$

Particle-hole symmetry implies that $r_{ee} = r_{hh}^*$ and $r_{eh} = r_{he}^*$. As the reflection matrix is unitary by definition, we have $\det(R) = \pm 1$. In practice, we will have either normal reflection (electron-to-electron or hole-to-hole) or Andreev reflection.

For different energy levels n and quantum point contact geometry, we arrive at the following quantized form for the conductance:

$$G = \frac{4e^2}{h} n, \quad (2.91)$$

with $n = 0, 1, \dots$ for a trivial system and $n = 1/2, 3/2, \dots$ for a topological system [70], [74].

2.6.2 Zero bias peaks

The zero-bias peak (ZBP) as a signature follows directly from the quantized conductance property. In low temperatures, following from eq. (2.91), when the bias V is zero, we expect perfect Andreev reflection and an I-V characteristic as:

$$\frac{dI}{dV} = \frac{2e^2}{h} \frac{\Gamma^2}{eV^2 + \Gamma^2}. \quad (2.92)$$

This means that we can observe a zero-bias peak in conductance, which can be measured via Scanning Tunneling Microscopy, an experimental probing method that will be discussed in the subsequent section.

The main issue with this particular signature is the many possible origins, not necessarily topological in nature, of a zero-bias peak. For instance, in nanowires, a ZBP may happen in as consequence of inhomogeneous chemical, dubbed “bad regime”) or a strong disorder regime, the “ugly” regime, in contrast to the “good” topological regime [3].

Such ambiguities became of particular interest after the retraction of a paper, published in a high impact journal, that claimed to find perfect quantized conductance in semiconductor-superconductor nanowires [36]. More rigorous studies on the impact of disorder in Majorana signatures followed as consequence [35], [75].

2.6.3 Current periodicity in Josephson junctions

In Josephson junctions, two superconductor materials are separated by a normal conductor. Current may flow despite the presence of a voltage bias; this current, named Josephson current, follows:

$$I \propto \sin(\phi). \quad (2.93)$$

Therefore, the current follows a 2π periodicity in the order parameter phase difference of the two superconductors, ϕ . In the presence of Majoranas, the Hamiltonian is modified and Parity restrictions ensures that the current behaves with:

$$I \propto \sin(\phi/2). \quad (2.94)$$

This implies a 4π periodicity for the Josephson current in the presence of Majoranas.

2.7 Experimental aspects

In this section, we shall discuss experimental aspects that will be relevant to the comprehension of results in this present work. First, we delve into the proposed experiment protocols for manipulation and readout of vortices for quantum computation, in particular, braiding methods. This is relevant to understand the practical difficulties of implementing gate-based quantum computing with vortices, an issue that will be further explored in chapter 4. Moreover, we cover experimental techniques to probe Majorana zero modes in vortices that rely on energy and charge properties of the states. The techniques will be core concepts to understand chapter 3.

2.7.1 Braiding implementation protocols

To perform quantum computation, a topological qubit needs to be manipulated in order to perform braiding and, thus, serve as logic quantum gates. Different physical procedures for the manipulation have been proposed; here we discuss two fundamentally different approaches [29].

Real space protocols

Real space braiding protocols required the movement of vortices in real space, using suitable apparatus. Real space braiding is considered a difficult approach. This fame relates, in parts, to the historical development of the field of topological quantum computation being more focused on nanowires rather than two-dimensional systems. In nanowires, due to the spacial limitations of from being an almost one-dimensional setup, moving vortices would drag particles around, which may cause quasiparticle poisoning and modify the parity of the system [38]. This can be detrimental since parity is the needed observable to perform braiding. Nevertheless, methods of error correction focused on parity flips can be used to aid such procedures, as further explained in Appendix D [76], [77].

Experimental efforts have also been made to improve the possibility of real space braiding. The advent of topological setups that are not limited to one dimension and the better understanding of materials with more appropriate parameters, such as superconductivity gap and coherence length, might be useful for implementing real space braiding.

Furthermore, not all techniques of real-space manipulation and readout of vortices rely on tunneling current. For instance, Magnetic Force Microscopy (MFM) uses magnetic force gradients and may be better in bypassing quasiparticle poisoning, besides being particularly

suitable to ferromagnetic materials [78], [79].

Measurement-based protocols

An alternative to overcome the difficulties of spacially moving vortices, the measurement-based protocol uses projective measurements to obtain topological charge information. Particular sequences of such measurements are equivalent to braiding operations, up to an overall phase.

In the case of Majoranas, being Ising anyons, projective measurements can be done via interferometry [39]. The protocol can be found in terms of Fusion rules formalism on Appendix A. Furthermore, measurement-based braiding has also been investigated in the case of quasi-majoranas ⁶, despite being trivial modes [80].

2.7.2 Probing techniques

Scanning Tunneling Microscopy

In terms of image resolution, regular optical microscopes are limited by light's wavelengths. In nanometric scales, therefore, this method is not suitable. Tunneling microscopes, in contrast, possess better resolution as they are bounded to electronic-scale properties.

In scanning tunneling microscopy (STM), images are obtained by examining the surface of a sample with a metallic tip [81]. Tip and substrate are not in contact; however, these two elements will function as electrodes in a vacuum, and the passage of current happens due to tunneling. Fig. 2.5 displays a scheme of scanning tunneling microscope above an irregular sample.

As tunneling is a function of the distance between the two electrodes, it is possible to obtain detailed topographic information about the examined material with the STM method. It is possible, for instance, to recreate a crystal's structure. The earliest experimental work on STM recreated the surface of materials such as Au(110) and Si(111) surfaces [81].

Scanning Tunneling Spectroscopy

As tunneling also depends on the electron density, information on the electronic properties of materials can also be obtained via electron scattering. Scanning Tunneling Spectroscopy adapts STM methods by fixing the tip on a specific position and varying an external voltage. Since

⁶Refer to Appendix C for more details on quasi-majorana particles.

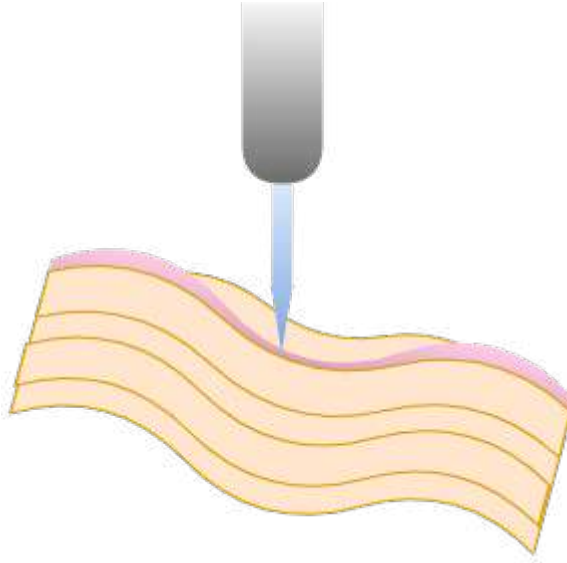


Figure 2.5: Pictoric scheme for a Scanning Tunneling Microscope. Scanning surface with different heights provide different tunneling current values.

we have a constant distance in a fixed position, any variations should be attributed to electronic properties.

Quantitatively, STS measurements evaluate the current variation in terms of voltage, also known as I-V characteristics, which is a quantity proportional to the local density of states, ρ [82].

$$\frac{dI}{dV} \propto \rho(eV).$$

Non-local STM measurements

One way to use STM apparatus to analyze the topological nature of a material is via non-local conductance, initially proposed for application to probing the nanowire setup [83]. A vortex-focused setup of uttermost importance throughout this thesis relies on using three-point contacts to carry non-local measurement of charge, q and local density of states, n [41]. The idea is to obtain a spacially-resolved mapping of both quantities and analyze the ratio $q(r)/n(r)$ in pairs of vortices to distinguish trivial and topological in-gap states in vortices. Charge is a relevant signature for Majorana quasiparticles, as particle-hole symmetry dictates that the zero-energy state must also have zero charge.

In section 3 we show how, in the presence of impurity and in the dilute limit, where vortices have enough spacial separation not to affect each other, the charge signature may still be misleading.

Chapter 3

Ambiguity of MZM signatures in the presence of scalar impurities

In this chapter, we examine the problem of potentially erroneous indications of the presence of Majorana states in fully trivial superconductivity in the presence of scalar impurities. We demonstrate that simply using high-resolution equipment may be insufficient to distinguish between these states with certainty. In fact, the anticipated broadening of energy levels may impede our ability to differentiate between Majorana states and topological trivial states that may also be present in vortices.

Many experiments to identify Majorana modes relied on measuring zero-bias peaks with scanning tunneling spectroscopy and microscopy ¹. In topological superconductors, Majorana zero modes may be found in superconducting vortices. At sufficiently low electron density, these vortices should host Majorana zero modes isolated from other in-gap states.

The fundamental challenges in verifying the presence of Majorana Zero Modes (MZMs) in vortices of topological superconductor candidates is establishing a clear distinction from other trivial states. In superconducting vortices, non-topological quasiparticle excitations are known as Caroli-de Gennes-Matricon (CdGM) states [4]. They appear in low-density superconducting materials, where vortices act as “quantum wells for quasiparticles” [84]. As previously discussed in chapter 2, for CdGM states, the spectrum given by [50] (see Fig. 3.1 (a, b)):

$$E_m = \frac{m\Delta_0}{k_F\xi}, \quad (3.1)$$

¹Check chapter 2 for a review on experimental techniques and signatures of Majorana quasiparticles.

where $m = (n + 1/2)$, n is an integer number, k_F is the Fermi momentum, ξ the bulk coherence length, and Δ_0 is the amplitude of the bulk superconducting pairing potential.

Note that the predicted spectrum of CdGM states in trivial superconductors lacks a zero-energy level. From Eq. (3.1), it is clear that an energy resolution better than $\Delta_0/k_F\xi$ is required to detect isolated excited levels. Since this resolution is accessible in state-of-the-art experiments, tunneling spectroscopy measurements of vortices on topological superconductors are expected to distinguish Majorana from trivial states [41], [85], [86]. Such differences between CdGM and MZMs spectra are taken into account for the interpretation of experimental observations of zero-bias peaks inside vortices [6], [7], [87]–[94].

We intend to challenge this assumption by considering the presence of scalar impurities on the material. Recent experiments on candidate topological superconductor materials revealed that many zero-bias peaks, associated with the presence of MZM modes, were not present in all vortices [88], [92]. Furthermore, some of the detected peaks often appeared to be stabilized by nearby magnetic [94] or scalar [89] impurities. Although it is well known that zero-bias peaks can emerge in superconductors without topological properties when magnetic impurities are present, it is still an open question whether scalar impurities may produce similar effects [95].

Motivated by this scenario, we study the effect of scalar impurities in the in-gap spectrum of a two-dimensional trivial s -wave superconductor. We chose this system because:

- (i) s -wave superconductor is a simple example of a trivial superconductor;
- (ii) the Hamiltonian does not contain additional terms that could lead to corrections from Eq. (3.1). As a result, the spectra and corresponding charge distributions can be traced back unequivocally to the presence of the impurity potential.

Moreover, influenced by the new generation of experiments in nanowires, non-local measurements with scanning tunneling microscope measurements were suggested as a way to extract the Bardeen-Cooper-Schrieffer (BCS) charge of in-gap vortex excitations [41]. Because trivial states have non-zero BCS charge whereas MZMs are strictly chargeless [70], information on the BCS charge in principle helps to distinguish CdGM states and MZMs.

Our main results are illustrated in Fig. 3.1, which compares the density of states and BCS charge for a trivial s -wave superconductor with and without an impurity potential. The calculations reveal that trivial CdGM states mimic MZM's signatures in two ways. First, electrostatic inhomogeneities shift the lowest CdGM state energy arbitrarily close to zero, as schematically shown in Figs. 3.1 (a, b). Second, as the energy separation of these states become smaller than

the experimental resolution – mainly limited by thermal broadening –, the spectral BCS charge is also suppressed, as shown in Figs. 3.1 (e, f). As a consequence, electrostatic inhomogeneities can make CdGM indistinguishable from MZMs when probed by STM experiments, given the current experimental resolutions.

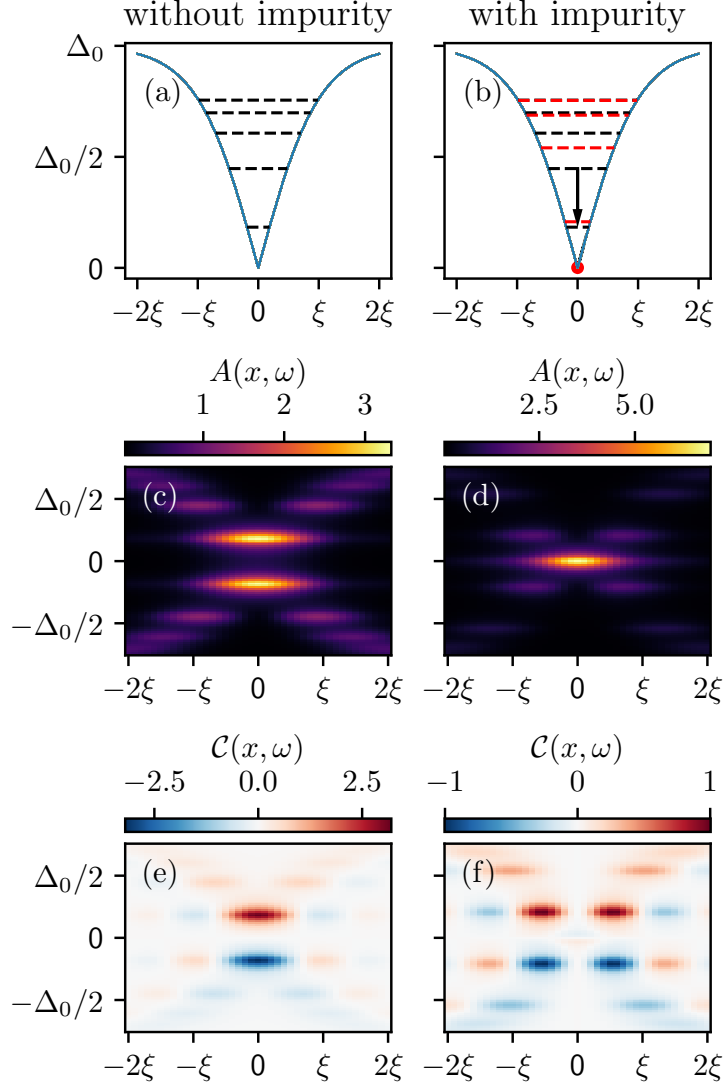


Figure 3.1: Energy states inside the vortex for (a) a clean s -wave superconductor and (b) an s -wave system with screened charge impurity. The blue line shows the position-dependent superconducting order parameter, and the dashed lines schematically show the energy of in-gap CdGM states. In panel (b), the black dashed lines indicate the CdGM spectrum without a charged impurity, whereas the red dashed lines indicate the spectrum with the impurity. The black arrow highlights the energy shift caused by the impurity potential. Panels (c) and (d) show the density of states, whereas (e) and (f) show the BCS spectral charge for the s -wave system without and with impurity respectively.

3.1 Model

We consider a trivial superconductor modeled as a two-dimensional electron gas with s -wave superconducting pairing ². The corresponding tight-binding model on a square lattice (with lattice constant a) has a normal state Hamiltonian

$$H_0 = (4t - \mu) \sum_i \sum_\sigma c_{i\sigma}^\dagger c_{i\sigma} - t \sum_{\langle i,j \rangle} \sum_\sigma c_{i\sigma}^\dagger c_{j\sigma} + \text{h.c.}, \quad (3.2)$$

where μ is the onsite energy, t is the hopping constant, $c_{i\sigma}^\dagger$ ($c_{i\sigma}$) creates (destroys) an electron of spin σ at site i , and $\langle i, j \rangle$ denotes a sum performed over nearest-neighbors. The superconducting term in the Hamiltonian is

$$H_{s\text{-wave}} = \sum_i \Delta_i^s c_{i\uparrow}^\dagger c_{i\downarrow}^\dagger + \text{h.c.},$$

$$\Delta_i^s = \Delta_0 e^{i\phi_i} \tanh\left(\frac{r_i}{\xi}\right), \quad (3.3)$$

where Δ_0 is the amplitude of the bulk order parameter, r_i is the distance from $\mathbf{r} = 0$ (the vortex center) to the atomic position i , ξ is the vortex radius, and $\phi_i = \arg(\mathbf{r}_i)$ is the order parameter phase, as shown in Figs. 3.2 (a) and (b). Note that we treat ξ and Δ_0 as independent parameters, since we do not solve the Ginzburg-Landau equations. We also treat spin as a trivial degeneracy and perform all tight-binding calculations with Kwant [96].

To match the typical ratios for μ/Δ_0 reported in experiments we set $\mu = 0.05t$ and $\Delta_0 = 0.02t$. We also set $\xi = 10a$, unless stated otherwise, to ensure that the vortex size is negligible compared to the system size ($200a \times 200a$).

²Refer to chapter 2 for a deeper review on this type of superconductivity.

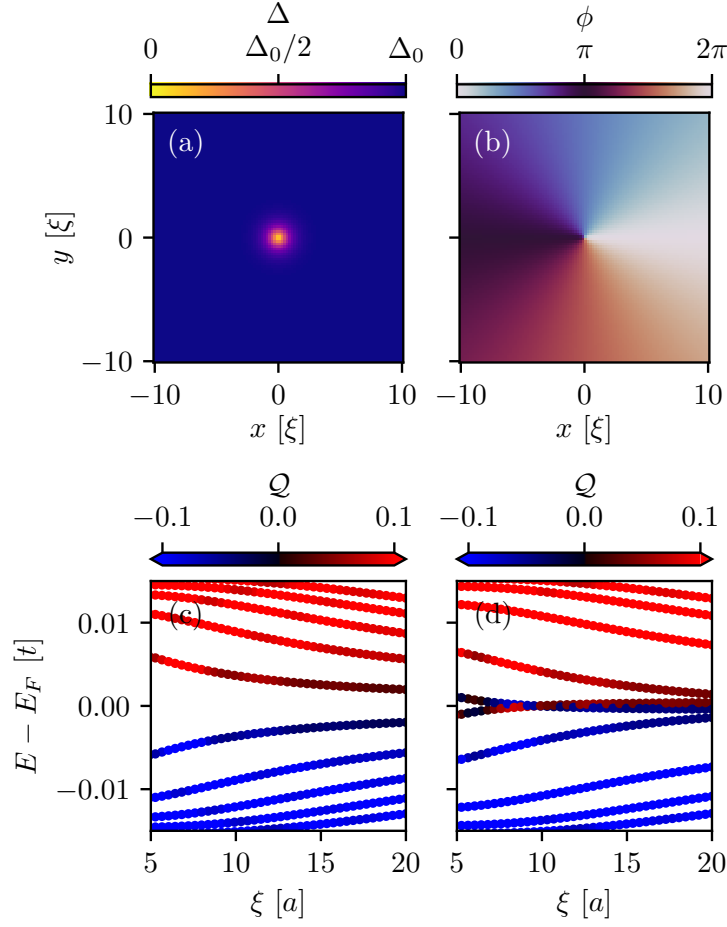


Figure 3.2: Magnitude (a) and phase (b) of the superconducting order parameter (as defined in Eq. (3.3)). The BCS charge-resolved spectrum of in-gap vortex states is shown for s -wave superconductor (c) without and (d) with an screened charge impurity with $\delta\mu = 0.06t$ and $\eta = 5a$.

Figure 3.2 (c) show the spectrum and the respective integrated BCS charge expectation values, $Q \equiv \sum_i Q(\mathbf{r}_i)$ where $Q(\mathbf{r}_i) := \langle \Psi | c_i^\dagger c_i - c_i c_i^\dagger | \Psi \rangle$ is the local charge for a given eigenstate, of in-gap vortex states for this system as a function of the vortex radius ξ . Finite energy levels approach zero as ξ increases, as expected for quantum-confined levels.

3.2 Effects of an impurity potential

We would like to test whether local changes in the electrostatic potential can shift the energy of CdGM states arbitrarily close to zero energy. In this situation, the lowest-energy trivial states may have energy smaller than the experimental resolution, resulting in a near-zero-bias conductance peak, similar to the one produced by MZMs.

To demonstrate this phenomenon, we consider the effects of an isolated screened charge impurity close to the vortex core. This choice is inspired by recent experiments in iron-based superconductors [88], [89], [92] showing that scalar impurities favor the presence of zero-bias peaks inside vortices.

We model the presence of a screened charged impurity on the s -wave Hamiltonian by incorporating an onsite modulation term as follows [97], [98]:

$$H_{\text{imp}} = \delta\mu \sum_{i,\sigma} e^{-r_i^2/2\eta^2} c_{i\sigma}^\dagger c_{i\sigma}, \quad (3.4)$$

where $\delta\mu$ is the potential strength of the impurity, and η is the screening length. Next, we calculate the energy spectra and the integrated charge Q of the quasiparticles.

Figure 3.3 shows the resulting low-energy spectra as a function of η and $\delta\mu$, revealing a resemblance to the spectra of a topological superconductor with a vortex. Both charge and energy of the lowest-energy state approach zero, while the shifts of energy and charges of higher energy states are exponentially suppressed³.

The local BCS charges $Q(\mathbf{r})$ for the lowest-energy in-vortex state with and without the impurity are shown in Fig. 3.3 (c). We verified that, although the total charge is suppressed [Fig. 3.3(a, b)], the local charge is weakly affected by the impurity. Thus, one should be able to distinguish CdGM and Majorana states with an arbitrarily small resolution, since MZMs have zero BCS charge everywhere. However, as we show in the next section, the energy shift together with level broadening of the lowest-energy CdGM states results in a vanishing spectral BCS charge.

³See Appendix E for a quantitative discussion on perturbative effects of impurities in higher energy states.

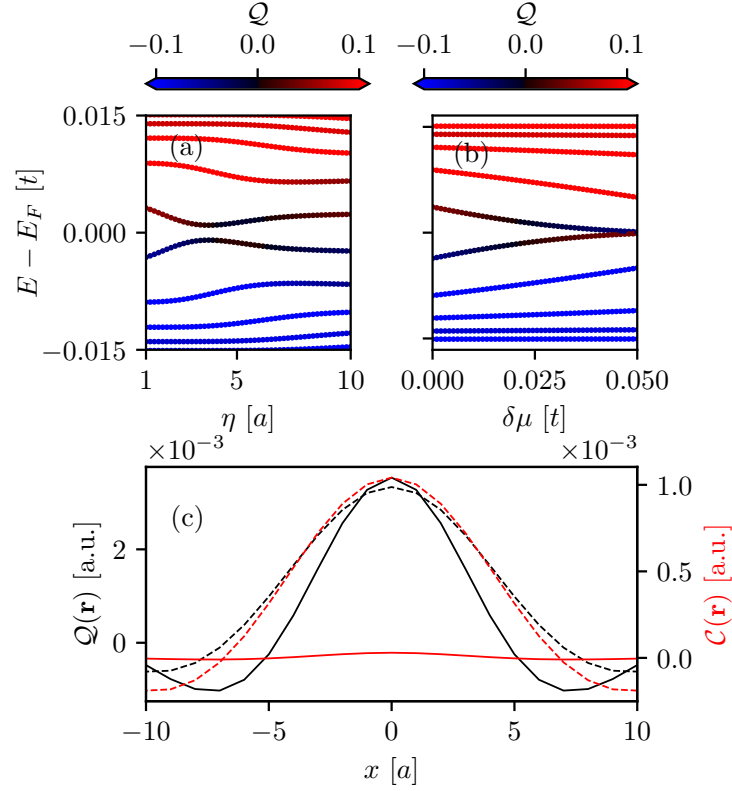


Figure 3.3: BCS charge for an s-wave system with impurity. In panels (a,b), the spectrum evolves as a function of (a) impurity size η ($\delta\mu = 0.025t$), (b) impurity strength $\delta\mu$ ($\eta = 5a$). (c) BCS charge (black) and BCS charge spectral density (red) for the lowest energy state for a system without (dashed line) and with (solid line) an impurity with $\eta = 5a$ and $\delta\mu = 0.05t$.

The effects of the vortex size and impurity screening length on the lowest-energy state, $E_{1/2}$, and its charge are shown in Fig. 3.4. The data clearly shows a suppression of $E_{1/2}$ and Q on large regions of the $\{\eta, \delta\mu\}$ parameter space, indicating that the above results hold beyond the highly-localized impurity regime, $\eta \ll \xi$. This also suggests that smooth fluctuations in the underlying electrostatic potential can mimic Majorana signatures. Furthermore, due to particle-hole symmetry, $E_{1/2}$ and Q tend to be correlated.

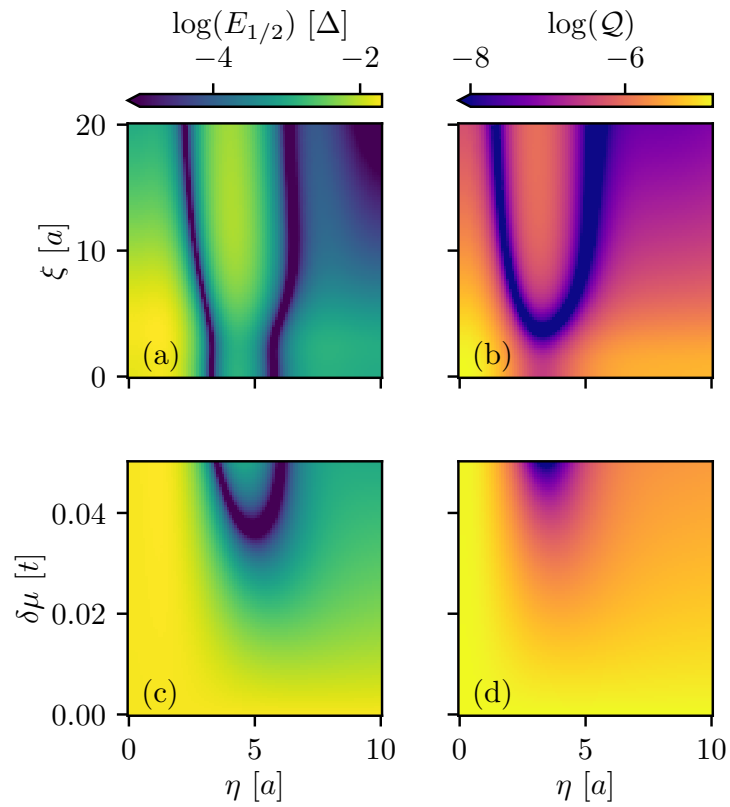


Figure 3.4: Dependence of lowest energy state $E_{1/2}$ (a, c) and BCS charge (b, d) on (a, b) η and ξ , (c, d) η and $\delta\mu$. In (a, b) we choose $\delta\mu = 0.06t$, and in (c, d) we choose $\xi = 5a$.

3.3 Experimental relevance

In this section, we highlight the relevance of our results for the interpretation of current experimental data from Scanning Tunneling Spectroscopy (STS) and Scanning Tunneling Microscopy (STM) experiments [7], [88], [92].

Thus far, we have discussed the changes in the global properties of CdGM state due to the presence of scalar impurities at the vortex site. Since vortices tend to be pinned by defects and impurities [99], this picture can be favored in samples in which some degree of surface disorder is present, as it seems to be the case in Fe(Se,Te) surfaces [92].

Moreover, STS conductance peaks at energies below of what would be estimated as $E_{1/2}$ are usually “ruled out” as CdGM states [7], [92]. As we have shown, such a heuristic picture is not accurate in the presence of impurities: the results shown in Figs. 3.2 and 3.3 show that the energy of the first CdGM state can be significantly lower than the value of $E_{1/2}$ estimated from bulk parameters and serve as a cautionary tale against ruling out these near-zero states as CdGM states.

Another important point of attention when comparing the raw CdGM spectra with the peaks appearing in STS measurements is the role of the thermal effects of the STS peaks, which effectively sets an energy resolution. To illustrate the limitations introduced by such energy resolution, we defined the spatially-resolved spectral density $A(\omega, \mathbf{r})$, and the spectral BCS charge $C(\omega, \mathbf{r})$ at energy ω and position \mathbf{r} :

$$G(\omega) = [\omega - H + i\gamma]^{-1}, \quad (3.5)$$

$$G(\omega, \mathbf{r}) \equiv \langle \mathbf{r} | G(\omega) | \mathbf{r} \rangle, \quad (3.6)$$

$$A(\omega, \mathbf{r}) \equiv -\frac{1}{\pi} \text{Im Tr} [G(\omega, \mathbf{r})], \quad (3.7)$$

$$C(\omega, \mathbf{r}) = -\frac{1}{\pi} \text{Im Tr} [G(\omega, \mathbf{r})Q(\mathbf{r})], \quad (3.8)$$

where γ is a positive small parameter that sets the level broadening.

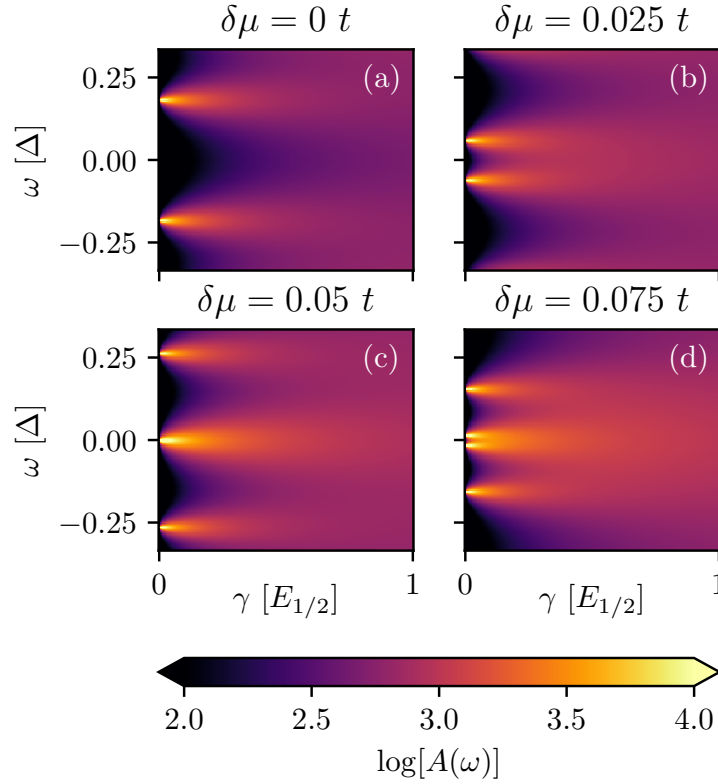


Figure 3.5: Density of states $A(\omega) \equiv (-1/\pi)\text{Im} G(\omega)$ of an s -wave superconductor as a function of level broadening γ ($\eta = 5a$). In panel (a), one can observe that the two trivial states are distinguishable in the absence of an impurity ($\delta\mu = 0$) up to $\gamma \sim E_{1/2}$. As the impurity strength increases, as shown in panels (b-d), the trivial states are shifted to smaller energies ω and therefore one cannot distinguish them even with a much smaller level broadening γ .

Typical experimental broadenings are of order $\gamma \sim 0.1 \Delta_0$ (mostly arising from thermal effects) whereas the energy spacing estimated without impurities is $E_{1/2} \sim 0.5\Delta_0$. [7] Thus, for clean systems, scanning tunneling transport experiments should indeed be able to resolve the energies of MZMs and CdGM states. However, electrostatic inhomogeneities that make $E_{1/2} \sim \gamma$ impede a clear distinction between trivial and non-trivial states due to the constraint imposed by particle-hole symmetry that implies the shifting of positive and negative energy states towards zero energy.

We illustrate the effects of level broadening in Figs. 3.1 and 3.5. Figure 3.1 shows contour plots of $A(\omega, \mathbf{r})$ [Fig. 3.1(c,d)] and $C(\omega, \mathbf{r})$ [Fig. 3.1(e,f)] for energies within the gap and positions inside the vortex. In the absence of impurities [Fig. 3.1(c) and (e)], one obtains peaks in $A(\omega \approx \pm E_{1/2}, \mathbf{r} \approx 0)$ originating from the first CdGM state, as expected. Some smaller peaks for excited CdGM states (with nodes at $\mathbf{r} \approx 0$) are also seen. The BCS charge for these states oscillates in position along the vortex, changing sign.

A different picture is observed in the presence of impurities and a modest thermal broadening ($\gamma/E_{1/2} \approx 0.27$). There is a single peak in the spectra charge density near zero energy $A(\omega \approx 0, \mathbf{r} \approx 0)$, and the BCS charge at these energies is very close to zero. In Fig. 3.5 we illustrate how much the level broadening affects our results. In the absence of impurities [Fig. 3.5(a)], the energies of CdGM states are determined by the bulk parameters. Therefore, the two lowest-energy peaks are distinguishable up to $\gamma/E_{1/2} \sim 1$. As the energy levels shift towards zero, the two lowest-energy peaks cannot be resolved for $\gamma/E_{1/2} \gtrsim 0.5$ (Fig. 3.5 (b)). In some cases, these peaks cannot be resolved even for relatively “small” broadening values $\gamma/E_{1/2} \sim 0.1$ or lower (Fig. 3.5 (c-d)). In a similar manner, since particle-hole symmetry ensures that $Q_{m=1}(\mathbf{r}) = -Q_{m=-1}(\mathbf{r})$, the BCS charge also becomes negligible, as shown in Fig. 3.1 (f).

Notice that the combined effect of the shifting of the energy levels toward zero and a moderate broadening can effectively “disguise” the lowest CdGM state as a zero-bias peak (see. e.g., Figs. 3.5 (c,d)) in experiments. Interestingly, some STS experimental data show vortex bound states as peaks *near but not at* zero bias in the tunneling spectra [88], a result which is consistent with this picture.

These observations suggest that recent experiments claiming impurity-assisted formation of MZMs [89] should be interpreted carefully. At the same time that local changes in the chemical potential could lead to a topological phase transition, trivial CdGM states can also be shifted arbitrarily close to zero energy. Thus, zero-bias peaks in the vicinity of scalar impurities are ambiguous signatures and cannot fully distinguish MZM and CdGM states.

3.4 Concluding Remarks

In this chapter, we have found that scalar impurities within vortices can alter the CdGM spectrum, resulting in spectral features that resemble those of MZMs. This is exemplified by using the unequivocally non-topological case of s-wave superconductivity. We see that scalar perturbations near the vortex center can decrease the energy of CdGM states and suppress their global BCS charge.

We highlight that this is a general result. Particularly, the energy and charge of CdGM modes can be shifted arbitrarily close to zero for a broad range of values in the parameter space of the model proposed, as shown in Fig. 3.4.

Consequently, distinguishing between impurity-driven zero energy states and topological MZMs using only local spectroscopic techniques may not be possible. Moreover, extrinsic broadening effects on particle-hole symmetric levels lead to apparent vanishing of the BCS charge. These considerations are particularly relevant to experimental works that often rely on the fact that CdGM states have finite energy.

To complement current local STS set-ups, non-local probes with adequate experimental resolution could potentially be used to map changes in the BCS charge at a local level, as argued in Ref. [41]. In summary, it is important to provide a description of the spectroscopic properties as they will be affected by the presence of electrostatic inhomogeneities.

Chapter 4

Multi-vortex configurations in semiconductor-superconductor hybrid systems

The common approach to obtain topologically non-trivial excitations involves using p -wave superconductivity, where the superconducting pairing is linearly proportional to the momentum. The naturally arising fermion parity anomaly allows for the creation of unpaired Majorana quasiparticles with anyonic statistics. However, this type of superconductivity is not common in materials [2]. Moreover, there is no consensus regarding the superconducting pairing nature of the leading candidate for this pairing, Strontium Ruthenate (Sr_2RuO_4) [30]–[32].

Naturally, a more common and less controversial type of superconductivity became a topic of interest. The s -wave superconductivity, found in Al and Nb, can be aided by other contributions to the Hamiltonian to generate effective topological superconductivity [100]. One of the earliest proposals, the Fu-Kane model, include combining s -wave pairing and topological insulators [40]. In this chapter, we focus on a following proposal, using s -wave, semiconductors with spin-orbit and a magnetic insulator [10].

4.1 The hybrid setup

To understand how an appropriate combination of terms may give rise to a system analogous to p -wave superconductivity, it is instructive to review relevant symmetries in condensed matter; section 2.3 contains a review of the topic. With symmetry considerations in mind, we can explore

how to construct a topologically non-trivial Hamiltonian from scratch. Here is the initial generic Hamiltonian, with a kinetic term, $\eta = 1/(2m)$, and chemical potential, μ :

$$H_0 = (-\eta\nabla^2 - \mu)\tau_z. \quad (4.1)$$

Here, $\tau_i, i = \{x, y, z, 0\}$ are equivalent to Pauli matrices in particle-hole space. The proportionality with τ_z accounts for the particle-hole symmetry of the system¹. We are dealing with differential operators in the Hamiltonian, as we intend to analyze real-space properties at this point of the thesis.

We wish to add *s*-wave superconductivity. Considering a vortex-like order parameter for the *s*-wave superconductivity:

$$\Delta(r) = \Delta_0 f(r) e^{i\theta} \tau_x, \quad (4.2)$$

where $f(r)$ is the radial function of the order parameter and θ encompasses the angular dependency. However, due to the spin degree of freedom, it is impossible to generate unpaired Majoranas [2].

If allied with a magnetic insulator in the z direction to provide a Zeeman component to the Hamiltonian, we may break time-reversal symmetry:

$$H_{Zeeman} = V_z \sigma_z. \quad (4.3)$$

V_z is the strength of the Zeeman component. This is needed due to Kramer's degeneracy. Kramer's theorem states that, for spin-half systems, each energy eigenstate has a degenerate, time-reversed pair [24].

However, we now have a conservation law for the z component of spin. The system is trivial again because the bands crossing belongs to different spin species and thus are not coupled. Adding the spin-orbit coupling term, $H_{s.o.}$, is crucial to providing spin terms in x and y directions, thus breaking σ_z symmetry.

$$H_{s.o.} = \frac{\alpha}{2} (\sigma_+ p_- - \sigma_- p_+) \tau_z. \quad (4.4)$$

This is a Rashba-type spin-orbit term with strength α . In practice, that can be achieved by introducing a semiconductor with spin-orbit, such as InAs and InSb [4]. The final setup can be

¹Refer to subsection 2.1.4 for a review on Bogoliubov-de Gennes formalism.

visualized in Fig. 4.1.

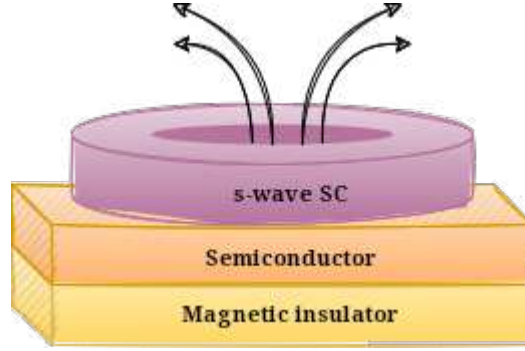


Figure 4.1: Physical setup for the hybrid device studied.

The final model, in the Nambu basis, becomes:

$$H = (-\eta\nabla^2 - \mu)\tau_z + V_z\sigma_z + \frac{\alpha}{2}(\sigma_+p_- - \sigma_-p_+)\tau_z + \Delta_0f(r)e^{i\theta}\tau_x. \quad (4.5)$$

Note that our final Hamiltonian breaks time-reversal symmetry and preserves particle-hole symmetry, fitting in the symmetry class D, as shown in the table 2.3. In this setting, a point-like defect (as a vortex) can host gapless states and possess \mathbb{Z}_2 protection, in analogy with a chiral p -wave system [101]. Due to the particle-hole symmetry of the system, it is convenient to write the Hamiltonian in Bogoliubov-de Gennes (BdG) form:

$$H_{\text{BdG}} = \begin{pmatrix} H_0 & \Delta \\ \Delta^* & -\sigma_y H_0 \sigma_y \end{pmatrix}, \quad (4.6)$$

with $H_0 \equiv (-\eta\nabla^2 - \mu)\tau_z + V_z\sigma_z + \frac{\alpha}{2}(\sigma_+p_- - \sigma_-p_+)\tau_z$. For this case of a single vortex, the angular dependency for this case can be avoided by performing a rotation of $e^{i(\sigma_x/2 - i\tau_x/2)\theta}$ [9]. This can also be achieved with a gauge transformation of the fermion operators as $c_\sigma \rightarrow c_\sigma e^{-i\theta/2}$, which omits the angular factor in the order parameter, since $\Delta(r) = \langle c_\downarrow c_\uparrow \rangle$.

The Hamiltonian for the electron sector is the 2x2 matrix:

$$H_{\text{BdG}} = \begin{pmatrix} -\eta(\partial_r^2 + \frac{1}{r}\partial_r) + V_z - \mu & +\alpha(\partial_r + \frac{1}{r}) + \lambda\Delta(r) \\ -\alpha\partial_r - \lambda\Delta(r) & -\eta(\partial_r^2 + \frac{1}{r}\partial_r - \frac{1}{r^2}) - V_z - \mu \end{pmatrix}. \quad (4.7)$$

We write the corresponding reduced spinor for the electronic part as:

$$\Psi(r) = \begin{pmatrix} u_{\uparrow}(r) \\ u_{\downarrow}(r) \end{pmatrix} \quad (4.8)$$

As the Majorana particles are the zero-energy quasiparticles for this Hamiltonian, we are interested in solutions for $H_{\text{BdG}}\Psi(r) = 0$. We obtain the coupled equations:

$$-\partial_r^2 u_{\uparrow}(r) - \frac{1}{r} \partial_r u_{\uparrow}(r) + u_{\uparrow}(r) + \partial_r u_{\downarrow}(r) + \frac{u_{\downarrow}(r)}{r} - \Delta(r) u_{\downarrow}(r) = 0, \quad (4.9)$$

$$-\partial_r u_{\uparrow}(r) + \Delta(r) u_{\uparrow}(r) - \partial_r^2 u_{\downarrow}(r) - \frac{1}{r} \partial_r u_{\downarrow}(r) + \frac{u_{\downarrow}(r)}{r^2} - u_{\downarrow}(r) = 0, \quad (4.10)$$

where we considered the parameters provided in reference [10], $\eta = \alpha = V_z = -\lambda = 1$, $\Delta_0 = 0.1$ and $\mu = 0$. Now we can solve the differential equations from the Hamiltonian through Boundary Value Problem (BVP) technique.

In Fig. 4.2, we plot the spinor components of the reduced BdG Hamiltonian of this system, which we will denote as $u_{\uparrow}(r)$ and $u_{\downarrow}(r)$.

Note the results are quantitatively different from Fig. 2 of the original reference for the hybrid model [10]. While our results indicate $u_{\downarrow}(r)$ with negative initial first derivative, the results showcase a negative initial first derivative.

Upon further review and after discussion with the original paper authors, both parts concluded that our results in Fig. 4.2 are nevertheless correct. This is partially due sign-error typo in the caption of Fig 2 in [10]. The correct initial condition is $\Psi_0(r = 0) = -(1, 0)^T$. Furthermore, sign of the first derivative was incorrect. Our results also consistent with Fig 3 of a later paper from the same authors, apart from the sign of the initial conditions [9].

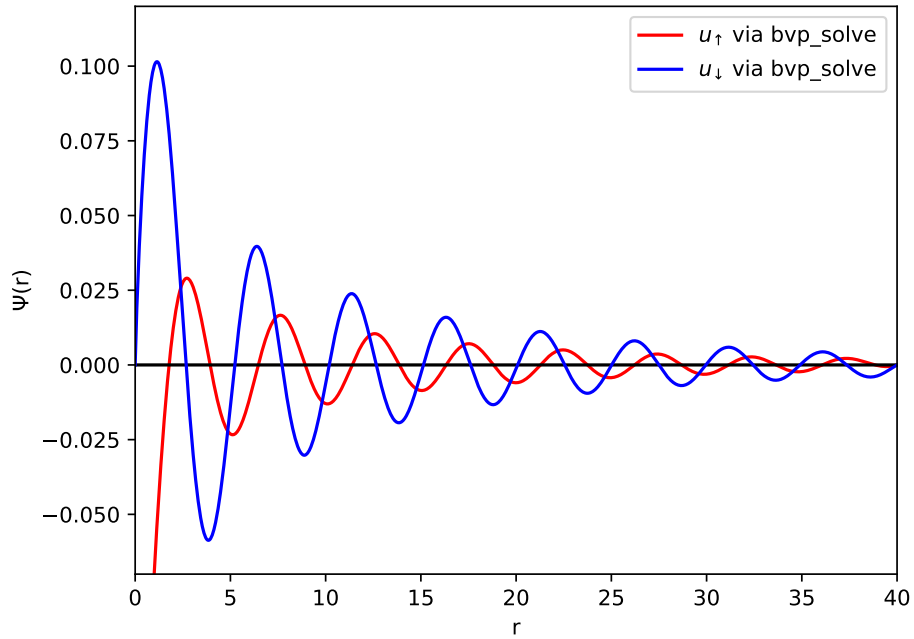


Figure 4.2: Spinor components from the reduced BdG Hamiltonian with a vortex-like order parameter. where we used $\eta = \alpha = V_z = -\lambda = 1$, $\Delta_0 = 0.1$ and $\mu = 0$.

4.2 Zero-energy spinor components for many vortices

Using the setup discussed in the last section, we can now extrapolate the results from the literature to obtain a more general expression, considering more vortices. For this purpose, we need to modify the order parameter to correspond to multiple different positions for the new vortices, R_i . A general way to account for this behavior would take the following form [102]:

$$\Delta(r, R_i, \theta, \theta_i) = \prod_{i=1} f(|r - R_i|) \exp[i\phi_i(r, R_i, \theta, \theta_i)]. \quad (4.11)$$

Where the i index counts the number of vortices. The term $f(r - R_i)$ is the radial component of the order parameter, that can be obtained self-consistently.

The component $\phi_i(r, \theta)$ accounts for the angle between the vortex positions and n_i are the winding numbers of the vortices. This form maintains the parity of the order parameter as even, thus, it is still compatible with s -wave pairing. This is important to preserve the required overall antisymmetry of the fermionic wavefunction.

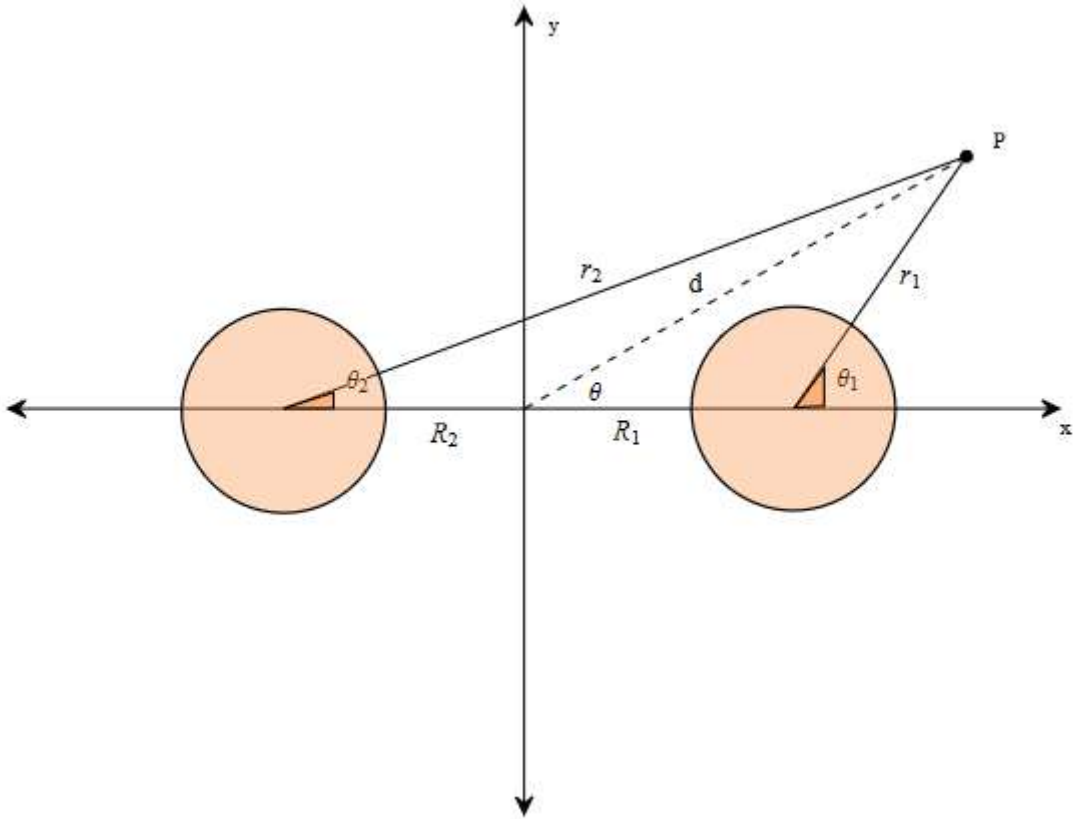


Figure 4.3: A visual scheme for two vortices in real space. The distance between vortices is assumed to be greater than the vortex core, $R_{core} = 1$.

In polar coordinates, we can write the coordinates of the vortices in a given distance d of the reference point P in terms of the coordinates of our origin as:

$$R_i(r, \theta) = \sqrt{r_i^2 + d^2 + 2r_i d \cos \theta}, \quad (4.12)$$

$$\theta_i(r, R_i, \theta) = n_i \arctan\left(\frac{\sin \theta}{\cos \theta - d/R_i}\right), \quad (4.13)$$

where r_i is the distance between vortex i and P . We introduce $n_i = \pm 1$ to account for different winding numbers. Thus, our final form for the order parameter is:

$$\Delta(r, R_i, \theta, \theta_i) = \Pi^N \Delta_0 f(r - R_i) e^{i(\theta - n_i \theta_i)}. \quad (4.14)$$

A sketch for the real space interaction between two vortices is shown in Fig. 4.3.

Our coupled system for more than one vortex cannot be solved by separation of variables anymore due to the modified order parameter, which is no longer rotationally invariant. Explicitly, the new set of BdG equations are:

$$-\partial_r^2 u_\uparrow - \frac{1}{r} \partial_r u_\uparrow - \frac{1}{r^2} \partial_\theta^2 u_\uparrow + u_\uparrow + \frac{ie^{-i\theta}}{2} \left(-i\partial_r u_\downarrow - \frac{1}{r} \partial_\theta u_\downarrow \right) - \Delta(r, \theta) u_\downarrow = 0 \quad (4.15)$$

$$-\frac{ie^{i\theta}}{2} \left(-i\partial_r u_\uparrow + \frac{1}{r} \partial_\theta u_\uparrow \right) + \Delta^*(r, \theta) u_\uparrow - \partial_r^2 u_\downarrow - \frac{1}{r} \partial_r u_\downarrow - \frac{1}{r^2} \partial_\theta^2 u_\downarrow - u_\downarrow = 0. \quad (4.16)$$

To solve this coupled system, we use the Finite Differences method, further explained in Appendix F [103]. Once cast in a discretized form, we use a routine to invert sparse matrices and obtain the N -vortices spinor components. As a sanity check, we may test whether our generalization can be reduced to the one-vortex case reproduces the result for one vortex. Fig. 4.4 demonstrates that this is the case ².

²Refer to Appendix F for details and comparison between Boundary Value Problem and Finite Differences methods.

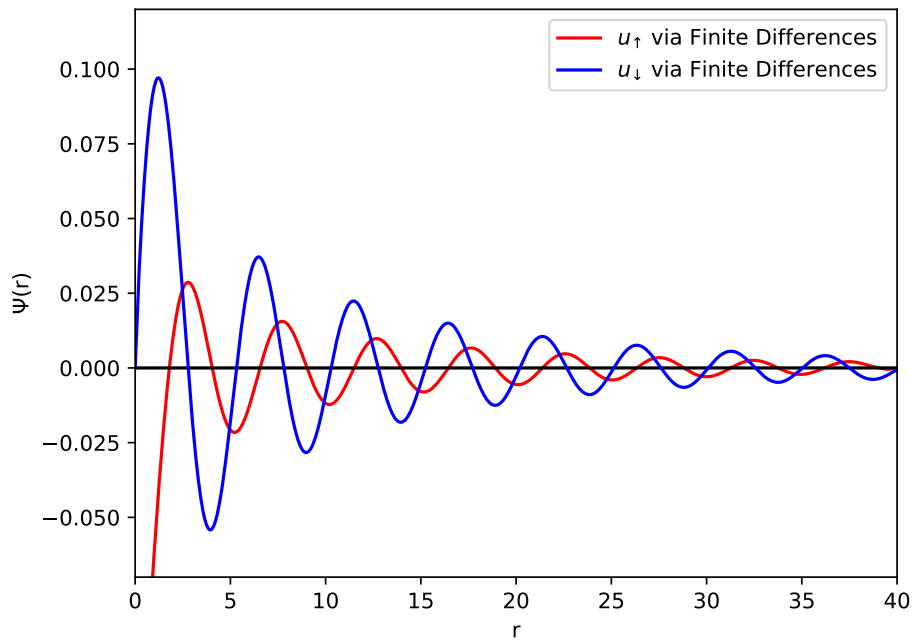


Figure 4.4: Spinor component solutions. Using parameters to account for one vortex.

4.3 Topological Characterization for many vortices

In order to understand and quantify the topological nature of the generalized proposal, starting with the original semi-superconductor Hamiltonian, we can introduce our modeled order parameter, tweak parameters and analyze relevant observables.

In this section, we check the proximitized s -wave, semiconductor and magnetic insulator setup and compare with the standard p -wave setup in the previous section. Note that the system will be topological when $V_z > V_z^c$, or $V_z > \sqrt{\mu^2 + \Delta_0^2}$ [9]. The parameters used from here onwards are, unless stated otherwise, $\Delta=5$, $\mu=0$, $V_z=10$ and $\eta=2$.

4.3.1 Majorana Polarization

For precision, we use a scattering space of 100-by-100 sites system. We may plot the density of states to observe spatial signatures case ³. For a more quantitative test, we can use **Majorana Polarization**, a measure of the particle-hole symmetry of the system, useful to analyze whether the vortices have a topological character [104], [105]. A generalized formulation of the Majorana Polarization is:

$$MP = \frac{\sum \langle \Psi | C_j | \Psi \rangle}{\sum \langle \Psi | r_j | \Psi \rangle}, \quad (4.17)$$

where C_j is the particle-hole operator and r_j is the projection onto a site j . Majorana states obey $\langle \Psi | C_j | \Psi \rangle = 1$, thus the expression, when evaluated over a region, determines the localization of the Majorana state, with $MP \rightarrow 1$ representing a localized state in a given region. For the system we are considering, $C_j = \sigma_x$.

Fig. 4.5 presents a spectrum with clear zero-energy mode and high Majorana Polarization. It also features two gap openings: for small V_z , the gap is open because $V_z < \sqrt{\mu^2 + \Delta_0^2}$. A second gap opening is also expected for higher magnetic fields.

³We are using the `kwant.plotter.map()` method in Kwant, as opposed to the usual `kwant.plotter.density()` for improved site-level resolution.

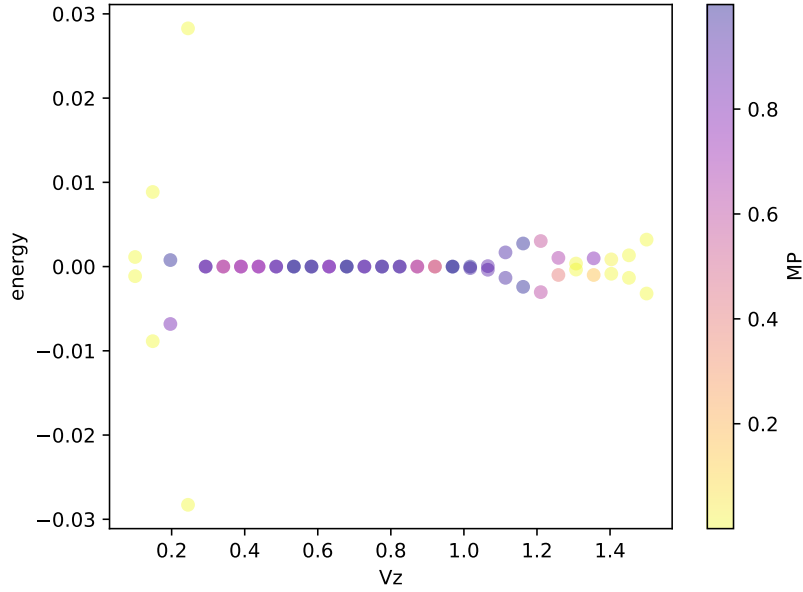


Figure 4.5: Single vortex case: Spectrum. Here, $\Delta = 0.5$.

Majorana polarization may be represented as a vector field, with the x component of each arrow corresponding to $\text{Re}(\langle \Psi | C_j | \Psi \rangle)$ and the y component being $\text{Im}(\langle \Psi | C_j | \Psi \rangle)$, as it brings to light how components may cancel each other over a given region [106].

4.3.2 Multiple Vortices

We are interested in investigating the possibilities of working with several vortices. For this purpose, we move to two vortices, as pictured in Fig. 4.6. We start by placing two vortices at $r_1 = (10, 0)$ and $r_2 = (-10, 0)$, in units of the lattice length. In realistic systems, vortices too close to each other may fuse into a single trivial Fermion, however, vortices too far away may be affected by the proximity of the edges. In the present computational simulations, the vortices' radii is taken to be effectively zero; the more complex case of finite radius will be taken into account in Chapter 3. Therefore, fusion by proximity is minimized.

Fig. 4.6 a showcases a well-localized density of states and Fig. 4.6 b, the vectorial Majorana Polarization. Higher values of the order parameter will increase radial symmetry in this representation, which may lead to canceling components on a given region.

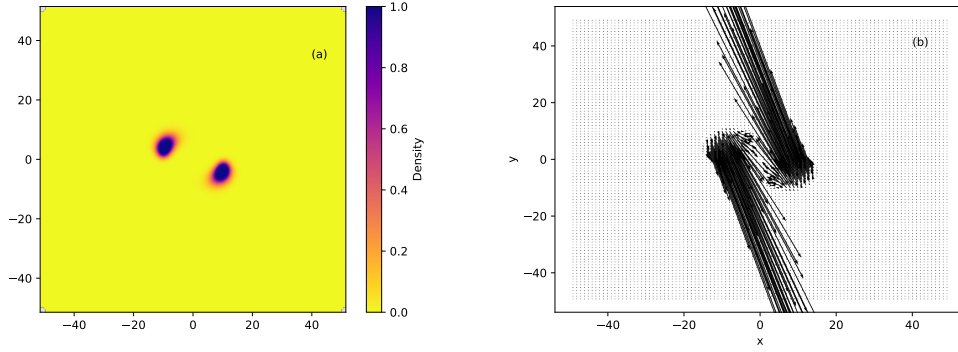


Figure 4.6: Two vortices case: a) spatial distribution of the density of states, b) spatial distribution of the Majorana Polarization.

In Fig. 4.7, the spectrum for two vortices as a function of the external magnetic field reveals a robust zero-energy mode, with high Majorana Polarization, up until the gap opening at $\Delta = 5$. For $\Delta \leq 5$, the spectrum shows many near-zero energy states. Note the absence of the first gap opening.

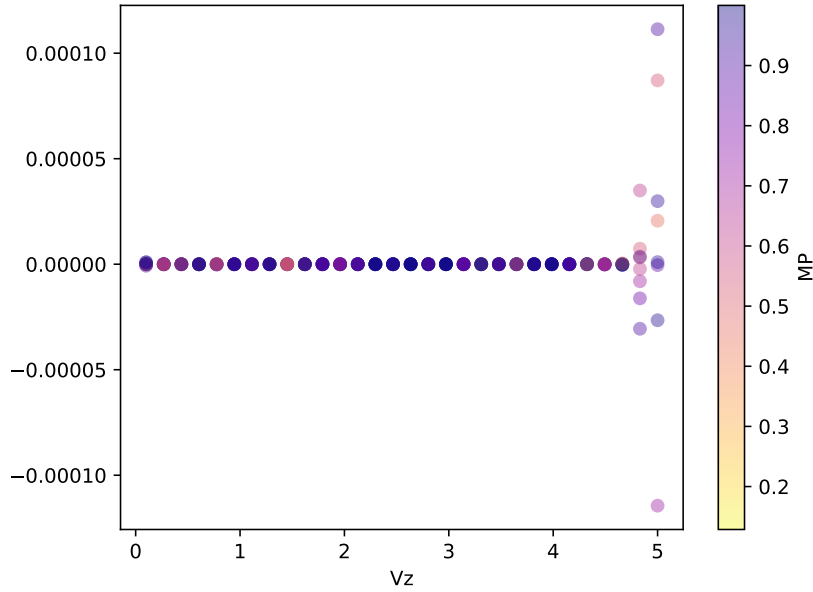


Figure 4.7: Two vortices case positioned at $r_1 = (30,0)$ and $r_2 = (-30,0)$: Spectrum as a function of V_z .

With more than a single vortex, we can also investigate the effect of different relative phases between vortices. As described previously in Eq. (4.13), for many vortices we have:

$$\Delta = \Delta_0 \prod_n \exp\{in \arctan(y_n, x_n)\} \quad (4.18)$$

where n is the n -th vortex added and y_n, x_n are the respective x - and y -coordinates for the vortex n . The phase $n = \pm 1$ represents the relative phase of the vortices. We may establish the convention (n_1, \dots, n_N) to indicate the phases of the first to the N -th vortex, respectively.

In Fig. 4.8, the vortex at $r_2=(10,0)$ possess a negative phase factor. Differences in Majorana Polarization as a function of V_z are minimal when compared to Fig. 4.7, where the vortex at $r_2=(-10,0)$ carries a positive phase factor.

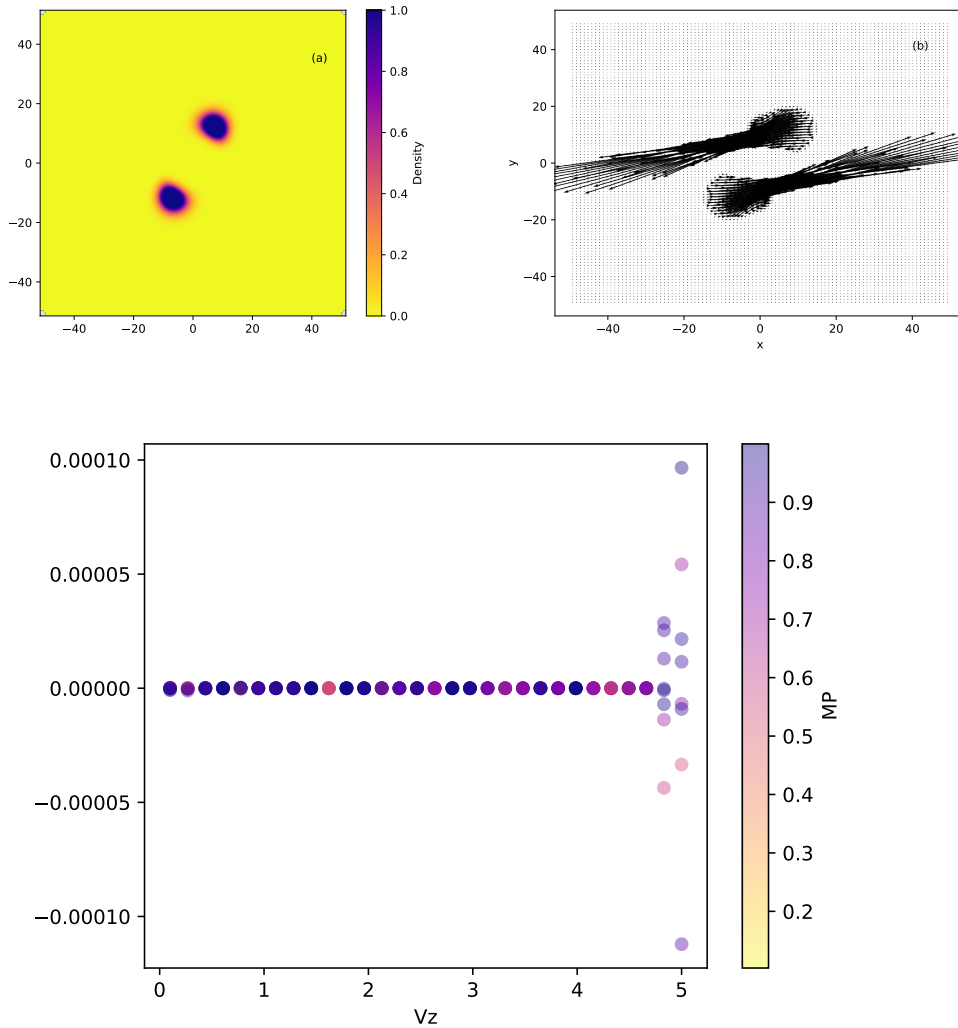


Figure 4.8: Two vortices case, with $(-1,1)$ phases, positioned at $r_1 = (10,0)$ and $r_2 = (-10,0)$: a) spatial distribution of the density of states, b) spatial distribution of the Majorana Polarization.

Four vortices

We now investigate four vortices, as this is the required number of vortices to define a single qubit. We place the vortices at $r_1 = (20,0)$, $r_2 = (-20,0)$, $r_3 = (0, 20)$ and $r_4 = (0,-20)$. It is straightforward to note the detrimental aspect of relative phases here by comparing right and left

sides of Fig. 4.9.

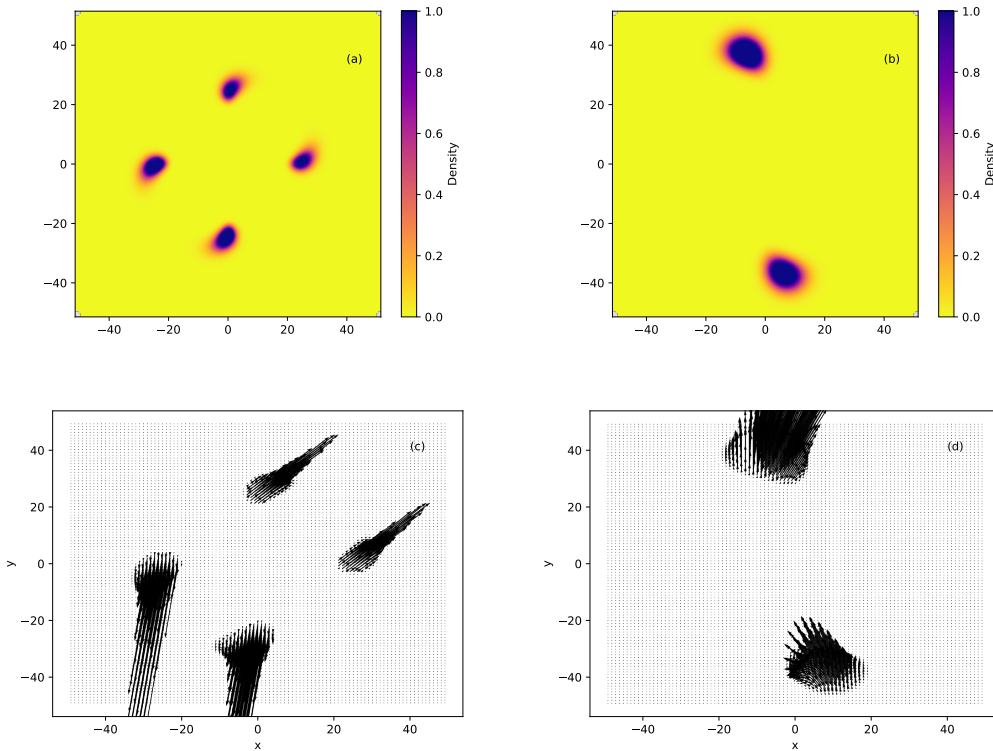


Figure 4.9: Four vortices. a) spatial distribution of the density of states for for $(+1, -1, +1, -1)$ phases. b) spatial distribution of the density of states for for $(-1, +1, +1, -1)$ phases. c) spatial distribution of the Majorana Polarization for $(+1, -1, +1, -1)$ phases. d) spatial distribution of the Majorana Polarization for $(-1, +1, +1, -1)$ phases.

Different relative phase also impact the spectrum, as shown in Fig. 4.10. Similarly to the two-vortex case, there intervals of Zeeman magnitude where clear zero-energy mode can be found. However, in other intervals, the spectrum is crowded with very near zero-energy spurious states that can pose a problem for experimental identification. Moreover, the energy scales for the levels are critically different for different relative phases.

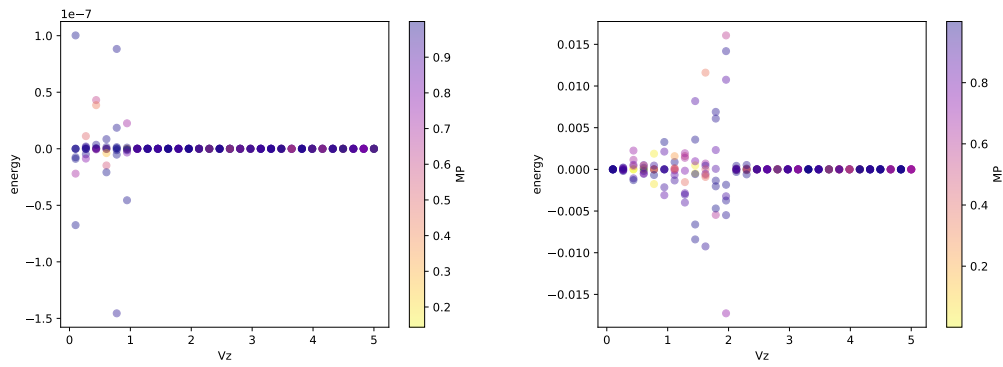


Figure 4.10: Four vortices case positioned at $r_1 = (20,0)$, $r_2 = (-20,0)$, $r_3 = (0, 20)$ and $r_4 = (0,-20)$. a) spectrum as a function of V_z for $(+1,-1,+1,-1)$ phases. b) spectrum as a function of V_z for $(-1,+1,+1,-1)$ phases.

Note, also, the impact of the scattering region in Fig. 4.11, where 200x200 sites are used instead of 100x100 sites. As expected, it is possible to obtain a much cleaner spectrum because hybridization among vortices and edge effects should be minimized.

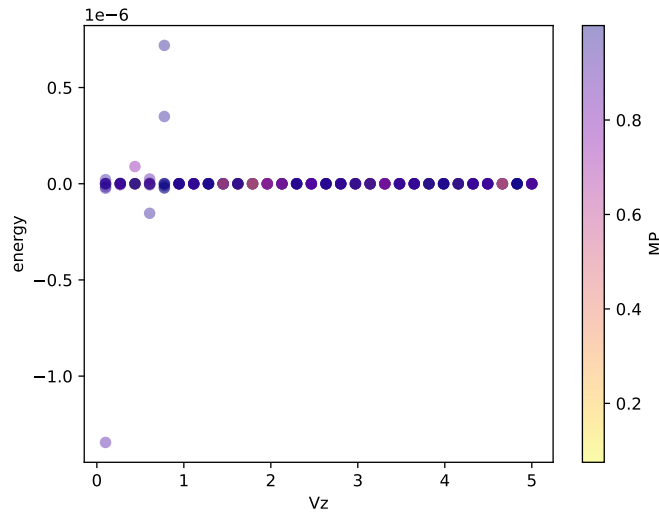


Figure 4.11: Four vortices case positioned at $r_1 = (20,0)$, $r_2 = (-20,0)$, $r_3 = (0, 20)$ and $r_4 = (0,-20)$: spectrum as a function of V_z on a 200x200 sites scattering setup.

4.4 Concluding remarks

We investigate whether the ability to retain topological character would be more robust in a the hybrid system, as opposed to traditional p -wave system that we considered in the last section.

The first difference comes from the inherently different nature of the boundary conditions for these types of superconductivity. While the complex phase of the p -wave order parameter imposes restrictions to the number of vortices added, the scalar s -wave order parameter do not hold the same constraint. This is relevant because although the total number of modes are the same, the edge mode will not be useful for braiding.

However, a direct comparison between the two flavors of superconductivity in real space is severely limited by numerical factors. The computational method for finding the wavefunction components require sparse diagonalization, which tends to be costly, specially for complex matrices [107]. Increasing scattering space region is ideal for resolution, but increases memory consumption. This restriction makes it difficult to avoid hybridization among vortices and edge effects, even in the approximation of minimal radii.

Particularly for spectrum analysis, it is difficult to select the appropriate lowest energy state. This is most likely the explanation to why the first gap opening is generally absent for more than a single vortex: proper selection of the appropriate states is not a trivial matter, and many in-gap trivial Andreev states may be accidentally taken into account. It is interesting, however, to note that it is possible to find sets of parameters with high Majorana polarization.

Chapter 5

Conclusions

The search for Majorana quasiparticles has been driven by the growing interest in both quantum computing and topological materials. While much of the experimental efforts have focused on nanowire realizations, the limitations and skepticism surrounding this approach have prompted investigations into two-dimensional setups such as superconducting vortices. The present thesis has explored the potential and limitations of these vortices as hosts for topological quasiparticles.

In the second chapter of our work, we delve into the issue of false-positive signatures of Majoranas in the presence of scalar impurities in fully trivial superconductivity. We investigate both energy and charge measurements and show that high apparatus resolution alone is not sufficient to resolve the signature ambiguity. In fact, the expected level broadening can hinder the unequivocal differentiation between Majorana states and topological trivial states that may coexist in vortices.

Moving on to the third chapter, we explore the use of proximitized superconductivity, where we employ trivial s -wave and additional external parameters to mimic intrinsic topological superconductivity in vortices. We use computational simulation to examine the advantages and disadvantages of this approach.

Our work has interesting implications for experimental studies on Majorana physics in vortices. One of our main findings is the formal confirmation that considering the experimental energy resolution higher than the lowest CdGM mode as a sufficient criteria for differentiation of trivial and non-trivial states is a misconception. We have shown that this energy scale is, in fact, nothing more than an upper bound when scalar impurities are present.

Additionally, our work highlights the benefits of combining different contemporary ap-

proaches, such as the recent exploration of non-local BCS charge measurements, when aiming for convincing evidence of presence or absence of Majorana quasiparticles.

However, we also note the instrumental limitations posed by memory-consuming calculations and the current lack of direct accessibility of Majorana polarization through experiments. Further research and technological advancements will surely be needed to fully realize the potential of Majorana quasiparticles and their applications in quantum computing and beyond.

Appendix A

Braiding and Fusion formalisms

In three dimensions, the permutation operation, P , applied on wavefunctions of indistinguishable particles in positions r_1 and r_2 is given by

$$P\Phi(r_1, r_2) = a\Phi(r_2, r_1), \quad (\text{A.1})$$

with $a = \pm 1$. When $a = 1$, the wavefunction represents Bosons; when $a = -1$, Fermions. In two dimensions, however, the permutation may take a more general form:

$$P\Phi(r_1, r_2) = e^{i\theta}\Phi(r_2, r_1), \quad (\text{A.2})$$

where $e^{i\theta}$ is not necessarily ± 1 . This is a consequence of the dimensionality restriction forcing that permutation trajectories characterized by different winding numbers cannot be continuously deformed into one another [108]. This peculiarity of two-dimensions calls for a more general description than the permutation operation. The braid group for n particles is defined as:

$$\sigma_j \sigma_k = \sigma_k \sigma_j \quad (\text{A.3})$$

when $|j - k| \geq 2$, and

$$\sigma_j \sigma_{j+1} \sigma_j = \sigma_{j+1} \sigma_j \sigma_{j+1} . \quad (\text{A.4})$$

The operation σ_i represents the counter-clockwise permutation of adjacent particles [109]. Visualizations of these properties are portrayed in Figures A.1 and A.2.

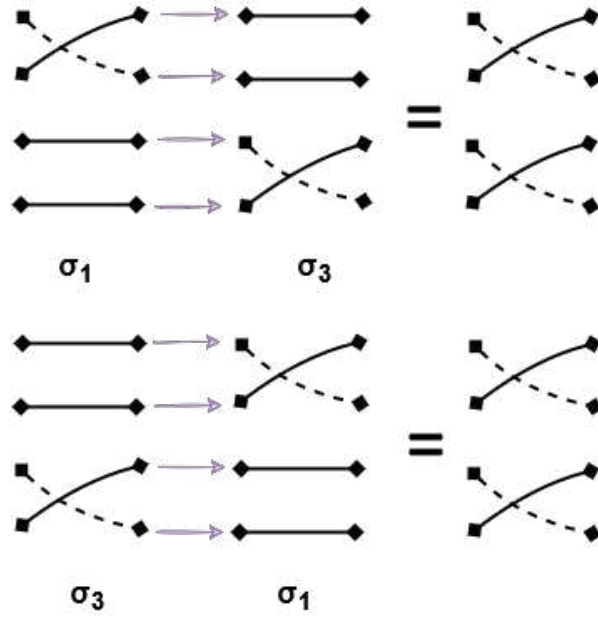


Figure A.1: Pictorial demonstration of first braiding relation. Braiding diagrams can be composed by concatenation of the end of an operation with the beginning of another for each particle, as shown by the purple arrows. The dashed lines represent that the trajectory is below the full line.

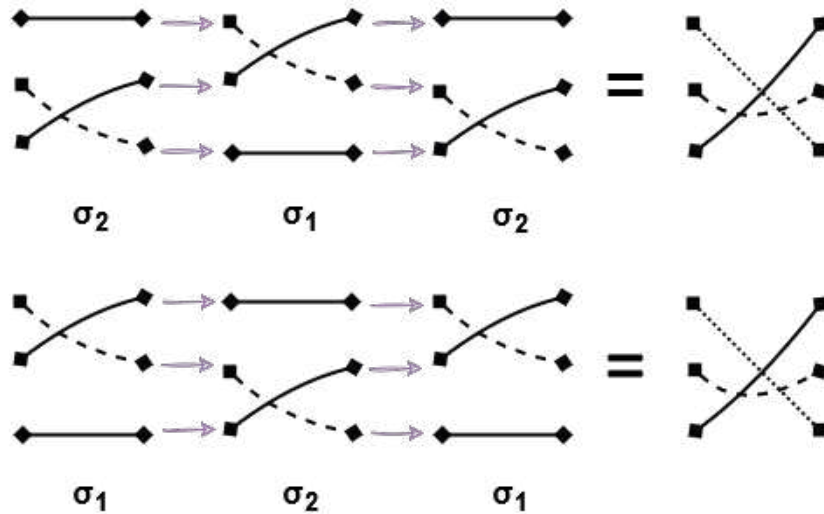


Figure A.2: Pictorial demonstration of second braiding relation. Braiding diagrams can be composed by concatenation of the end of an operation with the beginning of another for each particle, as shown by the purple arrows. The dashed lines represent that the trajectory is below the full line. Smaller, lesser-spaced dashed lines are below both the larger dashed line and the full line.

The braiding of non abelian anyons can create several single qubit gates, as detailed in the main text.

Fusion rules - Although braiding realizes quantum gates, the readout of the outcome of a quantum circuit relies on obtaining the final topological charges [29], [109].

The physical process of fusion brings together two particles that will output another particle. This may happen univocally, as is the case for abelian anyons, or it may happen through multiple fusion channels, allowing for different particles.

In general, for two particles a and b , their fusion is expressed as:

$$a \times b = \sum_i N_{ab}^i i, \quad (\text{A.5})$$

where i are the possible particles obtained from this fusion process.

The relationship of different fusion ordering of operations is given by the F-matrix components, also known as an F-move. For instance, the process $a \times b = i$ followed by $c \times i = d$ is related to the process $b \times c = j$ followed by $a \times j = d$ via:

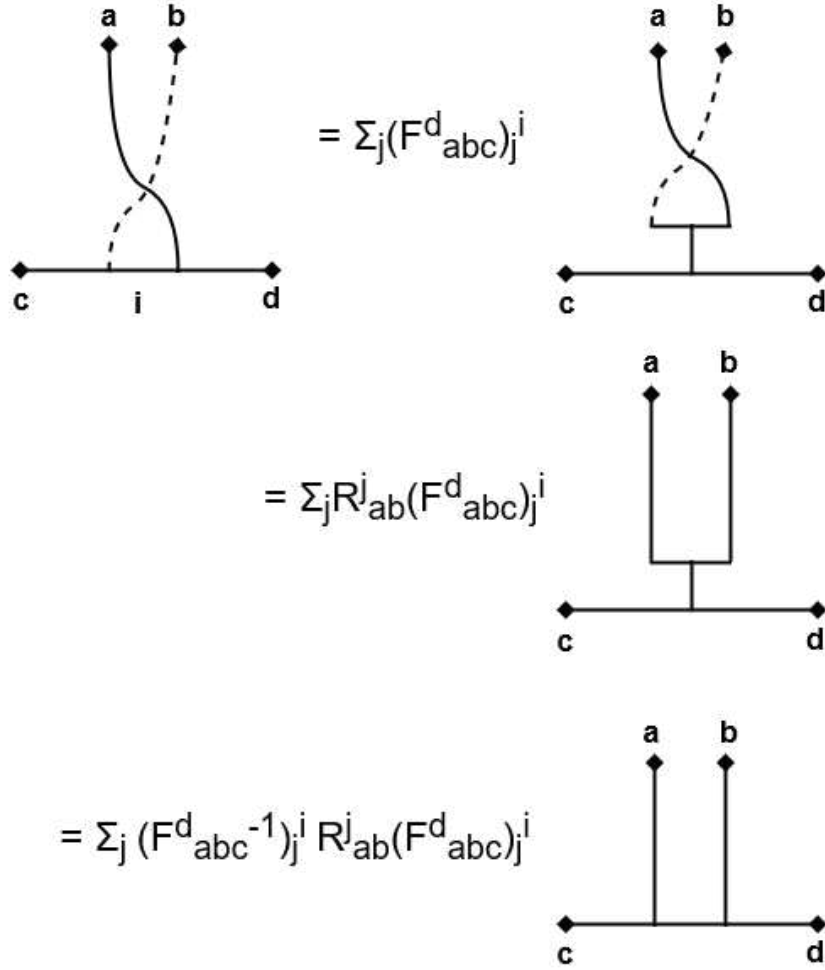
$$|i\rangle = \sum_j (F_{abc}^d)_j^i |j\rangle, \quad (\text{A.6})$$

Another important operation is the R-move, corresponding to the clockwise exchange of two anyons with a well defined fusion channel.

The Braiding unitary, B , relates to F- and R-moves via:

$$B = F^{-1}RF. \quad (\text{A.7})$$

Figure A.3 is a diagrammatic visualization of the above identity. From it, we may understand braiding as an F-move changing an i particle output to a j particle output followed by an R-move on a and b particles and another F-move, changing j to i particle again.


 Figure A.3: Pictorial demonstration of $B = F^{-1}RF$.

Anyons in Majorana systems are of Ising type, in contrast to anyons the Fractional Quantum Hall Effect, of Fibonacci type. For our purposes, we are interested in the Ising fusion rules, which are:

$$\sigma \times \sigma = 1 + \psi, \quad (\text{A.8})$$

$$\sigma \times \psi = \sigma, \quad (\text{A.9})$$

$$\psi + \psi = 1. \quad (\text{A.10})$$

where σ are the non-abelian anyons. ψ are the Fermions and 1 is the vacuum [23], [109]. Therefore, fusion of anyons may produce a normal Fermion. As an example of this fusion, proximitized Majoranas hybridize and lose topological character, behaving as Fermions.

An interesting application of fusion relates to measurement-based braiding, as mentioned in subsection 2.7.1 in the main text. Equation 13 from reference [39] relates forced measurements

with braiding, using the formalism of fusion rules.

$$\hat{\Pi}_{M_3}^{(23 \rightarrow 14)} \hat{\Pi}_{M_2}^{(24 \rightarrow 12)} \hat{\Pi}_{M_1}^{(12 \rightarrow 23)} = \frac{e^{i\phi_M}}{d_a} \begin{array}{c} \begin{array}{ccc} a \bar{a} & & a a \\ \swarrow & & \searrow \\ & \nearrow & \\ a \bar{a} & & a a \end{array} \\ \propto R_{aa}^{(14)} \otimes |\bar{a}, a; 0\rangle \langle \bar{a}, a; 0|, \end{array}$$

where $R_{aa}^{(14)}$ represents the R-move of anyons 1 and 4 with topological charge a .

Appendix B

Circuit Model of Quantum Computation

Quantum computers are currently a topic of increasing interest due to their predicted optimized capabilities, compared to their classical counterparts, to perform specific computational tasks [110]. For instance, it may be useful to perform complex numerical studies such as the simulation of large interacting systems, molecular dynamics and protein folding, an unprecedented development in chemistry and pharmaceutical research. On the other hand, it also raises security concerns, as it may break Rivest-Shamir-Adleman (RSA) encryption, the most popular available security protocol [111].

Among the main challenges for implementing a reliable quantum computer, the stability of the quantum bits (qubits) is one of the most difficult, as they might lose quantum coherence due to environmental noise. An approach to overcome decoherence is to work with non-local qubits, as proposed in Topological Quantum Computation (TQC) protocols[23], [27], [109]. The idea is to use the inherent robustness of topological degenerated ground state spaces to encode quantum information in a locally-protected manner.

The best-established framework for quantum computing is the quantum circuit model ¹ [109]. Analogous to Computer Science's circuit model, logical gates modify the bits to obtain the desired outcome. In the quantum context, the gates are unitary matrices operating in the qubit states.

An essential set of gates that acts on a single qubit are the **Pauli matrices**. In particular, the σ_x matrix is also known as the bit flip gate and the σ_z matrix is the phase-flip gate. As the Pauli matrices act as π -rotations along the corresponding axis in the sphere, the significance of bit- and phase-flips can be better visualized in the Bloch sphere. By definition, we have the $|0\rangle$ state

¹Other models include One-way Quantum Computation and Adiabatic Quantum computation.

in the northmost point of the Bloch sphere and $|1\rangle$ state in the southmost point.

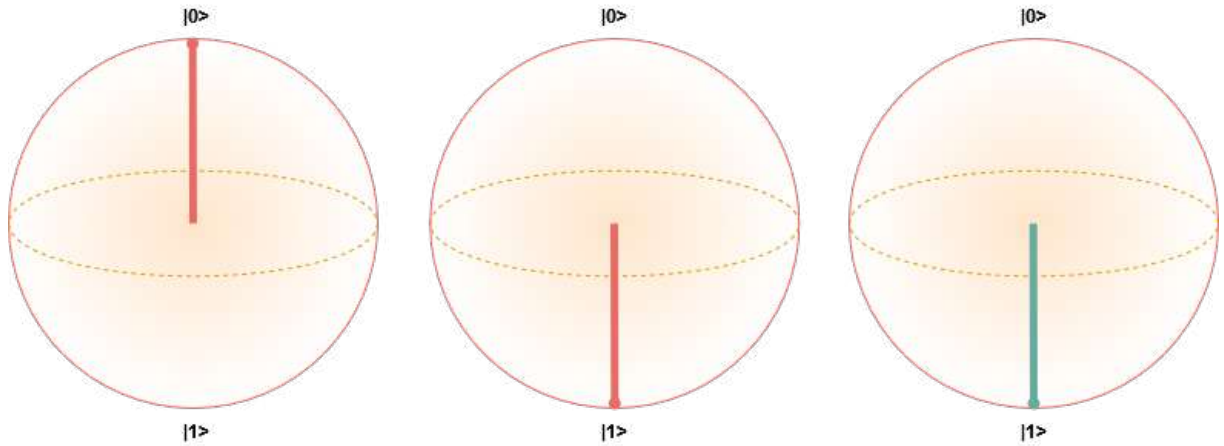


Figure B.1: Bloch sphere visualization. a - A qubit in the bloch sphere, initialized in $|0\rangle$ state. b - Action of σ_x on the initial qubit, performing a bit-flip and bringing the qubit to state $|1\rangle$. c - Action of σ_z on the bit-flipped qubit, now performing a phase-flip, indicated by the red color of the state.

The **Hadamard** gate is given by:

$$H = \frac{1}{\sqrt{2}} \begin{pmatrix} 1 & 1 \\ 1 & -1 \end{pmatrix}. \quad (\text{B.1})$$

and is the single-qubit gate most commonly used to bring qubits to a superposition - particularly, an equiprobable one.

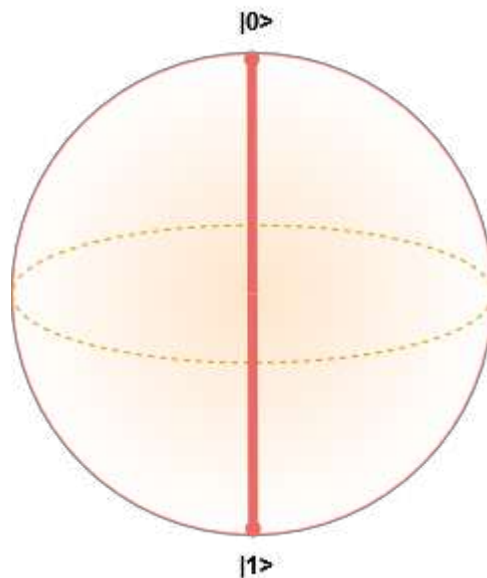


Figure B.2: Action of the Hadamard gate on the initial qubit, $|0\rangle$, creating an equal superposition of $|0\rangle$ and $|1\rangle$

For two-qubit states, a gate worth highlighting is the controlled-NOT gate (CNOT), used to create entangled states. For the first qubit being the target state and the second qubit being the control, the matrix format of CNOT is:

$$CNOT = \begin{pmatrix} 1 & 0 & 0 & 0 \\ 0 & 1 & 0 & 0 \\ 0 & 0 & 0 & 1 \\ 0 & 0 & 1 & 0 \end{pmatrix}. \quad (\text{B.2})$$

With the aid of single-qubit gates, CNOT enables the creation of all four maximally entangled states (Bell states). These states are essential for many basic quantum algorithms, such as Superdense Coding [111].

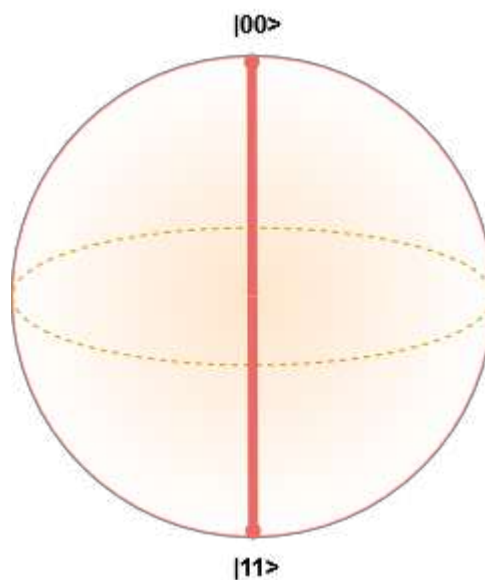


Figure B.3: Action of the CNOT gate on the initial qubit, $\frac{1}{\sqrt{2}}(|0\rangle + |1\rangle)|0\rangle$, on the Q-Sphere, a generalization of the Bloch sphere for multi-qubits. creating the entangled state $\frac{1}{\sqrt{2}}(|00\rangle + |11\rangle)$

To be able to perform any possible algorithm and to satisfy the di Vincenzo criteria for a quantum computer [112], we need a **universal set of quantum gates**. The mathematical definition of this set requires that the matrices span $U(N)$ densely. Therefore, there is some freedom of choice of individual gates.

A typical set involves basic-single qubit gates, densely spanning $U(2)$, such as the Hadamard and the S-phase gate, and a two-qubit gate capable of performing entanglement - in general,

CNOT. The S-gate is defined as:

$$S = \begin{pmatrix} 1 & 0 \\ 0 & e^{i\pi/4} \end{pmatrix} = \sqrt{\sigma_z}. \quad (\text{B.3})$$

This is the Clifford set of gates. From this set, to obtain a universal set, it is required to add the T-gate, defined as $T = \sqrt{S}$. This particular gate is unachievable via braiding of Ising anyons, thus rendering the topological implementation of quantum computing using Majoranas non-universal.

B.1 Example: Hadamard gate in the TQC hardware

Casting the x and z Pauli matrices in terms of fermionic operators:

$$\sigma_x = i(c_{1,2} + c_{1,2}^\dagger)(c_{3,4} + c_{3,4}^\dagger) \quad (\text{B.4})$$

$$\sigma_z = (2c_{1,2}^\dagger c_{1,2} - 1). \quad (\text{B.5})$$

Braiding of same-vortex Majorana Fermions, such as fermions 1 and 2, becomes:

$$B_{1,2} = \exp\left(-\frac{\pi}{4}c_1c_2\right) = \frac{1}{\sqrt{2}}(\mathcal{I} - i\sigma_z) = e^{-\frac{i\pi}{4}} \begin{pmatrix} 1 & 0 \\ 0 & i \end{pmatrix}. \quad (\text{B.6})$$

For Majoranas in different vortices, for instance, Majoranas 2 and 3, we have:

$$B_{2,3} = \exp\left(-\frac{\pi}{4}c_2c_3\right) = \frac{1}{\sqrt{2}}(\mathcal{I} - i\sigma_x) = \frac{1}{\sqrt{2}} \begin{pmatrix} 1 & -i \\ -i & 1 \end{pmatrix}. \quad (\text{B.7})$$

From the obtained matrix form of the braiding operations, the Hadamard gate (B.1) can be written of the following sequence of intra- and inter-vortices braiding:

$$H = B_{1,2}B_{2,3}B_{1,2}. \quad (\text{B.8})$$

Appendix C

Majorana-like states in vortices

The following examples showcase how states with similar signatures to Majoranas can be created and, even more strikingly, may be able to perform braiding operations.

However, braiding does not imply topological protection. In practice, as anyons are not elementary particles, but arise from effective Hamiltonians, the anyon candidate γ_i must obey:

$$[H, \gamma_i] \propto \exp(L/\xi), \quad (\text{C.1})$$

where L characterizes the distance between γ_i and other anyons present in the system and ξ is a size scale for these quasiparticles [23], [109]. To ensure topological protection, one must ensure that $L \ll \xi$, which may not always be the case.

Topological protection is, therefore, a more subtle matter: qubits analogous to Majorana qubits may be proposed, but will not necessarily have the inherent topological protection.

C.1 Poor man's majoranas

The denomination "poor man's Majorana" comes from the fact that these bound states show signatures in agreement with MBS, but only in sweet spots of the parameter space. The earliest proposal of a "poor man's Majorana" required two quantum dots and an s-wave superconductor [113]. The dots are in a homogeneous magnetic field and have different polarization angles. The angle dependence, embedded in hopping and tunneling parameters, allows for perfect Andreev reflection, as required for MBS formation. It is similar to MBS, but does not have topological protection.

A Parity qubit can be established from this system. Parity measurements must be carried

out in a non-local way, by measuring the charge in both dots simultaneously or via non-local transport. Furthermore, adding another dot may allow for creating Bell states and obtaining coherence times. A similar setup, with improved controllability, substitutes the superconductor with a third quantum dot with proximity-induced superconductivity [114].

A refined proposal exhibits quadratic protection against decoherence, an improvement in the linear protection from the original Poor Man's ideation [115]. This setup uses two quantum dots and a semi-superconductor hybrid and relies on elastic co-tunneling and crossed Andreev reflections as tuning mechanisms. The robustness, however, occurs in one of the dots, but not in both.

C.2 Quasi-majoranas

Quasimajoranas are trivial states that emerge in semi-superconductor setups with a smooth confinement tunneling barrier [116]. They mimic several topological signatures, such as quantized zero-bias peaks, the 4π Josephson effect, and the tunneling spectrum in the presence of a normal quantum dot.

Quasimajoranas are braidable via measurement-based protocols but lack true topological protection and are hence sensitive to magnetic impurities or other short-range disorder mechanisms that could break the smoothness of the potential barrier [80].

Appendix D

Quasiparticle poisoning and error correction

Despite being protected against environmental effects, qubit errors are still possible during the readout in these topological setups. The most pronounced source of error for Majorana systems consists of quasiparticle poisoning, which changes the total parity of the system. For the two-level system for Majorana qubits, parity errors translate as bit-flip errors [76].

The strategy to overcome this issue comes from the classical computing theory of error correction. Earlier studies on error correction in the quantum computing context are attributed to Peter Shor, who proposed the introduction of redundancy in encoding the bits [77]. We could, for instance, encode the physical $|0\rangle$ state as $|0000\rangle$ (which will be called “logical qubit”). If the state obtained is, $|0100\rangle$, it is most likely to represent the state $|0000\rangle$, with an isolated error.

Error-correcting codes based on redundancy are usually identified by the notation $[[N, k, d]]_f$, where f denotes that the code is for fermions, N is the number of real qubits, k is the name of logical qubits and d is the “code distance”, i.e., the smallest number of errors that need to occur to map one logical qubit to another.

D.1 Quantum Error Correction Protocols

Most quantum error-correcting (QEC) protocols in the literature apply to bosonic systems, which is not the case for superconducting qubits or Majorana-based qubits [76]. Many relevant fermionic proposals for error-correcting still point to difficulties regarding the real-space manipulation of vortices, which might drag quasiparticles and is especially detrimental in

one-dimensional systems [38].

A relevant family of protocols against this phenomenon rests on the classical Reed-Muller code and has a relatively easy physical implementation since it relies on the fixed total parity of the system [76]. For the construction of this protocol, we need to create stabilizer operators, which perform measurements on the ancillary part of the circuit to obtain information about the possible errors in the real qubits. In general, we can construct operators as a product of MZMs (denoted by γ_n):

$$O_i \sim \prod_{n=1}^{2N} \gamma_n^{v_n^i}, \quad (\text{D.1})$$

where $v_n^i = (v_1^i, v_2^i, \dots, v_{2N}^i)$ is a vector with $v_n^i = 0, 1$, equipped with \mathbb{Z}_2 addition and multiplication operations. The stabilizer matrix is defined by:

$$S = (v_1, v_2 \dots v_{2N})^T, \quad (\text{D.2})$$

with $S \cdot S^T = 0$, which characterizes binary weakly self-dual matrices. These matrices are important in both classical and quantum error-correcting schemes, since the codespace, which is the space of the codewords (valid codified bits), is given by $C = \text{span}[v^1 \dots v^m]$.

With a parity check measurement on C , it is possible to identify whether the logical bit is or is not one of the codewords, i.e., if it is an error. A particular weakly self-dual matrix, with parameters

$$RM_f(r, m) = \left[\left[2^{m-1}, 2^{m-1} - \sum_{j=0}^r \binom{m}{j}, 2^{r+1} \right] \right] \quad (\text{D.3})$$

is a subset of the Reed-Muller protocol and can be shown to correct quasiparticle poisoning [62].

Appendix E

Perturbative corrections due to the impurity potential

From Fig. 3.3 (b) it is evident that lower energy states have larger shifts than higher energy ones. This quantitative difference can be traced back to the nature of the confined wavefunctions and is obtained using perturbation theory arguments.

For an s -wave superconductor, the eigenstates are written as [117]:

$$\Psi_m(r) = \begin{pmatrix} u_m(r) \\ v_m(r) \end{pmatrix} \propto e^{-K(r)} \begin{pmatrix} J_m(k_F r) \\ J_{m+1}(k_F r) \end{pmatrix}, \quad (\text{E.1})$$

with $J_m(k_F r)$ being the order- n Bessel function of the first kind and

$$K(r) = \frac{1}{\hbar v_F} \int_0^r dr' \Delta(r'), \quad (\text{E.2})$$

where v_F is the Fermi velocity in the normal state. For low-energy in-gap states $E_n \ll \Delta_0$, we expand the superconducting pairing as $\Delta(r) \approx \frac{\Delta_0}{\xi} r$. Therefore:

$$K(r) \approx \frac{\Delta_0}{2\hbar v_F \xi} r^2 =: \frac{r^2}{2\xi^2}. \quad (\text{E.3})$$

The first-order corrections to the energy levels are given by

$$\delta E_m = \langle \Psi_m | H_{imp} | \Psi_m \rangle. \quad (\text{E.4})$$

Assuming that there are not many states inside the vortex and particularly considering the

low-energy ones, the Bessel functions can be approximated by their asymptotic form with $k_F r \ll 1$.

In this regime, the energy correction follows a power law in k_F^2/α , given by:

$$\delta E_m = \frac{\pi \delta \mu}{m! \alpha} \left(\frac{k_F^2}{4\alpha} \right)^m, \quad \alpha := \frac{1}{2\eta^2} + \frac{1}{2\tilde{\xi}^2}. \quad (\text{E.5})$$

By carrying out first-order corrections on the eigenstates, we can understand the perturbative effects of the impurity on the charge. We find:

$$\delta Q_m = 2 \sum_{n \neq m} \frac{\beta_{mn}(\delta \mu, \eta) \beta_{mn}(1, \infty)}{E_m - E_n}. \quad (\text{E.6})$$

with

$$\beta_{mn}(\delta \mu, \eta) := \langle \psi_m | \delta H | \psi_n \rangle \approx \frac{\pi \delta \mu}{m - n} \left[\frac{1}{m! n!} \left(\frac{k_F^2}{4\alpha} \right)^{\frac{m+n}{2}} \right] \frac{\Gamma((m+n+2)/2)}{\alpha}.$$

Taking the lowest order term in Eq. E.6, we find:

$$\delta Q_m = \begin{cases} \frac{\pi^2 \mu \delta \mu}{2\alpha^2 \Delta_0^2} \left(\frac{k_F^4 \tilde{\xi}^2}{2\alpha} \right)^{\frac{3}{2}} \Gamma(5/2), & m = 1 \\ \frac{\pi^2 \mu \delta \mu}{2\alpha^2 \Delta_0^2 (m-1)^3} \left[\frac{1}{m!^2} \left(\frac{k_F^4 \tilde{\xi}^2}{2\alpha} \right)^{\frac{m+1}{2}} \right] \Gamma\left(\frac{m+3}{2}\right), & m \neq 1 \end{cases}. \quad (\text{E.7})$$

Therefore we obtain a polynomial dependence on $k_F^4 \tilde{\xi}^2 / 2\alpha$. The results lead to the conclusion that the higher-energy states have smaller corrections in both energy and charge.

Appendix F

Finite Differences Method for the single vortex case

We may solve the coupled system obtained for the s -wave superconductivity, magnetic insulator and semiconductor setup by using a Finite Differences method. Although it is not particularly necessary for this Hamiltonian, it will be essential for the cases where rotational symmetry is lost, i. e. general situations with more than one vortex. It is, thus, useful to introduce the formalism for the more straightforward one-vortex case.

To apply the Finite Differences method, we interpret derivatives as a difference of infinitesimal values. We need to discretize the space by creating a mesh:

$$r(i) \rightarrow i\Delta r, \quad (\text{F.1})$$

where i indexes the position. We may write first and second derivatives using the central Euler method, which simplifies the adjustment of boundary values. This method also reduces the computational error, of order $O(r^3)$, compared to $O(r^2)$ from both forward or backwards Euler method [118]. For the radial derivatives, we have:

$$\partial_r u(i, j)_{\uparrow, \downarrow} = \frac{u(i+1, j)_{\uparrow, \downarrow} - u(i-1, j)_{\uparrow, \downarrow}}{2\Delta r} \quad (\text{F.2})$$

$$\partial_r^2 u(i, j)_{\uparrow, \downarrow} = \frac{u(i+1, j)_{\uparrow, \downarrow} - 2u(i, j)_{\uparrow, \downarrow} + u(i-1, j)_{\uparrow, \downarrow}}{\Delta r^2}. \quad (\text{F.3})$$

The corresponding equations for the discretized Hamiltonian for one vortex are:

$$\begin{aligned} & \frac{-u(i+1)_\uparrow + 2u(i)_\uparrow - u(i-1)_\uparrow}{\Delta r^2} + \frac{-u(i+1)_\uparrow + u(i-1)_\uparrow}{2\Delta r} + u(i)_\uparrow \\ & + \frac{u(i+1)_\downarrow - u(i-1)_\downarrow}{2\Delta r} + \frac{u(i)_\downarrow}{r(i)} - \Delta u(i)_\downarrow = 0 \end{aligned} \quad (\text{F.4})$$

$$\begin{aligned} & -\frac{u(i+1)_\downarrow - 2u(i)_\downarrow + u(i-1)_\downarrow}{\Delta r^2} + \frac{-u(i+1)_\downarrow + u(i-1)_\downarrow}{2\Delta r} + \frac{u(i)_\downarrow}{r(i)^2} - u(i)_\downarrow = 0. \end{aligned} \quad (\text{F.5})$$

In matrix form, we have $Mx = b$, where M is the matrix of the finite difference coefficients, x is a vector containing the spinor solution information:

$$x = (u(0)_\uparrow, \dots, u(N)_\uparrow, u(0)_\downarrow, \dots, u(N)_\downarrow)^T \quad (\text{F.6})$$

and b is the solution vector, in which we can embed boundary condition information. Before doing so, it is important to notice that the coefficient matrix will have undetermined points in the borders, ghost points. We can deal with those points by using interpolation and considering the forward Euler method in the initial borders and the backward method for the ends. Including these in the system, we obtain an invertible $2N \times 2N$ matrix with non-zero terms in four blocks:

$$M = \begin{pmatrix} \frac{2}{\Delta r^2} + 1 & -\frac{1}{\Delta r^2} + \frac{1}{2r\Delta r} & & \dots & -\Delta(0) + \frac{1}{r} & -\frac{1}{2\Delta r} & & \dots \\ -\frac{1}{\Delta r^2} + \frac{1}{2r\Delta r} & \frac{2}{\Delta r^2} + 1 & -\frac{1}{\Delta r^2} - \frac{1}{2r\Delta r} & & -\frac{1}{2\Delta r} & -\Delta(1) + \frac{1}{r} & \frac{1}{2\Delta r} & \\ & & \ddots & & & & \ddots & \\ \vdots & & & \ddots & \vdots & & & \ddots \\ \Delta(0) & \frac{1}{2\Delta r} & & \dots & \frac{2}{\Delta r^2} + \frac{1}{r^2} - 1 & -\frac{1}{\Delta r^2} + \frac{1}{2r\Delta r} & & \\ \frac{1}{2\Delta r} & \Delta(1) & & & -\frac{1}{\Delta r^2} + \frac{1}{2r\Delta r} & \frac{2}{\Delta r^2} + \frac{1}{r^2} - 1 & -\frac{1}{\Delta r^2} - \frac{1}{2r\Delta r} & \\ & & \ddots & & & & \ddots & \\ \vdots & & & & \vdots & & & \ddots \end{pmatrix}$$

. We can determine the initial value conditions by estimating $u(0)_{\uparrow,\downarrow}$, $u(1)_{\uparrow,\downarrow}$ and $u(2)_{\uparrow,\downarrow}$ and using the first two rows of the matrix. Since u_\uparrow has a $-\text{BesselJ}(0, r)$ form and u_\downarrow has a $\text{BesselJ}(1, r)$ form, from the problem, $u_\uparrow(1) = 1$ and $u_\downarrow(0) = 0$, we can determine $u(1)_{\uparrow,\downarrow}$ and $u(2)_{\uparrow,\downarrow}$ using equation (F.3) and the known values of derivatives for the Bessel function at these points. This gives $u(1)_\uparrow = 1$, $u(2)_\uparrow = -0.5\Delta r$, $u(1)_\downarrow = \Delta r^2 + 3$ and $u(2)_\downarrow = -\Delta r$. Plugging back to the matrix, we obtain $b(0)$ and $b(1)$. Similarly, for $b(2N-2)$, $b(2N-1)$ and $b(2N)$, we have the condition of

$$u(40)_{\uparrow,\downarrow} = 0.$$

It is interesting to notice that reorganizing columns and rows in M , x and b allows to obtain the boundary conditions using only $u(0)_{\uparrow,\downarrow}$, $u(1)_{\uparrow,\downarrow}$, $u(39)_{\uparrow,\downarrow}$ and $u(40)_{\uparrow,\downarrow}$. The almost diagonal form is also computationally less time consuming. The results, compared to the numerical solution obtained via NumPy's `solve_bvp` routine, are shown in figure F.1.

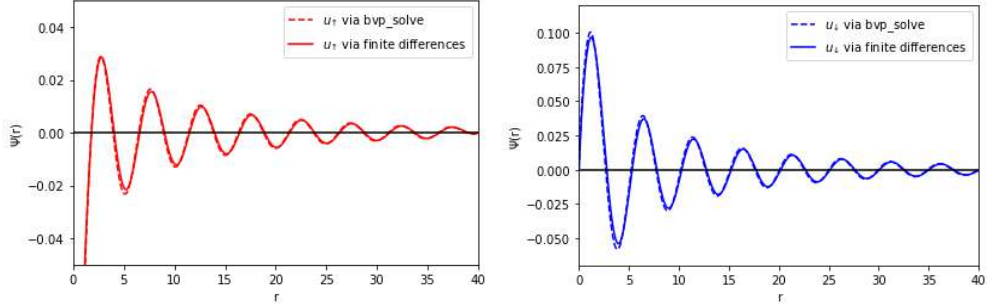


Figure F.1: Comparison between `bvp_solve` and finite differences methods.

F.1 Generalization for many vortices

To solve this coupled system by using a finite differences method, we need to discretize by creating a mesh in both r and θ coordinates:

$$r(i) \rightarrow i\Delta r, \theta(j) \rightarrow j\Delta\theta. \quad (\text{F.7})$$

By central finite differences, the derivatives in θ are:

$$\partial_{\theta} u(i, j)_{\uparrow,\downarrow} = \frac{u(i, j+1)_{\uparrow,\downarrow} - u(i, j-1)_{\uparrow,\downarrow}}{2\Delta\theta} \quad (\text{F.8})$$

$$\partial_{\theta}^2 u(i, j)_{\uparrow,\downarrow} = \frac{u(i, j+1)_{\uparrow,\downarrow} - 2u(i, j)_{\uparrow,\downarrow} + u(i, j-1)_{\uparrow,\downarrow}}{\Delta\theta^2}. \quad (\text{F.9})$$

The radial derivatives are analogous and can be found in (F.3), where we solve the system for the simpler one vortex case. The corresponding equations for the discretized Hamiltonian is:

$$\begin{aligned} & -\eta \left(\frac{u(i+1, j)_{\uparrow} - 2u(i, j)_{\uparrow} + u(i-1, j)_{\uparrow}}{\Delta r^2} + \frac{u(i+1, j)_{\uparrow} - u(i-1, j)_{\uparrow}}{r(i)2\Delta r} \right. \\ & \left. + \frac{u(i, j+1)_{\uparrow} - 2u(i, j)_{\uparrow} + u(i, j-1)_{\uparrow}}{r^2\Delta\theta^2} \right) + (V_z - \mu)u(i, j)_{\uparrow} - \Delta u(i, j)_{\downarrow} \\ & + \frac{1}{2}\alpha i e^{-i\theta} \left(i \frac{u(i+1, j)_{\downarrow} - u(i-1, j)_{\downarrow}}{2\Delta r} - \frac{u(i, j+1)_{\downarrow} - u(i, j-1)_{\downarrow}}{r(i)} \right) = 0 \end{aligned} \quad (\text{F.10})$$

$$\begin{aligned}
 & -\frac{1}{2}\alpha i e^{i\theta} \left(-i \frac{u(i+1, j)_\uparrow - u(i-1, j)_\uparrow}{2\Delta r} \right) + \Delta u(i, j)_\uparrow - (V_z + \mu)u(i, j)_\downarrow \\
 & -\eta \left(+ \frac{u(i+1, j)_\downarrow - 2u(i, j)_\downarrow + u(i-1, j)_\downarrow}{\Delta r^2} + \frac{u(i+1, j)_\downarrow - u(i-1, j)_\downarrow}{2\Delta r} \right. \\
 & \quad \left. + \frac{u(i, j+1)_\downarrow - 2u(i, j)_\downarrow + u(i, j-1)_\downarrow}{r(i)^2 \Delta \theta^2} \right) = 0. \quad (\text{F.11})
 \end{aligned}$$

Once again, we will solve $Mx = b$ where M is the matrix of the finite difference coefficients, x is a vector of the form

$$x_{r,\theta} = (u(0, 0)_\uparrow, u(1, 0)_\uparrow, \dots, u(N_r, N_\theta)_\uparrow, u(0, 0)_\downarrow, \dots, u(N_r, N_\theta)_\downarrow)^T \quad (\text{F.12})$$

and b is the solution vector and N_r, N_θ are the mesh size of the radial and angular coordinates. Here, $\dim[x_{r,\theta}] = 2N_r N_\theta$, a great increase in comparison of $\dim[x] = 2N_r$ for the one-vortex case in (F.3).

Since, in this construction of $x_{r,\theta}$, we are iterating through the radial mesh first, it means that the coefficients of the matrices obey:

$$u(i, i \pm 1)_{\uparrow, \downarrow} = u(i, i \pm N_r)_{\uparrow, \downarrow}, \quad (\text{F.13})$$

because each consecutive column value, for a fixed row value, is separated by $\pm N_r$ entries.

The non-zero coefficients of M are:

$$\begin{aligned}
 u_{\uparrow, 1}(i, i - N) &= -\frac{\eta}{r(i)^2 \Delta \theta^2} \\
 u_{\uparrow, 1}(i, i - 1) &= -\frac{\eta}{\Delta r^2} + \frac{\eta}{2r(i)\Delta r} \\
 u_{\uparrow, 1}(i, i) &= \frac{2\eta}{\Delta r^2} + \frac{2\eta}{r^2 \Delta \theta^2} + V_z - \mu \\
 u_{\uparrow, 1}(i, i + 1) &= -\frac{\eta}{\Delta r^2} - \frac{\eta}{2r(i)\Delta r} \\
 u_{\uparrow, 1}(i, i + N) &= -\frac{\eta}{r(i)^2 \Delta \theta^2}
 \end{aligned}$$

$$u_{\downarrow,1}(i, i - N) = \frac{\alpha e^{-i\theta(j)}}{2} \frac{1}{r(i)2\Delta\theta}$$

$$u_{\downarrow,1}(i, i - 1) = \frac{\alpha e^{-i\theta(j)}}{2} \frac{i}{2\Delta r}$$

$$u_{\downarrow,1}(i, i) = \lambda\Delta(i)$$

$$u_{\downarrow,1}(i, i + 1) = \frac{\alpha e^{-i\theta(j)}}{2} \frac{-i}{2\Delta r}$$

$$u_{\downarrow,1}(i, i + N) = \frac{\alpha e^{-i\theta(j)}}{2} \frac{-1}{r(i)2\Delta\theta}$$

$$u_{\uparrow,2}(i, i - N) = \frac{-\alpha e^{i\theta(j)}}{2} \frac{-1}{r(i)2\Delta\theta}$$

$$u_{\uparrow,2}(i, i - 1) = \frac{-\alpha e^{i\theta(j)}}{2} \frac{i}{2\Delta r}$$

$$u_{\uparrow,2}(i, i) = -\lambda\Delta(i)$$

$$u_{\uparrow,2}(i, i + 1) = \frac{-\alpha e^{i\theta(j)}}{2} \frac{-i}{2\Delta r}$$

$$u_{\uparrow,2}(i, i + N) = \frac{-\alpha e^{i\theta(j)}}{2} \frac{1}{r(i)2\Delta\theta}$$

$$u_{\downarrow,2}(i, i - N) = -\frac{\eta}{r(i)^2\Delta\theta^2}$$

$$u_{\downarrow,2}(i, i - 1) = -\frac{\eta}{\Delta r^2} + \frac{\eta}{2r(i)\Delta r}$$

$$u_{\downarrow,2}(i, i) = \frac{2\eta}{\Delta r^2} + \frac{2\eta}{r^2\Delta\theta^2} - V_z - \mu$$

$$u_{\downarrow,2}(i, i + 1) = -\frac{\eta}{\Delta r^2} - \frac{\eta}{2r(i)\Delta r}$$

$$u_{\downarrow,2}(i, i + N) = -\frac{\eta}{r(i)^2\Delta\theta^2} .$$

The matrix will have the following structure:

$$M = \begin{pmatrix} U_1 & D_1 \\ U_2 & D_2 \end{pmatrix},$$



where U_1 , U_2 , D_1 and D_2 correspond to submatrices for the coefficients of the up and down component for equations 1 and 2. This matrix is very sparse; for the block of up components and first equation, we have:

Appendix G

Near zero-energy Caroli-de Gennes-Matricon vortex states in the presence of impurities

In the following pages are the contents of the paper “Near zero-energy Caroli-de Gennes-Matricon vortex states in the presence of impurities”, published on Physical Review B and related to Chapter 3: “Ambiguity of MZM signatures in the presence of scalar” impurities of the present thesis.

Near zero energy Caroli–de Gennes–Matricon vortex states in the presence of impurities

Bruna S. de Mendonça ^{1,*}, Antonio L. R. Manesco,² Nancy Sandler,³ and Luis G. G. V. Dias da Silva ¹¹*Instituto de Física, Universidade de São Paulo, Rua do Matão 1371, São Paulo, São Paulo 05508-090, Brazil*²*Kavli Institute of Nanoscience, Delft University of Technology, Delft 2600 GA, The Netherlands*³*Department of Physics and Astronomy, Ohio University, Athens, Ohio 45701, USA*

(Received 19 June 2022; revised 28 April 2023; accepted 4 May 2023; published 17 May 2023)

Caroli–de Gennes–Matricon (CdGM) states are localized states with a discrete energy spectrum bound to the core of vortices in superconductors. In topological superconductors, CdGM states are predicted to coexist with zero energy, chargeless states widely known as Majorana zero modes (MZMs). Due to their energy difference, current experiments rely on scanning tunneling spectroscopy methods to distinguish between them. This work shows that electrostatic inhomogeneities can push trivial CdGM states arbitrarily close to zero energy in nontopological systems where no MZM is present. Furthermore, the BCS charge of CdGM states is suppressed under the same mechanism. Through exploration of the impurity parameter space, we establish that these two phenomena generally happen in consonance. Our results show that energy and charge shifts in CdGM may be enough to imitate the spectroscopic signatures of MZMs even in cases where the estimated CdGM level spacing (in the absence of impurities) is much larger than the typical experimental level broadening.

DOI: [10.1103/PhysRevB.107.184509](https://doi.org/10.1103/PhysRevB.107.184509)**I. INTRODUCTION**

Andreev bound states are a class of low-energy quasiparticle excitations that appear in metallic regions confined by a superconducting gap. A particular type of Andreev bound state excitations exists on zero-dimensional defects in topological superconductors. These zero energy excitations are known as Majorana zero modes (MZMs) [1–5]. Since these quasiparticles are topologically protected non-Abelian anyons [6–8], they can be used to build fault-tolerant qubits [9]. The interest in building robust quantum computers led to intense efforts to search for and identify MZMs.

The first generation of experiments to identify Majorana modes relied on measuring zero-bias peaks with tunneling probes. These peaks indicate the existence of zero energy excitations. However, to interpret these zero-bias peaks as Majorana zero modes, one must rule out the existence of other (trivial) excitations. Due to this ambiguity, together with theoretical progress showing that zero energy trivial states are possible, a new generation of experiments combining local and nonlocal probes was recently developed in nanodevice platforms [10–18].

In bulk topological superconductor candidates, an alternative procedure to detect Majorana zero modes is by piercing the superconductor with a magnetic field. With an applied field, superconducting vortices are formed. At sufficiently low electron density, these vortices should host Majorana zero modes isolated from other in-gap states. Thus, one can again probe the MZMs by scanning tunneling spectroscopy. Again, one of the fundamental challenges in verifying the presence of

MZMs in vortices of topological superconductor candidates is establishing a clear distinction from other trivial states.

In superconducting vortices, nontopological quasiparticle excitations are known as Caroli–de Gennes–Matricon (CdGM) states [19]. They appear in low-density superconducting materials, where vortices act as “quantum wells for quasiparticles” [20]. In trivial superconductors, vortices contain bound states with a low-energy spectrum given by [21] [see Figs. 1(a) and 1(b)]

$$E_m = \frac{m\Delta_0}{k_F\xi}, \quad (1)$$

where $m = (n + 1/2)$, n is an integer number, k_F is the Fermi momentum, ξ the bulk coherence length, and Δ_0 is the bulk superconducting pairing potential. The predicted spectrum of CdGM states in trivial superconductors lacks a zero energy level. These features establish the difference between CdGM and MZMs spectra and underlie the interpretation of experimental observations of zero-bias peaks inside vortices [5,22–30]. From Eq. (1), it is clear that an energy resolution better than $\Delta_0/k_F\xi$ is required to detect isolated excited levels. Since this resolution is accessible in state-of-the-art experiments, tunneling spectroscopy measurements of vortices on topological superconductors are expected to distinguish Majorana from trivial states [31–33].

Recent experiments on candidate topological superconductor materials revealed that many zero-bias peaks, associated with the presence of MZM modes, were not present in all vortices [26,30]. Furthermore, some of the detected peaks often appeared to be stabilized by nearby magnetic [28] or scalar [23] impurities. Although it is well known that zero-bias peaks can emerge in superconductors without topological properties when magnetic impurities are present, it is still an

*bsmend@usp.br

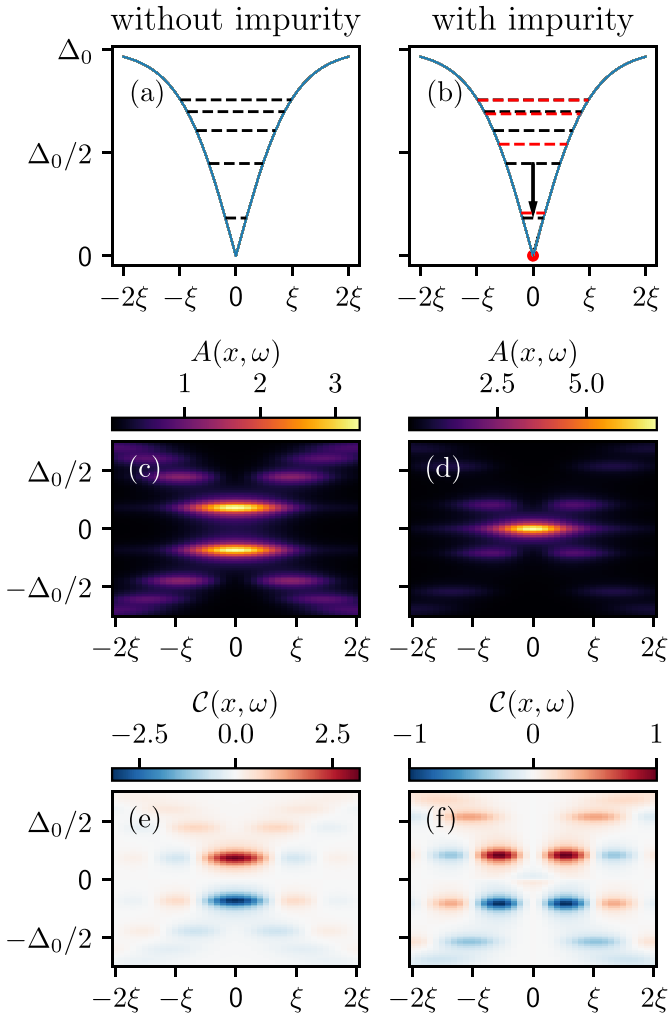


FIG. 1. Energy states inside the vortex for (a) a clean s -wave superconductor and (b) an s -wave system with screened charge impurity. The blue line shows the position-dependent superconducting order parameter, and the dashed lines schematically show the energy of in-gap CdGM states. In (b), the black dashed lines indicate the CdGM spectrum without a charged impurity, whereas the red dashed lines indicate the spectrum with the impurity. The black arrow highlights the energy shift caused by the impurity potential. (c),(d) The density of states; (e),(f) the BCS spectral charge for the s -wave system without and with impurity, respectively.

open question whether scalar impurities may produce similar effects [34].

Motivated by this scenario, we study the effect of scalar impurities in the in-gap spectrum of a two-dimensional trivial s -wave superconductor. We revisit this system because (i) an s -wave superconductor is a simple example of a trivial superconductor, and (ii) the Hamiltonian does not contain additional terms that could lead to corrections from Eq. (1). As a result, the spectra and corresponding charge distributions can be traced back unequivocally to the presence of the impurity potential.

Moreover, influenced by the new generation of experiments in nanowires, nonlocal measurements with scanning tunneling microscope measurements were suggested as a way to extract the Bardeen-Cooper-Schrieffer (BCS) charge of

in-gap vortex excitations [31]. Because trivial states have nonzero BCS charge whereas MZMs are strictly chargeless [7], information on the BCS charge, in principle, helps to distinguish CdGM states and MZMs.

Our main results are illustrated in Fig. 1, which compares the density of states and BCS charge for a trivial s -wave superconductor with and without an impurity potential. The calculations reveal that trivial CdGM states mimic MZM's signatures in two ways. First, electrostatic inhomogeneities shift the lowest CdGM state energy arbitrarily close to zero, as schematically shown in Figs. 1(a) and 1(b). Second, as the energy separation of these states become smaller than the experimental resolution—mainly limited by thermal broadening—the spectral BCS charge is also suppressed, as shown in Figs. 1(e) and 1(f). As a consequence, electrostatic inhomogeneities can make CdGM indistinguishable from MZMs when probed by scanning tunneling microscopy (STM) experiments, given the current experimental resolutions.

II. MODEL

We consider a trivial superconductor modeled as a two-dimensional electron gas with s -wave superconducting pairing. The corresponding tight-binding model on a square lattice (with lattice constant a) has a normal state Hamiltonian,

$$H_0 = (4t - \mu) \sum_i \sum_{\sigma} c_{i\sigma}^{\dagger} c_{i\sigma} - t \sum_{\langle i,j \rangle} \sum_{\sigma} c_{i\sigma}^{\dagger} c_{j\sigma}, \quad (2)$$

where μ is the on-site energy, t is the hopping constant, $c_{i\sigma}^{\dagger}$ ($c_{i\sigma}$) creates (destroys) an electron of spin σ at site i , and $\langle i, j \rangle$ denotes a sum performed over nearest neighbors. The superconducting term in the Hamiltonian is

$$H_{s\text{-wave}} = \sum_i \Delta_i^s c_{i\uparrow}^{\dagger} c_{i\downarrow}^{\dagger} + \text{H.c.},$$

$$\Delta_i^s = \Delta_0 e^{i\phi_i} \tanh\left(\frac{r_i}{\xi}\right), \quad (3)$$

where Δ_0 is the amplitude of the bulk order parameter, r_i is the distance from $\mathbf{r} = 0$ (the vortex center) to the atomic position i , ξ is the vortex radius, and $\phi_i = \arg(\mathbf{r}_i)$ is the order parameter phase, as shown in Figs. 2(a) and 2(b). Note that we treat ξ and Δ_0 as independent parameters since we do not solve the Ginzburg-Landau equations. To match the typical ratios for μ/Δ_0 reported in experiments, we set $\mu = 0.05t$ and $\Delta_0 = 0.02t$. We also set $\xi = 10a$, unless stated otherwise, to ensure that the vortex size is negligible compared to the system size ($200a \times 200a$). We treat spin as a trivial degeneracy and perform all tight-binding calculations with KWANT [35].

Figure 2(c) show the spectrum and the respective integrated BCS charge expectation values, i.e., $\mathcal{Q} \equiv \sum_i \mathcal{Q}(\mathbf{r}_i)$ where $\mathcal{Q}(\mathbf{r}_i) := \langle \Psi | c_i^{\dagger} c_i - c_i c_i^{\dagger} | \Psi \rangle$ is the local charge for a given eigenstate, of in-gap vortex states for this system as a function of the vortex radius ξ . Finite energy levels approach zero as ξ increases, as expected for quantum-confined levels.

III. EFFECTS OF AN IMPURITY POTENTIAL

An inspection of Eq. (1) suggests that local changes in the electrostatic potential can shift the energy of CdGM

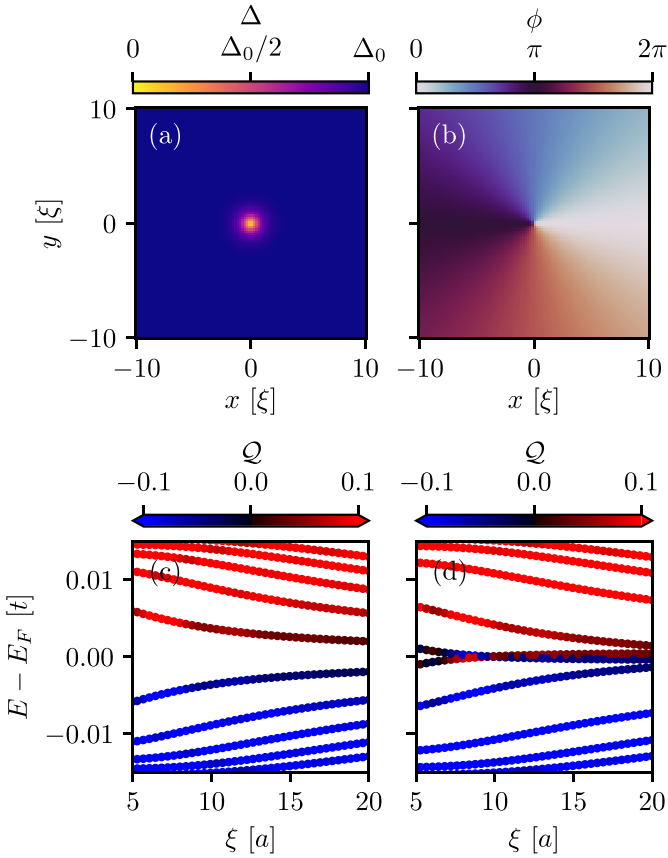


FIG. 2. (a) Magnitude and (b) phase of the superconducting order parameter [as defined in Eq. (3)]. The BCS charge-resolved spectrum of in-gap vortex states is shown for an s -wave superconductor (c) without and (d) with a screened charge impurity with $\delta\mu = 0.06t$ and $\eta = 5a$.

states arbitrarily close to zero energy. In this situation, the lowest-energy trivial states may have energy smaller than the experimental resolution, resulting in a near-zero-bias conductance peak, similar to the one produced by MZMs. To demonstrate this phenomenon, we consider the effects of an isolated screened charge impurity close to the vortex core. This choice is inspired by recent experiments in iron-based superconductors [23,26,30] showing that scalar impurities favor the presence of zero-bias peaks inside vortices.

We model the presence of a screened charged impurity on the s -wave Hamiltonian by incorporating an on-site modulation term as follows [36,37]:

$$H_{\text{imp}} = \delta\mu \sum_{i,\sigma} e^{-r_i^2/2\eta^2} c_{i\sigma}^\dagger c_{i\sigma}, \quad (4)$$

where $\delta\mu$ is the potential strength of the impurity and η is the screening length. Next, we calculate the energy spectra and the integrated charge $Q \equiv \sum_i Q(\mathbf{r}_i)$ of the Andreev quasiparticles.

Figure 3 shows the resulting low-energy spectra as a function of η and $\delta\mu$, revealing a resemblance to the spectra of a topological superconductor with a vortex. Furthermore, both charge and energy of the lowest-energy state approach zero, while the shifts of energy and charges of higher-energy

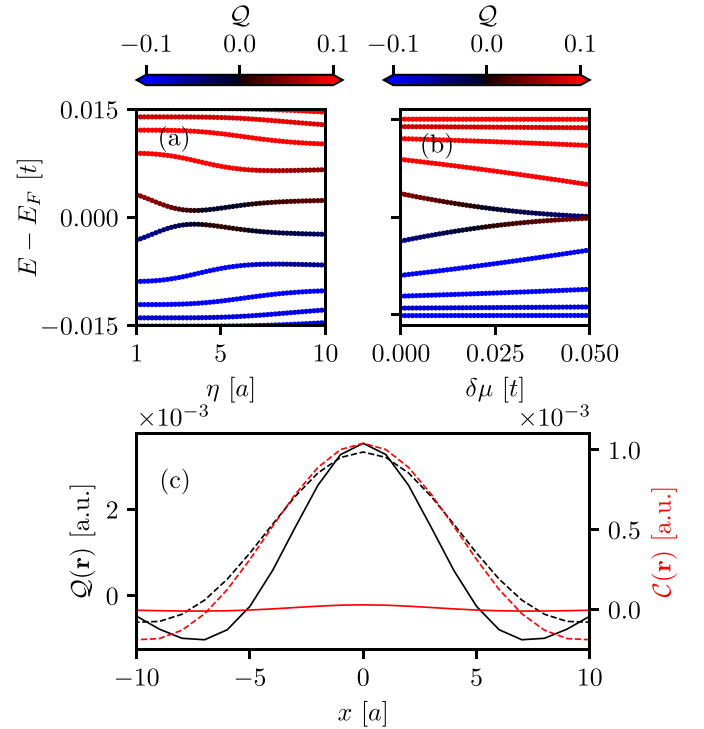


FIG. 3. BCS charge for an s -wave system with impurity. In (a) and (b), the spectrum evolves as a function of (a) impurity size η ($\delta\mu = 0.025t$) and (b) impurity strength $\delta\mu$ ($\eta = 5a$). (c) BCS charge (black) and BCS charge spectral density (red) for the lowest-energy state for a system without (dashed line) and with (solid line) an impurity with $\eta = 5a$ and $\delta\mu = 0.05t$.

states are exponentially suppressed (see the Appendix for a quantitative discussion).

The local BCS charges $Q(\mathbf{r})$ for the lowest-energy in-vortex state with and without the impurity are shown in Fig. 3(c). We verified that although the total charge is suppressed [Figs. 3(a) and 3(b)], the local charge is weakly affected by the impurity. Thus, one should be able to distinguish CdGM and Majorana states with an arbitrarily small resolution since MZMs have zero BCS charge everywhere. However, as we show in the next section, the energy shift together with level broadening of the lowest-energy CdGM states results in a vanishing spectral BCS charge.

The effects of the vortex size and impurity screening length on the energy and charge of the lowest-energy state [$E_{1/2}$, as defined in Eq. (1)] are shown in Fig. 4. The data clearly show a suppression of $E_{1/2}$ and Q on large regions of the $\{\eta, \delta\mu\}$ parameter space, indicating that the above results hold beyond the highly localized impurity regime, $\eta \ll \xi$. This also suggests that smooth fluctuations in the underlying electrostatic potential can mimic Majorana signatures. Finally, let us note that due to particle-hole symmetry, $E_{1/2}$ and Q tend to be correlated.

IV. EXPERIMENTAL RELEVANCE

In this section, we aim to establish the relevance of our results for the interpretation of current experimental data from

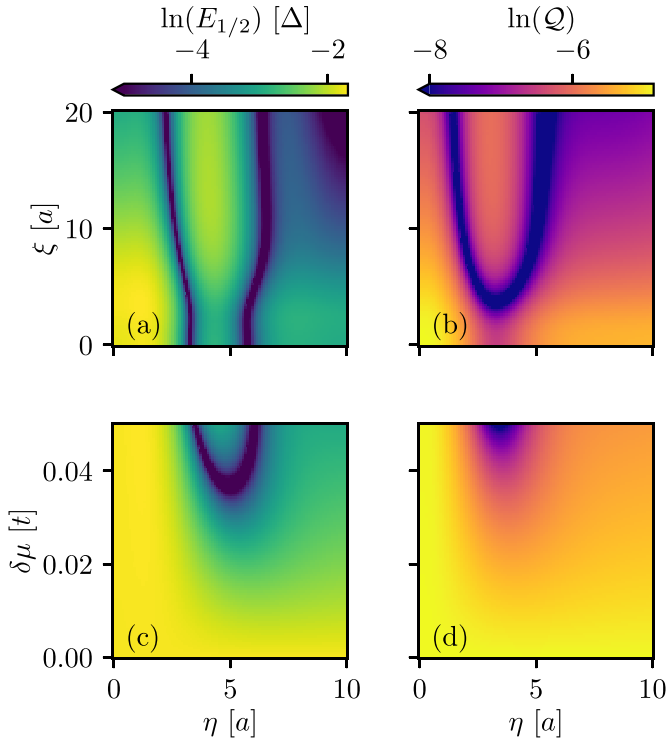


FIG. 4. Dependence of (a),(c) lowest-energy state $E_{1/2}$ and (b),(d) BCS charge on (a),(b) η and ξ and (c),(d) η and $\delta\mu$. In (a),(b), we choose $\delta\mu = 0.06t$, and in (c),(d), we choose $\xi = 5a$.

scanning tunneling spectroscopy (STS) and scanning tunneling microscopy (STM) experiments [26,29,30].

Thus far, we have discussed the changes in the global properties of the CdGM state due to the presence of scalar impurities at the vortex site. Since vortices tend to be pinned by defects and impurities [38], this picture can be favored in samples in which some degree of surface disorder is present, as seems to be the case in Fe(Se,Te) surfaces [26].

Moreover, experimental estimates of $E_{1/2}$ [as defined in Eq. (1)] are commonly used as a proxy for the position of the first CdGM state. As such, STS conductance peaks at energies below this estimate are usually “ruled out” as CdGM states [26,29]. As we have shown, such a heuristic picture is not accurate in the presence of impurities: the results shown in Figs. 2 and 3 show that the energy of the first CdGM state can be significantly lower than the value of $E_{1/2}$ estimated from bulk parameters and serve as a cautionary tale against ruling out these near zero states as CdGM states.

Another important point of attention when comparing the raw CdGM spectra with the peaks appearing in STS measurements is the role of the thermal effects of the STS peaks, which effectively sets an energy resolution. To illustrate the limitations introduced by such energy resolution, we defined the spatially resolved spectral density $A(\omega, \mathbf{r})$, and the spectral BCS charge $\mathcal{C}(\omega, \mathbf{r})$ at energy ω and position \mathbf{r} ,

$$G(\omega) = [\omega - H + i\gamma]^{-1}, \quad (5)$$

$$G(\omega, \mathbf{r}) \equiv \langle \mathbf{r} | G(\omega) | \mathbf{r} \rangle, \quad (6)$$

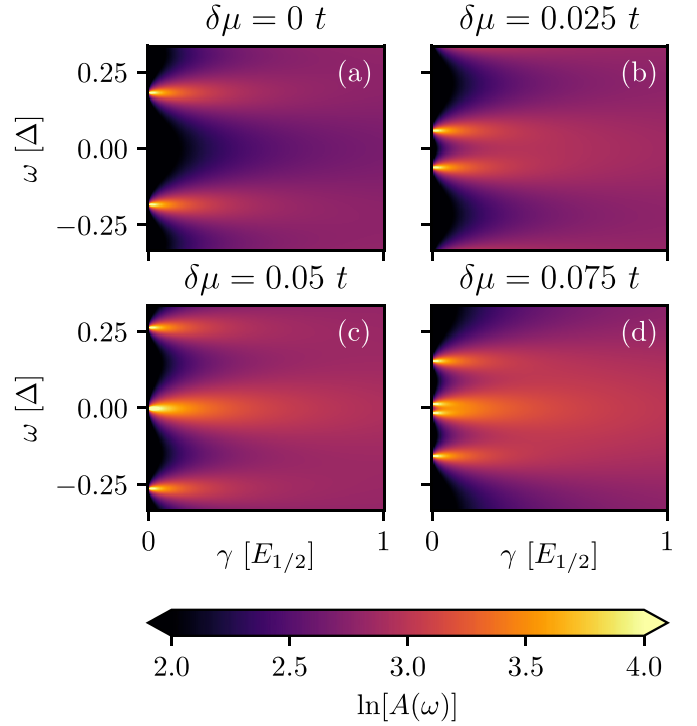


FIG. 5. Density of states $A(\omega) \equiv (-1/\pi)\text{Im Tr } G(\omega)$ of an η -wave superconductor as a function of level broadening γ ($\eta = 5a$). In (a), one can observe that the two trivial states are distinguishable in the absence of an impurity ($\delta\mu = 0$) up to $\gamma \sim E_{1/2}$. As the impurity strength increases, as shown in (b)–(d), the trivial states are shifted to smaller energies ω and therefore one cannot distinguish them even with a much smaller level broadening γ .

$$A(\omega, \mathbf{r}) \equiv -\frac{1}{\pi} \text{Im Tr}[G(\omega, \mathbf{r})], \quad (7)$$

$$\mathcal{C}(\omega, \mathbf{r}) = -\frac{1}{\pi} \text{Im Tr}[G(\omega, \mathbf{r})\mathcal{Q}(\mathbf{r})], \quad (8)$$

where γ is a positive small parameter that sets the level broadening.

Typical experimental broadenings are of the order of $\gamma \sim 0.1 \Delta_0$ (mostly arising from thermal effects), whereas the energy spacing estimated without impurities is $E_{1/2} \sim 0.5 \Delta_0$ [29]. Thus, for clean systems, scanning tunneling transport experiments should indeed be able to resolve the energies of MZMs and CdGM states. However, electrostatic inhomogeneities that make $E_{1/2} \sim \gamma$ impede a clear distinction between trivial and nontrivial states due to the constraint imposed by particle-hole symmetry that implies the shifting of positive and negative energy states towards zero energy.

We illustrate the effects of level broadening in Figs. 1 and 5. Figure 1 shows contour plots of $A(\omega, \mathbf{r})$ [Figs. 1(c) and 1(d)] and $\mathcal{C}(\omega, \mathbf{r})$ [Figs. 1(e) and 1(f)] for energies within the gap and positions inside the vortex. In the absence of impurities [Figs. 1(c) and 1(e)], one obtains peaks in $A(\omega \approx \pm E_{1/2}, \mathbf{r} \approx 0)$ originating from the first CdGM state, as expected. Some smaller peaks for excited CdGM states (with nodes at $\mathbf{r} \approx 0$) are also seen. The BCS charge for these states oscillates in position along the vortex, changing sign.

A different picture is observed in the presence of impurities and a modest thermal broadening ($\gamma/E_{1/2} \approx 0.27$). There is a single peak in the spectra charge density near zero energy $A(\omega \approx 0, \mathbf{r} \approx 0)$, and the BCS charge at these energies is very close to zero. In Fig. 5, we illustrate how much the level broadening affects our results. In the absence of impurities [Fig. 5(a)], the energies of CdGM states are determined by the bulk parameters. Therefore, the two lowest-energy peaks are distinguishable up to $\gamma/E_{1/2} \sim 1$. As the energy levels shift towards zero, the two lowest-energy peaks cannot be resolved for $\gamma/E_{1/2} \gtrsim 0.5$ [Fig. 5(b)]. In some cases, these peaks cannot be resolved even for relatively “small” broadening values of $\gamma/E_{1/2} \sim 0.1$ or lower [Figs. 5(c) and 5(d)]. In a similar manner, since particle-hole symmetry ensures that $Q_{m=1}(\mathbf{r}) = -Q_{m=-1}(\mathbf{r})$, the BCS charge also becomes negligible, as shown in Fig. 1(f).

Notice that the combined effect of the shifting of the energy levels toward zero and a moderate broadening can effectively “disguise” the lowest CdGM state as a “zero-bias peak” [see, e.g., Figs. 5(c) and 5(d)] in experiments. Interestingly, some STS experimental data show vortex bound states as peaks *near but not at* zero bias in the tunneling spectra [30], a result which is consistent with this picture.

These observations suggest that recent experiments claiming impurity-assisted formation of MZMs [23] should be interpreted carefully. At the same time that local changes in the chemical potential could lead to a topological phase transition, trivial CdGM states can also be shifted arbitrarily close to zero energy. Thus, zero-bias peaks in the vicinity of scalar impurities are ambiguous signatures and cannot fully distinguish MZM and CdGM states.

V. CONCLUDING REMARKS

Our main results can be summarized as follows: the presence of scalar impurities in vortices can modify the CdGM spectrum, leading to similar spectral properties to MZMs. We illustrate this fact in the extreme limiting case of a nontopological (*s*-wave) superconductor showing zero energy states and a vanishing global BCS charge.

This is, in fact, a very general result: local scalar perturbations in the vicinity of the vortex center lower the energy of CdGM states and suppress their total BCS charge. In particular, the energy and charge of CdGM modes can be shifted arbitrarily close to zero for a broad range of values in the parameter space of the proposed model, as shown in Fig. 4. As a consequence, such impurity-driven zero energy states cannot be set apart from topological MZMs using only local spectroscopic techniques. Furthermore, due to extrinsic broadening of the particle-hole symmetric levels, near zero energy states will render vanishing nonlocal transport signals, therefore resulting in the apparent vanishing of the BCS charge. These considerations are particularly relevant to experimental works that often rely on the fact that CdGM states have finite energy.

One possible route to complement the current local STS setups could be provided by *nonlocal* probes. As argued in Ref. [31], nonlocal transport measurements could, in principle, map the changes in the BCS charge at a local level provided that the experimental resolution allows for a distinction between MZM and CdGM states. Thus, it is important

to provide a description of the spectroscopic properties as they will be affected by the presence of electrostatic inhomogeneities.

All the scripts and resulting data used to prepare this manuscript are freely available on Zenodo [39].

ACKNOWLEDGMENTS

This study was financed in part by the Coordenação de Aperfeiçoamento de Pessoal de Nível Superior - Brasil (CAPES) - Finance Code 001. The work of A.L.R.M. was sponsored by a NWO VIDI Grant (Grant No. 016.Vidi.189.180). L.G.D.S. acknowledges financial support from Brazilian agencies FAPESP (Grant No. 2016/18495-4) and CNPq (Grants No. 423137/2018-2 and No. 309789/2020-6). Portions of this work were completed at NBI (KU) and the Physics Department at DTU (Denmark) under support from Otto Mønstedts and NORDEA foundations (N.S.).

L.G.D.S. and N.S. formulated the initial project that was later refined with contributions from all authors. B.S.M. and A.L.R.M. carried out the numerical simulations and analyzed the data with input from the other authors. A.L.R.M. identified the role of scalar impurities on the in-gap spectrum. N.S. and L.G.D.S. supervised the project. B.S.M. wrote the initial draft of the manuscript. All authors contributed to writing the manuscript.

APPENDIX: PERTURBATIVE CORRECTIONS DUE TO THE IMPURITY POTENTIAL

From Fig. 3(b), it is evident that lower-energy states have larger shifts than higher-energy ones. This quantitative difference can be traced back to the nature of the confined wave functions and is obtained using perturbation theory arguments.

For an η -wave superconductor, the eigenstates are written as [40]

$$\Psi_m(r) = \begin{pmatrix} u_m(r) \\ v_m(r) \end{pmatrix} \propto e^{-K(r)} \begin{pmatrix} J_m(k_F r) \\ J_{m+1}(k_F r) \end{pmatrix}, \quad (\text{A1})$$

with $J_m(k_F r)$ being the order- n Bessel function of the first kind and

$$K(r) = \frac{1}{\hbar v_F} \int_0^r dr' \Delta(r'), \quad (\text{A2})$$

where v_F is the Fermi velocity in the normal state. For low-energy in-gap states $E_n \ll \Delta_0$, we expand the superconducting pairing as $\Delta(r) \approx \frac{\Delta_0}{\xi} r$. Therefore,

$$K(r) \approx \frac{\Delta_0}{2\hbar v_F \xi} r^2 =: \frac{r^2}{2\xi}. \quad (\text{A3})$$

The first-order corrections to the energy levels are given by

$$\delta E_m = \langle \Psi_m | H_{imp} | \Psi_m \rangle. \quad (\text{A4})$$

Assuming that there are not many states inside the vortex and particularly considering the low-energy ones, the Bessel

functions can be approximated by their asymptotic form with $k_F r \ll 1$.

In this regime, the energy correction follows a power law in k_F^2/α , given by

$$\delta E_m = \frac{\pi \delta \mu}{m! \alpha} \left(\frac{k_F^2}{4\alpha} \right)^m, \quad \alpha := \frac{1}{2\eta^2} + \frac{1}{2\tilde{\xi}^2}. \quad (\text{A5})$$

By carrying out first-order corrections on the eigenstates, we can understand the perturbative effects of the impurity on the charge. We find

$$\delta Q_m = 2 \sum_{n \neq m} \frac{\beta_{mn}(\delta \mu, \eta) \beta_{mn}(1, \infty)}{E_m - E_n}, \quad (\text{A6})$$

with

$$\begin{aligned} \beta_{mn}(\delta \mu, \eta) &:= \langle \psi_m | \delta H | \psi_n \rangle \\ &\approx \frac{\pi \delta \mu}{m-n} \left[\frac{1}{m! n!} \left(\frac{k_F^2}{4\alpha} \right)^{\frac{m+n}{2}} \right] \frac{\Gamma[(m+n+2)/2]}{\alpha}. \end{aligned}$$

Taking the lowest-order term in Eq. (A6), we find

$$\delta Q_m = \begin{cases} \frac{\pi^2 \mu \delta \mu}{2\alpha^2 \Delta_0^2} \left(\frac{k_F^2 \tilde{\xi}^2}{2\alpha} \right)^{\frac{3}{2}} \Gamma(5/2), & m = 1 \\ \frac{\pi^2 \mu \delta \mu}{2\alpha^2 \Delta_0^2 (m-1)^3} \left[\frac{1}{m!^2} \left(\frac{k_F^2 \tilde{\xi}^2}{2\alpha} \right)^{\frac{m+1}{2}} \right] \Gamma\left(\frac{m+3}{2}\right), & m \neq 1. \end{cases} \quad (\text{A7})$$

Therefore, we obtain a polynomial dependence on $k_F^4 \tilde{\xi}^2 / 2\alpha$. The results lead to the conclusion that the higher-energy states have smaller corrections in both energy and charge.

-
- [1] C. Beenakker, Search for non-Abelian Majorana braiding statistics in superconductors, *SciPost Phys. Lect. Notes* **1**, 15 (2020).
- [2] S. Das Sarma, M. Freedman, and C. Nayak, Majorana zero modes and topological quantum computation, *npj Quantum Inf.* **1**, 15001 (2015).
- [3] L. Fu and C. L. Kane, Superconducting Proximity Effect and Majorana Fermions at the Surface of a Topological Insulator, *Phys. Rev. Lett.* **100**, 096407 (2008).
- [4] J. D. Sau, R. M. Lutchyn, S. Tewari, and S. Das Sarma, Generic New Platform for Topological Quantum Computation Using Semiconductor Heterostructures, *Phys. Rev. Lett.* **104**, 040502 (2010).
- [5] L.-Y. Kong and H. Ding, Emergent vortex Majorana zero mode in iron-based superconductors, *Acta Phys. Sin.* **69**, 110301 (2020).
- [6] A. Kitaev, Fault-tolerant quantum computation by anyons, *Ann. Phys.* **303**, 2 (2003).
- [7] R. Aguado, Majorana quasiparticles in condensed matter, *Rivista del Nuovo Cimento* **40**, 523 (2017).
- [8] J. Alicea, New directions in the pursuit of Majorana fermions in solid state systems, *Rep. Prog. Phys.* **75**, 076501 (2012).
- [9] C. Nayak, S. H. Simon, A. Stern, M. Freedman, and S. Das Sarma, Non-Abelian anyons and topological quantum computation, *Rev. Mod. Phys.* **80**, 1083 (2008).
- [10] H. Pan and S. Das Sarma, Physical mechanisms for zero-bias conductance peaks in Majorana nanowires, *Phys. Rev. Res.* **2**, 013377 (2020).
- [11] T. O. Rosdahl, A. Vuik, M. Kjaergaard, and A. R. Akhmerov, Andreev rectifier: A nonlocal conductance signature of topological phase transitions, *Phys. Rev. B* **97**, 045421 (2018).
- [12] H. Zhang, D. E. Liu, M. Wimmer, and L. P. Kouwenhoven, Next steps of quantum transport in majorana nanowire devices, *Nat. Commun.* **10**, (2019).
- [13] G. C. Ménard, G. L. R. Anselmetti, E. A. Martinez, D. Puglia, F. K. Malinowski, J. S. Lee, S. Choi, M. Pendharkar, C. J. Palmström, K. Flensberg, C. M. Marcus, L. Casparis, and A. P. Higginbotham, Conductance-Matrix Symmetries of a Three-Terminal Hybrid Device, *Phys. Rev. Lett.* **124**, 036802 (2020).
- [14] J. Danon, A. B. Hellenes, E. B. Hansen, L. Casparis, A. P. Higginbotham, and K. Flensberg, Nonlocal Conductance Spectroscopy of Andreev Bound States: Symmetry Relations and BCS Charges, *Phys. Rev. Lett.* **124**, 036801 (2020).
- [15] Z. Cao, G. Zhang, H. Zhang, W.-X. He, C. Zeng, K. He, and D. E. Liu, Probing electron-hole weights of an Andreev bound state by transient currents, *Phys. Rev. B* **106**, 075416 (2022).
- [16] N. van Loo, G. P. Mazur, T. Dvir, G. Wang, R. C. Dekker, J. Y. Wang, M. Lemang, C. Sfligoj, A. Bordin, D. van Driel, G. Badawy, S. Gazibegovic, E. P. A. M. Bakkers, and L. P. Kouwenhoven, Electrostatic control of the proximity effect in the bulk of semiconductor-superconductor hybrids, [arXiv:2211.06709](https://arxiv.org/abs/2211.06709).
- [17] D. I. Pikulin, B. van Heck, T. Karzig, E. A. Martinez, B. Nijholt, T. Laeven, G. W. Winkler, J. D. Watson, S. Heedt, M. Temurhan, V. Svidenko, R. M. Lutchyn, M. Thomas, G. de Lange, L. Casparis, and C. Nayak, Protocol to identify a topological superconducting phase in a three-terminal device, [arXiv:2103.12217](https://arxiv.org/abs/2103.12217).
- [18] M. Aghaee, A. Akkala, Z. Alam, R. Ali, A. A. Ramirez, M. Andrzejczuk, A. E. Antipov, M. Astafev, B. Bauer, J. Becker *et al.*, InAs-Al hybrid devices passing the topological gap protocol, [arXiv:2207.02472](https://arxiv.org/abs/2207.02472).
- [19] E. Prada, P. San-Jose, M. W. A. de Moor, A. Geresdi, E. J. H. Lee, J. Klinovaja, D. Loss, J. Nygård, R. Aguado, and L. P. Kouwenhoven, From Andreev to Majorana bound states in hybrid superconductor-semiconductor nanowires, *Nat. Rev. Phys.* **2**, 575 (2020).
- [20] A. A. Abrikosov, Nobel lecture: Type-II superconductors and the vortex lattice, *Rev. Mod. Phys.* **76**, 975 (2004).
- [21] C. Caroli, P. G. de Gennes, and J. Matricon, Bound fermion states on a vortex line in a type ii superconductor, *Phys. Lett.* **9**, 307 (1964).
- [22] J.-P. Xu, M.-X. Wang, Z. L. Liu, J.-F. Ge, X. Yang, C. Liu, Z. A. Xu, D. Guan, C. L. Gao, D. Qian, Y. Liu, Q.-H. Wang, F.-C. Zhang, Q.-K. Xue, and J.-F. Jia, Experimental Detection of a Majorana Mode in the Core of a Magnetic Vortex Inside a Topological Insulator-Superconductor $\text{Bi}_2\text{Te}_3/\text{NbSe}_2$ Heterostructure, *Phys. Rev. Lett.* **114**, 017001 (2015).
- [23] L. Kong, L. Cao, S. Zhu, M. Papaj, G. Dai, G. Li, P. Fan, W. Liu, F. Yang, X. Wang *et al.*, Majorana zero modes in impurity-assisted vortex of LiFeAs superconductor, *Nat. Commun.* **12**, 4146 (2021).
- [24] Z. Hou and J. Klinovaja, Zero-energy Andreev bound states in iron-based superconductor $\text{Fe}(\text{Te}, \text{Se})$, [arXiv:2109.08200](https://arxiv.org/abs/2109.08200).

- [25] K. Jiang, X. Dai, and Z. Wang, Quantum Anomalous Vortex and Majorana Zero Mode in Iron-Based Superconductor Fe(Te,Se), *Phys. Rev. X* **9**, 011033 (2019).
- [26] T. Machida, Y. Sun, S. Pyon, S. Takeda, Y. Kohsaka, T. Hanaguri, T. Sasagawa, and T. Tamegai, Zero-energy vortex bound state in the superconducting topological surface state of Fe(Se,Te), *Nat. Mater.* **18**, 811 (2019).
- [27] H. Kim, Y. Nagai, L. Rózsa, D. Schreyer, and R. Wiesendanger, Anisotropic non-split zero-energy vortex bound states in a conventional superconductor, *Appl. Phys. Rev.* **8**, 031417 (2021).
- [28] D. Wang, J. Wiebe, R. Zhong, G. Gu, and R. Wiesendanger, Spin-Polarized Yu-Shiba-Rusinov States in an Iron-Based Superconductor, *Phys. Rev. Lett.* **126**, 076802 (2021).
- [29] D. Wang, L. Kong, P. Fan, H. Chen, S. Zhu, W. Liu, L. Cao, Y. Sun, S. Du, J. Schneeloch, R. Zhong, G. Gu, L. Fu, H. Ding, and H.-J. Gao, Evidence for Majorana bound states in an iron-based superconductor, *Science* **362**, 333 (2018).
- [30] M. Chen, X. Chen, H. Yang, Z. Du, X. Zhu, E. Wang, and H.-H. Wen, Discrete energy levels of Caroli–de Gennes–Matricon states in quantum limit in FeTe_{0.55}Se_{0.45}, *Nat. Commun.* **9**, 970 (2018).
- [31] B. Sbierski, M. Geier, A.-P. Li, M. Brahlek, R. G. Moore, and J. E. Moore, Identifying Majorana vortex modes via nonlocal transport, *Phys. Rev. B* **106**, 035413 (2022).
- [32] C.-K. Chiu, T. Machida, Y. Huang, T. Hanaguri, and F.-C. Zhang, Scalable Majorana vortex modes in iron-based superconductors, *Sci. Adv.* **6**, eaay0443 (2020).
- [33] C. Christian, E. F. Dumitrescu, and G. B. Halász, Robustness of vortex-bound Majorana zero modes against correlated disorder, *Phys. Rev. B* **104**, L020505 (2021).
- [34] X. Chen, W. Duan, X. Fan, W. Hong, K. Chen, H. Yang, S. Li, H. Luo, and H.-H. Wen, Friedel Oscillations of Vortex Bound States Under Extreme Quantum Limit in KCa₂Fe₄As₄F₂, *Phys. Rev. Lett.* **126**, 257002 (2021).
- [35] C. W. Groth, M. Wimmer, A. R. Akhmerov, and X. Waintal, KWANT: A software package for quantum transport, *New J. Phys.* **16**, 063065 (2014).
- [36] A. Rycerz, J. Tworzydło, and C. Beenakker, Anomalously large conductance fluctuations in weakly disordered graphene, *Europhys. Lett.* **79**, 57003 (2007).
- [37] J. Wurm, M. Wimmer, and K. Richter, Symmetries and the conductance of graphene nanoribbons with long-range disorder, *Phys. Rev. B* **85**, 245418 (2012).
- [38] A. Kreisel, P. J. Hirschfeld, and B. M. Andersen, On the remarkable superconductivity of FeSe and its close cousins, *Symmetry* **12**, 1402 (2020).
- [39] B. S. de Mendonça, A. L. R. Manesco, N. Sandler, and L. G. D. da Silva, Can Caroli–de Gennes–Matricon and Majorana vortex states be distinguished in the presence of impurities? (2022), Zenodo, doi:10.5281/zenodo.6444338.
- [40] U. E. Khodaeva and M. A. Skvortsov, Vortex core near planar defects in a clean layered superconductor, *Phys. Rev. B* **105**, 134504 (2022).

Bibliography

- [1] J. Alicea, “New directions in the pursuit of majorana fermions in solid state systems,” *Reports on Progress in Physics*, vol. 75, no. 7, p. 076 501, 2012, issn: 1361-6633. doi: [10.1088/0034-4885/75/7/076501](https://doi.org/10.1088/0034-4885/75/7/076501). [Online]. Available: <http://dx.doi.org/10.1088/0034-4885/75/7/076501>.
- [2] S. Frolov, M. Manfra, and J. Sau, “Topological superconductivity in hybrid devices,” *Nature Physics*, vol. 16, pp. 718–724, Jul. 2020. doi: [10.1038/s41567-020-0925-6](https://doi.org/10.1038/s41567-020-0925-6).
- [3] H. Pan and S. Das Sarma, “Physical mechanisms for zero-bias conductance peaks in majorana nanowires,” *Phys. Rev. Research*, vol. 2, p. 013 377, 1 Mar. 2020. doi: [10.1103/PhysRevResearch.2.013377](https://doi.org/10.1103/PhysRevResearch.2.013377). [Online]. Available: <https://link.aps.org/doi/10.1103/PhysRevResearch.2.013377>.
- [4] E. Prada, P. San-Jose, M. W. A. de Moor, *et al.*, “From andreev to majorana bound states in hybrid superconductor–semiconductor nanowires,” *Nature Reviews Physics*, vol. 2, no. 10, pp. 575–594, Sep. 2020, issn: 2522-5820. doi: [10.1038/s42254-020-0228-y](https://doi.org/10.1038/s42254-020-0228-y). [Online]. Available: <http://dx.doi.org/10.1038/s42254-020-0228-y>.
- [5] K. K. Likharev, “Superconducting weak links,” *Rev. Mod. Phys.*, vol. 51, pp. 101–159, 1 Jan. 1979. doi: [10.1103/RevModPhys.51.101](https://doi.org/10.1103/RevModPhys.51.101). [Online]. Available: <https://link.aps.org/doi/10.1103/RevModPhys.51.101>.
- [6] Z. Hou and J. Klinovaja, “Zero-energy andreev bound states in iron-based superconductor fe(te,se),” *arXiv e-prints*, arXiv:2109.08200, arXiv:2109.08200, Sep. 2021. arXiv: [2109.08200](https://arxiv.org/abs/2109.08200) [cond-mat.mes-hall]. [Online]. Available: <https://ui.adsabs.harvard.edu/abs/2021arXiv210908200H>.
- [7] D. Wang, L. Kong, P. Fan, *et al.*, “Evidence for majorana bound states in an iron-based superconductor,” *Science*, vol. 362, no. 6412, pp. 333–335, 2018, issn: 1095-9203. doi: [10.1126/science.aao1797](https://doi.org/10.1126/science.aao1797). [Online]. Available: <http://dx.doi.org/10.1126/science.aao1797>.
- [8] B. S. de Mendonça, A. L. R. Manesco, N. Sandler, and L. G. G. V. Dias da Silva, “Near zero energy caroli–de gennes–matricon vortex states in the presence of impurities,” *Phys. Rev. B*, vol. 107, p. 184 509, 18 May 2023. doi: [10.1103/PhysRevB.107.184509](https://doi.org/10.1103/PhysRevB.107.184509). [Online]. Available: <https://link.aps.org/doi/10.1103/PhysRevB.107.184509>.
- [9] J. D. Sau, S. Tewari, R. M. Lutchyn, T. D. Stanescu, and S. D. Sarma, “Non-abelian quantum order in spin-orbit-coupled semiconductors: Search for topological majorana particles in solid-state systems,” *Phys. Rev. B*, vol. 82, no. 21, p. 214 509, 2010.

- [10] J. D. Sau, R. M. Lutchyn, S. Tewari, and S. Das Sarma, “Generic new platform for topological quantum computation using semiconductor heterostructures,” *Phys. Rev. Lett.*, vol. 104, p. 040502, 4 2010. doi: [10.1103/PhysRevLett.104.040502](https://doi.org/10.1103/PhysRevLett.104.040502). [Online]. Available: <https://link.aps.org/doi/10.1103/PhysRevLett.104.040502>.
- [11] J. M. Kosterlitz and D. Thouless, “Long range order and metastability in two dimensional solids and superfluids.(application of dislocation theory),” *Journal of Physics C: Solid State Physics*, vol. 5, no. 11, p. L124, 1972.
- [12] J. M. Kosterlitz and D. J. Thouless, “Ordering, metastability and phase transitions in two-dimensional systems,” *Journal of Physics C: Solid State Physics*, vol. 6, no. 7, p. 1181, 1973.
- [13] F. D. M. Haldane, “Continuum dynamics of the 1-d heisenberg antiferromagnet: Identification with the o (3) nonlinear sigma model,” *Physics letters a*, vol. 93, no. 9, pp. 464–468, 1983.
- [14] F. D. M. Haldane, “Nonlinear field theory of large-spin heisenberg antiferromagnets: Semiclassically quantized solitons of the one-dimensional easy-axis néel state,” *Physical review letters*, vol. 50, no. 15, p. 1153, 1983.
- [15] M. F. Atiyah, “Topological quantum field theory,” *Publications Mathématiques de l’IHÉS*, vol. 68, pp. 175–186, 1988.
- [16] E. Witten, “Topological quantum field theory,” *Communications in Mathematical Physics*, vol. 117, no. 3, pp. 353–386, 1988.
- [17] Y. Choi, H. Kim, Y. Peng, *et al.*, “Correlation-driven topological phases in magic-angle twisted bilayer graphene,” *Nature*, vol. 589, no. 7843, pp. 536–541, 2021.
- [18] A. Y. Kitaev, “Fault-tolerant quantum computation by anyons,” *Annals of physics*, vol. 303, no. 1, pp. 2–30, 2003.
- [19] X.-G. Wen, “Mean-field theory of spin-liquid states with finite energy gap and topological orders,” *Physical Review B*, vol. 44, no. 6, p. 2664, 1991.
- [20] A. Shapere and F. Wilczek, *Geometric phases in physics*. World scientific, 1989, vol. 5.
- [21] D. J. Thouless, M. Kohmoto, M. P. Nightingale, and M. den Nijs, “Quantized hall conductance in a two-dimensional periodic potential,” *Physical review letters*, vol. 49, no. 6, p. 405, 1982.
- [22] D. Xiao, M.-C. Chang, and Q. Niu, “Berry phase effects on electronic properties,” *Reviews of modern physics*, vol. 82, no. 3, p. 1959, 2010.
- [23] T. D. Stanescu, *Introduction to topological quantum matter & quantum computation*. CRC Press, 2016.
- [24] B. A. Bernevig, *Topological insulators and topological superconductors*. Princeton university press, 2013.
- [25] R. Aguado, “Majorana quasiparticles in condensed matter,” *La Rivista del Nuovo Cimento*, vol. 40, pp. 523–593, 2017.
- [26] E. Majorana, “Teoria simmetrica dell’elettrone e del positrone,” *Il Nuovo Cimento (1924-1942)*, vol. 14, no. 4, pp. 171–184, 1937.
- [27] S. Das Sarma, M. Freedman, and C. Nayak, “Majorana zero modes and topological quantum computation,” *npj Quantum Information*, vol. 1, Jan. 2015. doi: [10.1038/npjqi.2015.1](https://doi.org/10.1038/npjqi.2015.1).

- [28] C. Nayak, S. H. Simon, A. Stern, M. Freedman, and S. Das Sarma, “Non-abelian anyons and topological quantum computation,” *Rev. Mod. Phys.*, vol. 80, pp. 1083–1159, 3 2008. doi: [10.1103/RevModPhys.80.1083](https://doi.org/10.1103/RevModPhys.80.1083). [Online]. Available: <https://link.aps.org/doi/10.1103/RevModPhys.80.1083>.
- [29] C. Beenakker, “Search for non-abelian majorana braiding statistics in superconductors,” *SciPost Physics Lecture Notes*, Aug. 2020. doi: [10.21468/SciPostPhysLectNotes.15](https://doi.org/10.21468/SciPostPhysLectNotes.15).
- [30] C. Kallin, “Chiral p-wave order in Sr_2RuO_4 ,” *Reports on Progress in Physics*, vol. 75, no. 4, p. 042 501, 2012.
- [31] A. P. Mackenzie and Y. Maeno, “The superconductivity of Sr_2RuO_4 and the physics of spin-triplet pairing,” *Reviews of Modern Physics*, vol. 75, no. 2, p. 657, 2003.
- [32] C. W. Hicks, J. R. Kirtley, T. M. Lippman, *et al.*, “Limits on superconductivity-related magnetization in Sr_2RuO_4 and $\text{PrOs}_4\text{Sb}_{12}$ from scanning squid microscopy,” *Physical Review B*, vol. 81, no. 21, p. 214 501, 2010.
- [33] V. Mourik, K. Zuo, S. M. Frolov, S. Plissard, E. P. Bakkers, and L. P. Kouwenhoven, “Signatures of majorana fermions in hybrid superconductor-semiconductor nanowire devices,” *Science*, vol. 336, no. 6084, pp. 1003–1007, 2012.
- [34] S. Sasaki, S. De Franceschi, J. Elzerman, *et al.*, “Kondo effect in an integer-spin quantum dot,” *Nature*, vol. 405, no. 6788, pp. 764–767, 2000.
- [35] S. D. Sarma and H. Pan, “Disorder-induced zero-bias peaks in majorana nanowires,” *arXiv preprint arXiv:2103.05628*, 2021.
- [36] H. Zhang, C.-X. Liu, S. Gazibegovic, *et al.*, “Retracted article: Quantized majorana conductance,” *Nature*, vol. 556, no. 7699, pp. 74–79, 2018.
- [37] H. Zhang, M. W. de Moor, J. D. Bommer, *et al.*, “Large zero-bias peaks in insb-al hybrid semiconductor-superconductor nanowire devices,” *arXiv preprint arXiv:2101.11456*, 2021.
- [38] F. L. Pedrocchi, N. Bonesteel, and D. P. DiVincenzo, “Monte carlo studies of the self-correcting properties of the majorana quantum error correction code under braiding,” *Phys. Rev. B*, vol. 92, no. 11, p. 115 441, 2015.
- [39] P. Bonderson, M. Freedman, and C. Nayak, “Measurement-only topological quantum computation,” *Physical review letters*, vol. 101, no. 1, p. 010 501, 2008.
- [40] L. Fu and C. L. Kane, “Superconducting proximity effect and majorana fermions at the surface of a topological insulator,” *Phys. Rev. Lett.*, vol. 100, p. 096 407, 9 2008. doi: [10.1103/PhysRevLett.100.096407](https://doi.org/10.1103/PhysRevLett.100.096407). [Online]. Available: <https://link.aps.org/doi/10.1103/PhysRevLett.100.096407>.
- [41] B. Snierski, M. Geier, A.-P. Li, M. Brahlek, R. G. Moore, and J. E. Moore, “Identifying Majorana vortex modes via non-local transport,” *arXiv e-prints*, arXiv:2107.11226, arXiv:2107.11226, Jul. 2021. arXiv: [2107.11226](https://arxiv.org/abs/2107.11226) [[cond-mat.mes-hall](https://arxiv.org/abs/2107.11226)].
- [42] H. KAMERLINGH ONNES, “The superconductivity of mercury,” *Comm. Phys. Lab. Univ. Leiden*, vol. 122, pp. 122–124, 1911.
- [43] R. Ochsenfeld and W. Meissner, “Ein neuer effekt bei eintritt der supraleitfähigkeit,” *Naturwissenschaften*, vol. 21, pp. 787–788, 1933.
- [44] H. London and F. London, “Proc. roy. soc,” *Lond., Ser. A*, vol. 149, p. 71, 1935.

- [45] S. M. Girvin and K. Yang, *Modern condensed matter physics*. Cambridge University Press, 2019.
- [46] P.-G. De Gennes and P. A. Pincus, *Superconductivity of metals and alloys*. CRC Press, 2018.
- [47] M. Tinkham, *Introduction to superconductivity*. Courier Corporation, 2004.
- [48] A. A. Abrikosov and L. P. Gor'kov, "Contribution to the theory of superconducting alloys with paramagnetic impurities," *Zhur. Eksptl'. i Teoret. Fiz.*, vol. 39, 1960.
- [49] H. Shiba, "Classical spins in superconductors," *Progress of theoretical Physics*, vol. 40, no. 3, pp. 435–451, 1968. doi: [10.1143/PTP.40.435](https://doi.org/10.1143/PTP.40.435). [Online]. Available: <https://www.osti.gov/biblio/4833205>.
- [50] C. Caroli, P. G. de Gennes, and J. Matricon, "Bound fermion states on a vortex line in a type ii superconductor," *Phys. Letters*, vol. Vol: 9, no. 4, May 1964. doi: [10.1016/0031-9163\(64\)90375-0](https://doi.org/10.1016/0031-9163(64)90375-0). [Online]. Available: <https://www.osti.gov/biblio/4055167>.
- [51] M. Chen, X. Chen, H. Yang, *et al.*, "Discrete energy levels of caroli-de gennes-matrimon states in quantum limit in fete0. 55se0. 45," *Nature communications*, vol. 9, no. 1, pp. 1–7, 2018.
- [52] T. Lancaster and S. J. Blundell, *Quantum field theory for the gifted amateur*. OUP Oxford, 2014.
- [53] A. Altland and B. D. Simons, *Condensed matter field theory*. Cambridge university press, 2010.
- [54] M. Sato and Y. Ando, "Topological superconductors: A review," *Reports on Progress in Physics*, vol. 80, no. 7, p. 076 501, 2017.
- [55] T. Fukui, K. Shiozaki, T. Fujiwara, and S. Fujimoto, "Bulk-edge correspondence for chern topological phases: A viewpoint from a generalized index theorem," *Journal of the Physical Society of Japan*, vol. 81, no. 11, p. 114 602, 2012.
- [56] M. Nakahara, *Geometry, topology and physics*. CRC Press, 2003.
- [57] M. Leijnse and K. Flensberg, "Introduction to topological superconductivity and majorana fermions," *Semiconductor Science and Technology*, vol. 27, no. 12, p. 124 003, 2012.
- [58] S. An, P. Jiang, H. Choi, *et al.*, "Braiding of abelian and non-abelian anyons in the fractional quantum hall effect," *arXiv preprint arXiv:1112.3400*, 2011.
- [59] J. Nakamura, S. Liang, G. C. Gardner, and M. J. Manfra, "Direct observation of anyonic braiding statistics," *Nature Physics*, vol. 16, no. 9, pp. 931–936, 2020.
- [60] É. Cartan, "Sur une classe remarquable d'espaces de riemann," *Bulletin de la Société mathématique de France*, vol. 54, pp. 214–264, 1926.
- [61] G. Moore and N. Read, "Nonabelions in the fractional quantum hall effect," *Nuclear Physics B*, vol. 360, no. 2-3, pp. 362–396, 1991.
- [62] S. Bravyi, "Universal quantum computation with the $\nu=5/2$ fractional quantum hall state," *Phys. Rev. A*, vol. 73, no. 4, p. 042 313, 2006.
- [63] R. B. Laughlin, "Anomalous quantum hall effect: An incompressible quantum fluid with fractionally charged excitations," *Physical Review Letters*, vol. 50, no. 18, p. 1395, 1983.

- [64] F. D. M. Haldane, “Fractional quantization of the hall effect: A hierarchy of incompressible quantum fluid states,” *Physical Review Letters*, vol. 51, no. 7, p. 605, 1983.
- [65] B. I. Halperin, “Statistics of quasiparticles and the hierarchy of fractional quantized hall states,” *Physical Review Letters*, vol. 52, no. 18, p. 1583, 1984.
- [66] E. Grosfeld and K. Schoutens, “Non-abelian anyons: When ising meets fibonacci,” *Physical review letters*, vol. 103, no. 7, p. 076 803, 2009.
- [67] C. Schrade and L. Fu, “Majorana superconducting qubit,” *Physical Review Letters*, vol. 121, no. 26, p. 267 002, 2018.
- [68] S. Hoffman, C. Schrade, J. Klinovaja, and D. Loss, “Universal quantum computation with hybrid spin-majorana qubits,” *Phys. Rev. B*, vol. 94, no. 4, p. 045 316, 2016.
- [69] J. Schechter and J. W. Valle, “Neutrinoless double- β decay in $su(2) \times u(1)$ theories,” *Physical Review D*, vol. 25, no. 11, p. 2951, 1982.
- [70] R. Aguado, “Majorana quasiparticles in condensed matter,” *Rivista del Nuovo Cimento*, vol. 40, Oct. 2017. doi: [10.1393/ncr/i2017-10141-9](https://doi.org/10.1393/ncr/i2017-10141-9).
- [71] R. P. Feynman, T. Hey, and R. W. Allen, *Feynman lectures on computation*. CRC Press, 2018.
- [72] C. W. J. Beenakker, P. Baireuther, Y. Herasymenko, I. Adagideli, L. Wang, and A. R. Akhmerov, “Deterministic creation and braiding of chiral edge vortices,” *Phys. Rev. Lett.*, vol. 122, p. 146 803, 14 Apr. 2019. doi: [10.1103/PhysRevLett.122.146803](https://doi.org/10.1103/PhysRevLett.122.146803). [Online]. Available: <https://link.aps.org/doi/10.1103/PhysRevLett.122.146803>.
- [73] H. Zhang, C.-X. Liu, S. Gazibegovic, *et al.*, “Retraction note: Quantized majorana conductance,” *Nature*, vol. 591, Mar. 2021. doi: [10.1038/s41586-021-03373-x](https://doi.org/10.1038/s41586-021-03373-x).
- [74] B. Van Wees, H. Van Houten, C. Beenakker, *et al.*, “Quantized conductance of point contacts in a two-dimensional electron gas,” *Physical Review Letters*, vol. 60, no. 9, p. 848, 1988.
- [75] S. Ahn, H. Pan, B. Woods, T. D. Stanescu, and S. D. Sarma, “Estimating disorder and its adverse effects in semiconductor majorana nanowires,” *Physical Review Materials*, vol. 5, no. 12, p. 124 602, 2021.
- [76] S. Vijay and L. Fu, “Quantum error correction for complex and majorana fermion qubits,” *arXiv preprint arXiv:1703.00459*, 2017.
- [77] J. Roffe, “Quantum error correction: An introductory guide,” *Contemporary Physics*, vol. 60, no. 3, pp. 226–245, 2019.
- [78] O. Kazakova, R. Puttock, C. Barton, *et al.*, “Frontiers of magnetic force microscopy,” *Journal of applied Physics*, vol. 125, no. 6, p. 060 901, 2019.
- [79] S. Vock, C. Hengst, M. Wolf, *et al.*, “Magnetic vortex observation in feco nanowires by quantitative magnetic force microscopy,” *Applied Physics Letters*, vol. 105, no. 17, p. 172 409, 2014.
- [80] C. Zeng, G. Sharma, T. D. Stanescu, and S. Tewari, “Feasibility of measurement-based braiding in the quasi-majorana regime of semiconductor-superconductor heterostructures,” *Physical Review B*, vol. 102, no. 20, p. 205 101, 2020.
- [81] G. Binnig and H. Rohrer, “Scanning tunneling microscopy,” *Surface science*, vol. 126, no. 1-3, pp. 236–244, 1983.

- [82] H. J. Zandvliet and A. van Houselt, “Scanning tunneling spectroscopy,” *Annual review of analytical chemistry*, vol. 2, pp. 37–55, 2009.
- [83] H. Pan, J. D. Sau, and S. D. Sarma, “Three-terminal nonlocal conductance in majorana nanowires: Distinguishing topological and trivial in realistic systems with disorder and inhomogeneous potential,” *Physical Review B*, vol. 103, no. 1, p. 014 513, 2021.
- [84] A. A. Abrikosov, “Nobel lecture: Type-ii superconductors and the vortex lattice,” *Reviews of modern physics*, vol. 76, no. 3, p. 975, 2004.
- [85] C.-K. Chiu, T. Machida, Y. Huang, T. Hanaguri, and F.-C. Zhang, “Scalable majorana vortex modes in iron-based superconductors,” *Science Advances*, vol. 6, Feb. 2020. doi: [10.1126/sciadv.aay0443](https://doi.org/10.1126/sciadv.aay0443).
- [86] C. Christian, E. F. Dumitrescu, and G. B. Halász, “Robustness of vortex-bound majorana zero modes against correlated disorder,” *Phys. Rev. B*, vol. 104, p. L020505, 2 Jul. 2021. doi: [10.1103/PhysRevB.104.L020505](https://doi.org/10.1103/PhysRevB.104.L020505). [Online]. Available: <https://link.aps.org/doi/10.1103/PhysRevB.104.L020505>.
- [87] J.-P. Xu, M.-X. Wang, Z. L. Liu, *et al.*, “Experimental detection of a majorana mode in the core of a magnetic vortex inside a topological insulator-superconductor $\text{Bi}_2\text{Te}_3/\text{NbSe}_2$ heterostructure,” *Phys. Rev. Lett.*, vol. 114, p. 017 001, 1 Jan. 2015. doi: [10.1103/PhysRevLett.114.017001](https://doi.org/10.1103/PhysRevLett.114.017001). [Online]. Available: <https://link.aps.org/doi/10.1103/PhysRevLett.114.017001>.
- [88] M. Chen, X. Chen, H. Yang, *et al.*, “Discrete energy levels of caroli-de gennes-matricon states in quantum limit in $\text{FeTe}_{0.55}\text{Se}_{0.45}$,” *Nature Communications*, vol. 9, no. 1, p. 970, 2018, ISSN: 2041-1723. [Online]. Available: <https://doi.org/10.1038/s41467-018-03404-8>.
- [89] L. Kong, L. Cao, S. Zhu, *et al.*, “Majorana zero modes in impurity-assisted vortex of $\text{FeTe}_{0.55}\text{Se}_{0.45}$ superconductor,” *Nature Communications*, vol. 12, no. 1, pp. 1–11, 2021. doi: [10.1038/s41467-021-24372-6](https://doi.org/10.1038/s41467-021-24372-6). [Online]. Available: <https://www.nature.com/articles/s41467-021-24372-6>.
- [90] L.-Y. Kong and H. Ding, “Emergent vortex majorana zero mode in iron-based superconductors,” *Acta Physica Sinica*, vol. 69, no. 11, p. 110 301, 2020, ISSN: 1000-3290. doi: [10.7498/aps.69.20200717](https://doi.org/10.7498/aps.69.20200717). [Online]. Available: <http://dx.doi.org/10.7498/aps.69.20200717>.
- [91] K. Jiang, X. Dai, and Z. Wang, “Quantum anomalous vortex and majorana zero mode in iron-based superconductor $\text{Fe}(\text{Te},\text{Se})$,” *Phys. Rev. X*, vol. 9, p. 011 033, 1 Feb. 2019. doi: [10.1103/PhysRevX.9.011033](https://doi.org/10.1103/PhysRevX.9.011033). [Online]. Available: <https://link.aps.org/doi/10.1103/PhysRevX.9.011033>.
- [92] T. Machida, Y. Sun, S. Pyon, *et al.*, “Zero-energy vortex bound state in the superconducting topological surface state of $\text{Fe}(\text{Se},\text{Te})$,” *Nature Materials*, vol. 18, no. 8, pp. 811–815, Jun. 2019, ISSN: 1476-4660. doi: [10.1038/s41563-019-0397-1](https://doi.org/10.1038/s41563-019-0397-1). [Online]. Available: <http://dx.doi.org/10.1038/s41563-019-0397-1>.
- [93] H. Kim, Y. Nagai, L. Rózsa, D. Schreyer, and R. Wiesendanger, “Anisotropic non-split zero-energy vortex bound states in a conventional superconductor,” *Applied Physics Reviews*, vol. 8, no. 3, 031417, p. 031 417, Sep. 2021. doi: [10.1063/5.0055839](https://doi.org/10.1063/5.0055839). arXiv: [2105.01354](https://arxiv.org/abs/2105.01354) [cond-mat.supr-con].

- [94] D. Wang, J. Wiebe, R. Zhong, G. Gu, and R. Wiesendanger, “Spin-polarized yu-shiba-rusinov states in an iron-based superconductor,” *Phys. Rev. Lett.*, vol. 126, p. 076 802, 7 Feb. 2021. doi: [10.1103/PhysRevLett.126.076802](https://doi.org/10.1103/PhysRevLett.126.076802). [Online]. Available: <https://link.aps.org/doi/10.1103/PhysRevLett.126.076802>.
- [95] X. Chen, W. Duan, X. Fan, *et al.*, “Friedel oscillations of vortex bound states under extreme quantum limit in $\text{KCa}_2\text{Fe}_4\text{As}_4\text{F}_2$,” *Phys. Rev. Lett.*, vol. 126, p. 257 002, 25 Jun. 2021. doi: [10.1103/PhysRevLett.126.257002](https://doi.org/10.1103/PhysRevLett.126.257002). [Online]. Available: <https://link.aps.org/doi/10.1103/PhysRevLett.126.257002>.
- [96] C. W. Groth, M. Wimmer, A. R. Akhmerov, and X. Waintal, “Kwant: A software package for quantum transport,” *New Journal of Physics*, vol. 16, no. 6, p. 063 065, Jun. 2014. doi: [10.1088/1367-2630/16/6/063065](https://doi.org/10.1088/1367-2630/16/6/063065). [Online]. Available: <https://doi.org/10.1088/1367-2630/16/6/063065>.
- [97] A. Rycerz, J. Tworzydło, and C. Beenakker, “Anomalously large conductance fluctuations in weakly disordered graphene,” *EPL (Europhysics Letters)*, vol. 79, no. 5, p. 57 003, 2007. [Online]. Available: <https://iopscience.iop.org/article/10.1209/0295-5075/79/57003/meta>.
- [98] J. Wurm, M. Wimmer, and K. Richter, “Symmetries and the conductance of graphene nanoribbons with long-range disorder,” *Physical Review B*, vol. 85, no. 24, p. 245 418, 2012. [Online]. Available: <https://journals.aps.org/prb/abstract/10.1103/PhysRevB.85.245418>.
- [99] A. Kreisel, P. J. Hirschfeld, and B. M. Andersen, “On the remarkable superconductivity of fese and its close cousins,” *Symmetry*, vol. 12, no. 9, p. 1402, 2020.
- [100] R. M. Lutchyn, J. D. Sau, and S. D. Sarma, “Majorana fermions and a topological phase transition in semiconductor-superconductor heterostructures,” *Physical review letters*, vol. 105, no. 7, p. 077 001, 2010.
- [101] S. Ryu, A. P. Schnyder, A. Furusaki, and A. W. Ludwig, “Topological insulators and superconductors: Tenfold way and dimensional hierarchy,” *New Journal of Physics*, vol. 12, no. 6, p. 065 010, 2010.
- [102] M. Cheng, R. M. Lutchyn, V. Galitski, and S. D. Sarma, “Splitting of majorana-fermion modes due to intervortex tunneling in a $p_x + ip_y$ superconductor,” *Phys. Rev. letters*, vol. 103, no. 10, p. 107 001, 2009.
- [103] J. Thijssen and J. Inglesfield, “Generating tight-binding hamiltonians with finite-difference methods,” *Physical Review B*, vol. 51, no. 24, p. 17 988, 1995.
- [104] D. Sticlet, C. Bena, and P. Simon, “Spin and majorana polarization in topological superconducting wires,” *Physical Review Letters*, vol. 108, no. 9, p. 096 802, 2012.
- [105] N. Sedlmayr and C. Bena, “Visualizing majorana bound states in one and two dimensions using the generalized majorana polarization,” *Phys. Rev. B*, vol. 92, p. 115 115, 11 Sep. 2015. doi: [10.1103/PhysRevB.92.115115](https://doi.org/10.1103/PhysRevB.92.115115). [Online]. Available: <https://link.aps.org/doi/10.1103/PhysRevB.92.115115>.
- [106] C. Bena, “Testing the formation of majorana states using majorana polarization,” *Comptes Rendus Physique*, vol. 18, no. 5-6, pp. 349–357, 2017.
- [107] C. W. Groth, M. Wimmer, A. R. Akhmerov, and X. Waintal, “Kwant: A software package for quantum transport,” *New Journal of Physics*, vol. 16, no. 6, p. 063 065, 2014.

- [108] F. Wilczek, *Fractional statistics and anyon superconductivity*. World scientific, 1990, vol. 5.
- [109] J. K. Pachos, *Introduction to topological quantum computation*. Cambridge University Press, 2012.
- [110] P. W. Shor, “Polynomial-time algorithms for prime factorization and discrete logarithms on a quantum computer,” *SIAM review*, vol. 41, no. 2, pp. 303–332, 1999.
- [111] M. A. Nielsen and I. Chuang, *Quantum computation and quantum information*. American Association of Physics Teachers, 2002.
- [112] D. P. DiVincenzo, “The physical implementation of quantum computation,” *Fortschritte der Physik: Progress of Physics*, vol. 48, no. 9-11, pp. 771–783, 2000.
- [113] M. Leijnse and K. Flensberg, “Parity qubits and poor man’s majorana bound states in double quantum dots,” *Phys. Rev. B*, vol. 86, p. 134 528, 13 Oct. 2012. doi: [10.1103/PhysRevB.86.134528](https://doi.org/10.1103/PhysRevB.86.134528). [Online]. Available: <https://link.aps.org/doi/10.1103/PhysRevB.86.134528>.
- [114] A. Tsintzis, R. S. Souto, and M. Leijnse, “Creating and detecting poor man’s majorana bound states in interacting quantum dots,” *arXiv preprint arXiv:2207.06160*, 2022.
- [115] T. Dvir, G. Wang, N. van Loo, *et al.*, “Realization of a minimal kitaev chain in coupled quantum dots,” *arXiv preprint arXiv:2206.08045*, 2022.
- [116] A. Vuik, B. Nijholt, A. Akhmerov, and M. Wimmer, “Reproducing topological properties with quasi-majorana states,” *SciPost Physics*, vol. 7, no. 5, p. 061, 2019.
- [117] U. E. Khodaeva and M. A. Skvortsov, “Vortex core near planar defects in a clean layered superconductor,” *Phys. Rev. B*, vol. 105, p. 134 504, 13 Apr. 2022. doi: [10.1103/PhysRevB.105.134504](https://doi.org/10.1103/PhysRevB.105.134504). [Online]. Available: <https://link.aps.org/doi/10.1103/PhysRevB.105.134504>.
- [118] N. J. Giordano, M. L. De Jong, S. R. McKay, and W. Christian, “Computational physics,” *Computers in Physics*, vol. 11, no. 4, pp. 351–351, 1997.